

AN ABSTRACT OF THE DISSERTATION OF

Michael Tassotto for the degree of Doctor of Philosophy in Physics presented on November/30/2000. Title: Time-of-Flight Direct Recoil Spectrometry: Application to Liquid Surfaces and Steps toward Quantification.

Abstract approved: _____ *Redacted for Privacy* _____
Philip R. Watson

Liquid surfaces are very abundant in nature. Despite the importance of the liquid interface in general, experimental molecular-level data was almost completely lacking prior to the last decade and a half. The intent of this work is to provide a means by which experimental data on the composition of liquid surfaces and the average orientation of their constituent molecules can be obtained in order to supplement data from molecular dynamics and related computational techniques. To this end, a unique time-of-flight (TOF) spectrometer, which constitutes the backbone of a new method to study liquid surfaces, was constructed and commissioned. The performance of the spectrometer is demonstrated in a number of exemplary TOF spectra obtained from liquid glycerol.

Moving from mere qualitative to quantitative surface analysis necessitates the ability to relate physical quantities such as detection efficiencies, accurate signal intensities, and interaction cross-sections for all elements to one another. As a first step, the absolute detection efficiency of a channel electron multiplier, used as particle detector in the spectrometer, was measured for the noble gas ions He^+ , Ar^+ , and Xe^+ . The data obtained led to an empirically derived, general expression of the detection efficiency that is applicable to particles of *any* atomic number. The results also show that the threshold velocity, below which a multiplier does not respond to impinging

ions, cannot be regarded as independent of the ion's atomic number as previously reported in the literature.

The second step involved a comprehensive investigation of ion-atom interactions and spectral features that are crucial for the processing of experimental signal intensities for quantitative analysis. For this purpose, the binary collision code MARLOWE was used in extensive trajectory calculations simulating TOF spectra. The simulation results confirm the high surface sensitivity of the technique and reveal the strong dependence of the sampling depth on the primary ion type and energy.

Finally, theoretically calculated interaction cross-sections for hydrogen, which had often been reported as being *abnormally* high, were investigated and a correction factor to the screening function of the atomic interaction potential was empirically derived. This constituted a crucial step toward a more accurate determination of surface concentrations involving hydrogen.

© Copyright by Michael Tassotto

November/30/2000

All Rights Reserved

**TIME-OF-FLIGHT DIRECT RECOIL SPECTROMETRY:
APPLICATION TO LIQUID SURFACES AND STEPS TOWARD
QUANTIFICATION**

by

Michael Tassotto

A Dissertation Submitted
to
Oregon State University

In Partial Fulfillment
of the Requirements for the
Degree of
Doctor of Philosophy

Presented November 30, 2000
Commencement June, 2001

Doctor of Philosophy dissertation of Michael Tassotto presented on November/30/2000.

APPROVED:

Redacted for Privacy

Major Professor, representing Physics

Redacted for Privacy

Chair of Department of Physics

Redacted for Privacy

Dean of Graduate School

I understand that my dissertation will become part of the permanent collection of Oregon State University libraries. My signature below authorizes the release of my dissertation to any reader upon request.

Redacted for Privacy

Michael Tassotto, Author

Acknowledgements

I would like to start my acknowledgements with a brief anecdote. Having come from the “Otto von Guericke” University of Magdeburg, which owes its name to the renowned son of Magdeburg, who got famous far beyond Germany for his pioneering research on the vacuum, I was totally surprised after setting foot into Dr. Phil Watson’s lab for the first time to find replicas of the Magdeburg hemispheres. In 1663, the originals were used in Berlin to demonstrate to the German Elector Friedrich Wilhelm that twelve horses on either side of the evacuated hemispheres were unable to pull them apart. While I would have cared less under other circumstances, with everything else around me being foreign, I suddenly felt at home. The “extra bonus” was that I liked the research Phil was doing.

Not quite two years after I had started working in his laboratory, Phil needed a second student to get his hands dirty in the construction of some kind of spectrometer. I am grateful for the confidence he placed in my abilities to see this project through to a successful completion. I am thankful for his guidance throughout this endeavor, which also depended on his knowledge and resourcefulness. I owe him a special thank-you for encouraging me to think independently. He also helped me out with financial support given by the National Science Foundation, the Research Corporation, and the OSU Research Council, which is hereby gratefully acknowledged.

My close co-worker, Tom Gannon (since October 1999 Dr. Gannon), deserves special recognition. He was instrumental in the joint construction efforts of the spectrometer. Without him as well as the technical support staff represented by Jim Swirczynski, John Archibald, and Ted Hinke, the spectrometer would never have seen “first light”. Thank you for lending your very capable hands!

Special thanks go to Al Gore for “creating the Internet”. It was the Internet through which I received numerous, tremendously helpful electronic communications from Dr. Mark T. Robinson, formerly of Oak Ridge National Laboratory. He was instrumental in getting me onto solid ground in regard to the computer simulations that are part of this work. I am greatly indebted to him.

The computer simulations would not have been possible without the great resources of the OSU Physics Department. In the same way, I am very thankful to Dr. Freeman and Dr. Hedberg for providing access to their workstations as well. The weeks of time I saved by having these resources are too numerous to count.

Joey Carson and her crew in the office of OSU's chemistry department, where I spent the majority of my time, surely provided one of the best working atmospheres a student would ever want to find himself in. No need was too big, no cry for help returned unanswered. They have what it takes to keep a smile on a student's face or, at least, return one to the same. Thank you so very much.

My parents deserve a very heartfelt thank-you for their continuing support in letting me come to OSU, originally as an exchange student. Little did anyone know that one year was to turn into two, three, ..., and eventually into a 'Goodbye' for good.

I also want to express my deepest gratitude to my wife, Mary Lynn, who has shared with me times of frustration and success as we have been facing this adventure together. Besides juggling her own career as a graduate student, she always found enough energy to support me in various ways such as lending me an ear to spout, loving me unconditionally, being my best fan, and keeping her husband's tummy happy. Her understanding, love, and patience were the primary pillars of this success story.

Finally, I honor the Lord, Jesus Christ; the One who places in our hearts the desire to ask questions and allows us to discover, in some small measure, the working of the world He created.

Contribution of Authors

The construction of the time-of-flight spectrometer described in Chapter 2 was a concerted effort of Thomas J. Gannon and the author. Due credit is given directly or by means of literature references for components exclusively contributed by T. J. Gannon but mentioned in this work for completeness sake.

Table of Contents

	<u>Page</u>
Chapter 1. General Introduction	1
1.1. Surfaces and their Importance	1
1.2. A Zoo of Surface Analytical Techniques.....	2
1.3. Ion Scattering and Recoiling from Surfaces	4
1.4. Objective of this Project.....	6
1.5. Time-of-Flight Direct Recoil Spectrometry (TOF–DRS)	7
1.5.1. Basic Principle of TOF–DRS	7
1.5.2. Kinematics of Ion–Surface Collisions	8
1.5.2.1. Single Scattering (SS)	10
1.5.2.2. Multiple Scattering (MS)	11
1.5.2.3. Direct Recoiling (DR).....	11
1.5.2.4. Surface Recoiling and Deflect Recoiling.....	12
1.5.2.5. Cascade Sputtering.....	13
1.5.3. Projectile–Target Interaction Cross-Sections	13
1.6. The Binary Collision Computer Code MARLOWE	17
1.6.1. MARLOWE: Computer Simulation of Atomic Collisions in Crystalline Solids.....	17
1.6.2. The Binary Collision Approximation (BCA)	19
1.6.3. Interatomic Potential Energy Functions in MARLOWE	20
1.6.4. Modeling of Inelastic Energy Losses in MARLOWE	22
1.7. Dissertation Outline	24
Chapter 2. Ion Scattering and Recoiling from Liquid Surfaces	26
2.1. Introduction.....	27
2.2. Spectrometer Design.....	31
2.2.1. Overview.....	31
2.2.2. Ion Source	31
2.2.3. Mass and Velocity Selection.....	34
2.2.4. Ion Optics.....	37
2.2.5. Beam Pulsing Scheme.....	38

Table of Contents (Continued)

	<u>Page</u>
2.2.6. Differential Pumping	39
2.2.7. Sample Introduction.....	43
2.2.8. Particle Detection.....	44
2.2.9. Data Acquisition Electronics	44
2.2.10. Miscellaneous	46
2.2.10.1. Beam Position Monitors	46
2.2.10.2. Diffusion Pump Protection Circuitry	47
2.3. Performance	52
 Chapter 3. Detection Efficiency of a Channel Electron Multiplier for Low Energy Incident Noble Gas Ions.....	 57
 3.1. Abstract.....	 58
3.2. Introduction.....	58
3.3. Experimental Method.....	61
3.4. Results.....	64
3.5. Discussion	69
 Chapter 4. Simulation of Time-of-Flight Spectra in Direct Recoil Spectrometry for the Study of Recoil Depth Distributions and Multiple Scattering Contributions	 72
 4.1. Abstract.....	 73
4.2. Introduction.....	73
4.3. Simulation Model	75
4.4. Results and Discussion	79
4.4.1. 2 keV Ar ⁺ Bombardment of the Diamond {001} Surface	79
4.4.2. Influence of Projectile Type and Energy on Recoil Intensity and Peak Shape	85
4.4.3. 2 keV Ar ⁺ Bombardment of the Alkane Polymer {001} Surface	87
4.4.4. Comparison to Experimental Data.....	93

Table of Contents (Continued)

	<u>Page</u>
4.4.4.1. Liquid Heptadecane	93
4.4.4.2. Monocrystalline Hexatriacontane	95
4.5. Summary	98
Chapter 5. A Correction Factor to the Screening Radius for Atomic Interactions Involving Hydrogen and its Application in Direct Recoil Spectrometry.....	99
5.1. Abstract.....	100
5.2. Introduction.....	100
5.3. Theoretical Considerations and Potentials.....	102
5.4. Experimental Method.....	107
5.5. Simulation Model	108
5.6. Results and Discussion	109
5.6.1. The Surface of Liquid Heptadecane	109
5.6.2. Empirical Estimation of the Screening Radius a_{X-H}	112
5.6.3. Test of a_{X-H} in TOF Simulations	115
5.6.3.1. 2.5 keV Ar ⁺ Bombardment of Heptadecane	116
5.6.3.2. 2.2 keV Ne ⁺ Bombardment of Heptadecane.....	119
5.6.3.3. 4.0 keV Ar ⁺ Bombardment of an Organic Polymer.....	121
5.6.4. The Correction factor Γ_{X-H}	123
5.7. Summary	124
Chapter 6. General Conclusions	125
Bibliography	129
Appendices.....	136

List of Figures

<u>Figure</u>	<u>Page</u>
1.1 Schematic diagram of scattering and recoiling processes.....	8
1.2 Definition of angles and other experimental parameters.	9
1.3 Schematic drawing of surface recoiling and deflect recoiling processes.	12
1.4 Calculated differential scattering [$\sigma^s(\theta)$] and recoil [$\sigma^r(\phi)$] cross-sections as a function of the scattering angle θ and recoil angle ϕ	16
1.5 Calculated differential recoil cross-section $\sigma^r(\phi)$ as a function of the projectile energy E_0	17
2.1 Schematic drawing of the major components of the time-of-flight ion scattering and recoiling spectrometer.	32
2.2 Schematic drawing of the Wien filter assembly.	35
2.3 Plot of the vertical deflection (due to changes in mass) of charged residual gas molecules as a function of their location behind the Wien-filter deflector plates.	36
2.4 Photograph of the ion optics assembly.	37
2.5 Schematic diagram of the pulsing regime and voltage-pulse sequences.	38
2.6 Schematic drawing of the spectrometer's vacuum system.	41
2.7 Photograph and schematic drawing of the liquid sample cell.....	43
2.8 Photograph of a beam-position monitor (BPM).	47
2.9 Schematic diagram showing the circuitry controlling the flow of power to the diffusion pumps.	49
2.10 Schematic circuit diagram of the pressure sensing control unit.	49
2.11 Influence of the projectile ion type on the peak positions in a TOF spectrum.	53
2.12 Time-of-flight spectra from glycerol using 2.5 keV Ne^+ ions at $\phi = 45^\circ$	55

List of Figures (Continued)

<u>Figure</u>		<u>Page</u>
3.1	Schematic diagram of the experimental setup.	61
3.2	Faraday cup current (I_{FC}) as function of retarding voltage (V_{RET}) for He^+ ions. The maximum of the derivative is found at $V_{RET} = 1690$ V.....	63
3.3	Absolute detection efficiency for Xe^+ , Ar^+ and He^+ as function of ion velocity.....	65
3.4	Threshold velocity, v^{th} , as function of inverse atomic number.	66
3.5	Linear regression for the determination of constants a and n in Eq. (3.4).....	68
4.1	Model surfaces chosen for DRS simulations.	76
4.2	Calculated TOF–DRS spectra for 2 keV Ar^+ bombardment of the diamond {001} surface with overlaid area plots of depth distribution.	80
4.3	Definition of the local incident angle α_L and local recoil angle ϕ_L	82
4.4	Calculated average values of collision parameters between Ar projectiles and first-layer C atoms.....	83
4.5	Comparison of calculated TOF–DRS spectra for bombardment of the diamond {001} surface by projectiles of varying type and energy with overlaid area plots of depth distribution.	86
4.6	Calculated TOF–DRS spectra for 2 keV Ar^+ bombardment of the alkane polymer {001} surface with overlaid area plots of depth distribution.	88
4.7	Calculated average values of collision parameters between Ar projectiles and methyl-group C atoms.....	90
4.8	Example of an area plot revealing the identity of the collision partner that caused the initial displacement of hydrogen and carbon recoils.....	92
4.9	Comparison of an experimental TOF–DRS spectrum for liquid heptadecane with simulation.....	94
4.10	Comparison of an experimental TOF–DRS spectrum for hexatriacontane with simulation.	96

List of Figures (Continued)

<u>Figure</u>	<u>Page</u>
4.11 Incident angle α -scan of directly recoiled carbon atoms from hexatriacontane.	97
5.1 Differential recoil cross-section as function of target mass calculated for collisions with a primary Ar^+ projectile.	104
5.2 TOF spectrum showing hydrogen and carbon recoil peaks resulting from Ar^+ bombardment of liquid heptadecane.	110
5.3 Measured peak intensity ratios, $S_{\text{H}}/S_{\text{C}}$, versus beam incident angle α	111
5.4 Comparison of calculated TOF spectra (dashed line) with an experimental one (solid line) for 2.5 keV Ar^+ bombardment of liquid heptadecane at 23°C and $\alpha = 16^\circ$	113
5.5 Comparison of calculated TOF spectra (solid lines) to experiment (solid circles) for 2.5 keV Ar^+ ion bombardment of liquid heptadecane at 41°C for incident angles $\alpha = 12, 20,$ and 28°	117
5.6 Comparison of calculated TOF spectra (solid lines) to experiment (solid circles) for 2.2 keV Ne^+ ion bombardment of liquid heptadecane at 41°C for incident angles $\alpha = 12, 20,$ and 28°	120
5.7 Comparison of calculated TOF spectra (dashed lines) to an experimental one (solid line) for hexatriacontane [98] resulting from 4.0 keV Ar^+ irradiation at $\alpha = 6^\circ$	122
5.8 Plot of the correction factor $\Gamma_{\text{X-H}}$ versus the atomic number Z_1	124

List of Tables

<u>Table</u>		<u>Page</u>
3.1	List of energy and corresponding velocity ranges exhibiting linear increase of the detection efficiency for the noble gas ions He ⁺ , Ar ⁺ , and Xe ⁺ as seen in Fig. 3.3.....	65
3.2	Threshold velocities v^{th} from this work compared with literature values.	67
3.3	Values of the constants a , b , c , and n for $\varepsilon(v, Z) = a (v - b/Z^c) Z^n$	68

List of Appendices

<u>Appendix</u>	<u>Page</u>
A. FORTRAN Code for User-Supplied MARLOWE Analysis Procedure EXTRAZ.....	137
B. FORTRAN Code for User-Supplied MARLOWE Analysis Procedure SINGLEZ.....	143
C. FORTRAN Code for User-Supplied MARLOWE CODE and COMMON Blocks	146
D. Additions to MARLOWE Source Code	147

Dedication

Diese Arbeit ist meinen lieben Eltern, Marianne und Eduard, gewidmet.



This dissertation is dedicated to my dear parents, Marianne and Eduard.

TIME-OF-FLIGHT DIRECT RECOIL SPECTROMETRY: APPLICATION TO LIQUID SURFACES AND STEPS TOWARD QUANTIFICATION

Chapter 1. General Introduction

1.1. Surfaces and their Importance

The surface behavior of materials in different environments is crucial to our lives. Special surface treatments can help overcome obvious problems such as corrosion. The surface chemistry of polymers can be tuned to provide selective reduction or enhancement of protein adsorption, which is important in replacing components of the human body. The auto-exhaust catalyst, which removes some of the worst output of the combustion engine, is a masterpiece of surface chemistry. A change in surface composition or the application of surface coatings can help shape the optical and/or electronic behavior of materials. Thus, whether one considers a car body shell, a biomedical implant, a catalyst, or a solid state electronic device, it is the surface that interfaces with its environment. The extent to which a surface is either reactive or inert will determine how well the material behaves in its intended function. It is therefore vital that the surface properties and the behavior of materials used in our modern world are thoroughly understood [1].

The ability to characterize surfaces directly affects the progress made in surface science, which is a field of great importance to many disciplines ranging from physics and chemistry to life sciences and modern electronic technology. The term *surface science* and its inception as a separate field of study have their origin in the early 1960s. Since then, experimental investigations of interfacial phenomena and surface properties have largely focused on solid state materials.

Liquid surfaces are ubiquitous in nature. Diverse properties of a liquid such as adhesion, lubrication, and wetting are connected to its microscopic surface chemical structure. A gas-phase specie's interaction with and subsequent dissolution in a liquid depend on what it encounters at the surface. Evaporation and condensation processes

involve mass and energy transport across the liquid–air interface. Among the various surface properties, molecular orientation is of special interest because of its relevance to a variety of interfacial phenomena such as ion exchange, catalysis, and bio-membrane functions. Despite the importance of the liquid interface in general, experimental molecular-level data was almost completely lacking prior to the last decade and a half. By far most of the available information on liquid surface structure comes from theoretical modeling. Only a few examples shall be mentioned in this context in the following paragraph.

Due to its importance, the liquid–vapor interface of water has seen much attention in molecular dynamics (MD) simulations. For example, among the properties studied are the surface potential of water [2] and its variation with depth, the surface tension and surface excess energy [3] as thermodynamic quantities, and density profiles of the interfacial transition region [4]. Evaporation and condensation processes [5] as well as static properties of methanol, such as its preferred orientation in the surface [6], have been investigated by MD. The methanol molecules project their hydrophobic methyl groups toward the vapor phase in an effort to maximize the number of hydrogen bonds. Other organic molecules in their liquid state such as formamide (HCONH_2) [7], benzyl alcohol [8], and glycerol [9] have more or less recently been studied using MD techniques. Finally, the unusual surface-ordering phenomenon of liquid *n*-alkanes, e.g. the formation of a monolayer of molecules aligned perpendicular to the surface, has been investigated in simulation studies [10,11]. One such *n*-alkane, liquid heptadecane ($\text{C}_{17}\text{H}_{36}$), was used as a model system for known surface structure and composition in the study described in Chapter 5.

1.2. A Zoo of Surface Analytical Techniques

As may be imagined, there is a wide spectrum of experimental tools available to study surfaces, but only a few can provide quantitative information about molecular orientation at an interface. Each technique has its own shortcomings. Particle scattering techniques require high vacuum. Neutron scattering depends on large experimental facilities and, along with X-ray diffraction, is mostly limited to

crystalline samples. Some optical techniques such as infrared, Raman, or ultraviolet/visible spectroscopy and ellipsometry can be applied to any interfaces accessible by light, but they usually lack sufficient surface specificity to discriminate against bulk contributions [12]. Angle-resolved X-ray photoelectron spectroscopy (XPS) has been used, for instance, on perfluoropolyethers to investigate the depth and tilt of preferential surface ordering [13,14].

An analytical technique, which is said to have perfect surface sensitivity, for the characterization of liquid and solid surfaces is MIES (metastable induced electron spectroscopy) [15]. However, only a small minority of surface scientists makes use of this technique. This is due to the more complicated interpretation of MIES spectra in terms of surface properties compared to other electron spectroscopies. Additionally, metastable rare gas atoms and alkali atoms exhibit a close similarity in their reactive behavior, which further complicates interpretation.

With the dawn of laser technology, new optical tools became available such as second harmonic generation (SHG) and sum-frequency generation (SFG). These are three-wave mixing processes that originate from the rapid change of index of refraction that occurs at an interface [16]. SHG is experimentally simpler to implement because it involves only one frequency input. However, this simplicity comes at the cost of difficulties in interpretation. Tuning in to resonances to boost selected signals diminishes general applicability of the technique because problems of peak-overlap arise in mixtures. SFG provides a remedy by accessing two input frequencies, one in the infrared and one in the visible range of wavelengths, now at the cost of experimental complexity. Sufficiently intense tunable infrared frequencies are necessary to drive the nonlinear polarization.

Nathanson and co-workers [17] employ molecular beam scattering to gain an understanding of fundamental steps involved in the mixing of gases and liquids and reactions between them. Mechanisms of trapping of gas molecules and energy transfer play important roles in attempting to answer these fundamental questions, as do the presence of functional groups in the liquid surface and roughness. Together with spectroscopic approaches like SHG and SFG and with computer simulations of

interfaces, these methods are helping to provide a predictive, molecular picture of interfacial chemistry.

Near-edge X-ray absorption fine structure (NEXAFS) spectroscopy has been shown to be a useful probe of the structure, orientation and bonding characteristics of a variety of molecules to (catalytic) substrates [18]. While mostly solid samples have been considered in the analysis of molecular orientation with NEXAFS, studies on liquid surfaces have not been well developed due to the generally high vapor pressure of liquids and the lack of long-range order. Recently, the temperature dependence of the surface structure of a long-chain normal alkane was studied using NEXAFS in the solid and liquid phase [19]. The results showed a molecularly ordered phase in the liquid up to 1.3°C above the bulk melting point – an unusual behavior that was previously observed in other n-alkanes using various surface sensitive techniques (see [11] and Refs. therein).

1.3. Ion Scattering and Recoiling from Surfaces

In order to avoid confusion from the beginning, a brief introduction of frequently and rather freely used terms is given. Throughout this work, *incident ion*, *primary ion*, and *primary projectile* all refer to an ion impinging upon a target surface at some energy. The terms *ejected (target) atoms*, *recoiled (target) atoms*, and simply *recoils* refer to atoms or ions, originally part of the material under study, leaving the target surface as a direct result of having been struck by either a primary ion or another target atom that was displaced and set in motion.

Surface analytical methods designated as ion scattering spectroscopy (ISS) have been used for the past three decades to probe elemental composition, near-surface crystal structure, and electronic configurations of the target. In the various ISS techniques, a beam of mono-energetic (mostly rare gas) ions is directed at the surface, and the scattered primary projectiles are detected. The energy of the scattered ion is directly related to the mass of the target atom from which it scattered and, therefore, the energy spectrum represents a mass spectrum of the target atoms. Incident ion energies can range from a few hundred electronvolts (eV) to several MeV. Rutherford

backscattering (RBS) and elastic recoil detection (ERD) represent the high-energy end of ISS. Here, high-energy nuclei (e.g. He^+) are used to probe the long range atomic order and elemental makeup of bulk samples. On the contrary, secondary ion mass spectrometry (SIMS) represents the low-energy end of ISS, performing elemental analysis by detecting low-energy ions liberated from surfaces due to keV ion impact.

Terminology such as LEIS and MEIS, for low and medium-energy ion scattering, respectively, does not necessarily categorize ISS techniques according to the energy range of their primary ions. Although it is generally accepted that incident ions of a few keV are regarded as low-energy projectiles, there certainly are exceptions. Fluoride ions ejected from a polymer surface as the result of Ar^+ bombardment at 320 eV have recently been referred to as high-energy recoils [20]. In this work, the generally accepted view will be adhered to, e.g. energies of 1–10 keV are considered low.

Ion/surface reactive scattering at very low energies (< 100 eV) and surface-induced dissociation have been coupled with mass spectrometry to learn more about the surface structure of liquid polymers. Cooks and co-workers [21,22] investigated a liquid perfluorinated polyether (PFPE) surface, and their results suggest microscopic ordering of the molecules with the $-\text{CF}_3$ end-groups projecting outward from the surface. Other researchers used the PFPE surface to study the dynamics of inelastic scattering and fragmentation mechanisms of incident molecular ions [23]. In these studies, information about the system under investigation is exclusively obtained from an analysis of the properties of the primary incident projectile after its collision with the target.

While in ISS all interest is placed upon scattered primary ions, direct recoil spectrometry (DRS) energy-analyzes the flux of target atoms escaping the surface after atomic collisions with incident projectiles. Rabalais and co-workers have been developing time-of-flight (TOF) methods for scattering and recoiling from solid materials, spectral interpretation, and surface elemental analysis since the early 1980's [24]. They built the first TOF spectrometer system with a long flight path for separation of scattered and recoiled particles and continuous variation of the scattering

and recoiling angles [25]. This enabled them to concentrate their efforts on surface structural determinations. The coupling of TOF methods with the detection of both scattered and recoiled particles has led to the development of time-of-flight scattering and recoiling spectrometry (TOF–SARS) as a tool capable of making unique contributions in the area of structural surface analysis [26].

In 1997, work in this laboratory, particularly the efforts described in Chapter 2 in this dissertation, led to the first-time demonstration of the general applicability of the TOF–SARS technique to probe the composition and molecular orientation of the surface of liquids [27]. Independently and very shortly thereafter, Andersson and Morgner [28] successfully applied two forms of ion scattering spectroscopy, namely impact collision ISS and neutral impact collision ISS, to surfaces of organic liquids. They demonstrated the usefulness of these methods by determining the concentration–depth profiles of solutions with surface-active solutes and the qualitative composition of their outermost layer.

1.4. Objective of this Project

The TOF–SARS technique combines a number of attractive features that make it very applicable as an analytical tool not only to crystalline samples but potentially also to surfaces of liquids. These features include:

- extreme surface sensitivity, no integration over significant depth of material,
- detection of *all* elements including hydrogen (distinguishes H from D),
- direct probe of surface atomic composition,
- applicable to solutions, including inorganics and ions,
- useful tool for investigating orientation of surface species,
- use of relatively simple equipment.

The objective of this project was twofold. Initially, the concept of successfully using TOF–SARS measurements for liquid surfaces was to be proven and demonstrated. To this end, a time-of-flight scattering and recoiling spectrometer was constructed and commissioned. The spectrometer’s capabilities to generate

uncontaminated and representative surfaces of low vapor pressure liquids and to provide qualitative surface composition data was then tested.

The second part of this project focused on the direct recoil method of the TOF–SARS technique and its quantification for surface analysis. In direct recoil spectrometry (DRS), which will be introduced in more detail in Section 1.5 below, the primary interest is placed upon the detection of target atoms ejected from the surface. TOF spectra of these recoils exhibit characteristic peak shapes that are not well understood to date. The goal was a comprehensive investigation of ion-atom interactions and spectral features that are crucial for the detailed understanding and processing of experimental data for quantitative surface analysis by DRS. Specifically, the detection efficiency for recoils, spectral peak overlap, depth distributions of recoils and their multiple scattering contributions to TOF spectra, and ion-atom interaction cross-sections were investigated.

The in-depth analysis of TOF spectra in DRS was aided by computer simulations performed using the binary collision code MARLOWE [29]. An introduction to MARLOWE will be given in Section 1.6 below.

1.5. Time-of-Flight Direct Recoil Spectrometry (TOF–DRS)

1.5.1. Basic Principle of TOF–DRS

The schematic drawing in Fig. 1.1 depicts the basic principle of ion scattering and recoiling. A pulsed ion beam is incident upon the sample surface, here shown as crystalline. Upon impact, primary ions can be scattered by the sample or they eject atoms out of the surface. Scattered and recoiled particles traverse the distance from the sample to the detector, which, in this case, is a channel electron multiplier, where they are recorded as a function of flight time. The resulting TOF spectrum can exhibit direct recoil (DR), single, and multiple scattering peaks. Depending on the exact experimental parameters, single scattering or DR features can be enhanced or eliminated from the spectrum.

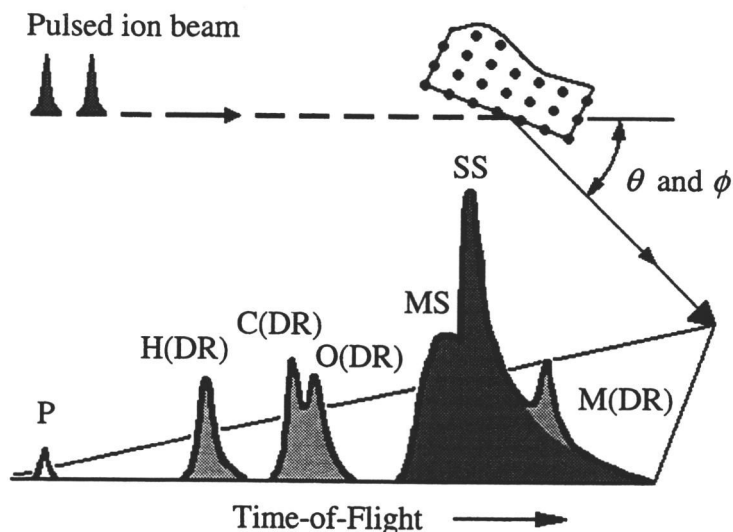


Fig. 1.1 Schematic diagram of scattering and recoiling processes. A pulsed primary ion beam impinges on a sample from the left, and scattered and recoiled particles are detected by an electron multiplier. The TOF spectrum shows hydrogen, carbon, oxygen, and metal direct recoils (DR) together with single (SS) and multiple (MS) scattering peaks. The peak labeled 'P' is due to photons resulting from inelastic collisions and defines time zero on the abscissa.

In DRS, experimental geometries are chosen in such a way as to suppress the intense single scattering peaks. This aspect will be discussed in more detail in Chapter 2. The technique of DRS was first suggested by Chen et al. [30] and has been used in the past for adsorbate surface structure determinations, investigations of chemisorption processes, and thin-film growth and nucleation studies. Rabalais [31] and Hammond et al. [32] have written reviews on many of these applications.

1.5.2. Kinematics of Ion-Surface Collisions

The kinematics of energetic atomic collisions is accurately described by classical mechanics [33,34]. Mutual Coulomb repulsion between the colliding atomic cores, that is the nucleus plus core electrons, leads to such scattering. The scattered primary atom transfers part of its energy to the target atom which, in turn, recoils into a forward direction. The final energies and trajectories of the scattered and recoiled

atoms are determined by the atomic masses involved and the closeness of their encounter. The latter is called the impact parameter p and is defined as the perpendicular distance at which an incident projectile would pass by a target atom in the absence of any interatomic interaction, $V(r) = 0$.

Fig. 1.2 displays experimental parameters such as the incident angle, α , which is defined with respect to the surface plane, the scattering and recoil angles θ and ϕ , respectively, as well as the masses and energies of the colliding particles. In DRS, the ion source and the particle detector lie in a plane that includes the surface normal of the sample. When the primary ion strikes the surface, where initially all atoms are considered to be at rest, a large variety of collisions can occur. The major spectral features in Fig. 1.1 can be classified [31], in an overly simplified but rather useful way, into five categories. Although this work is primarily concerned with recoiling mechanisms, scattering of the incident ion will also be considered for completeness sake. In the equations below, energies and angles refer to in-plane scattering and recoiling (see Fig. 1.2) – geometrical conditions that are exploited experimentally in DRS.

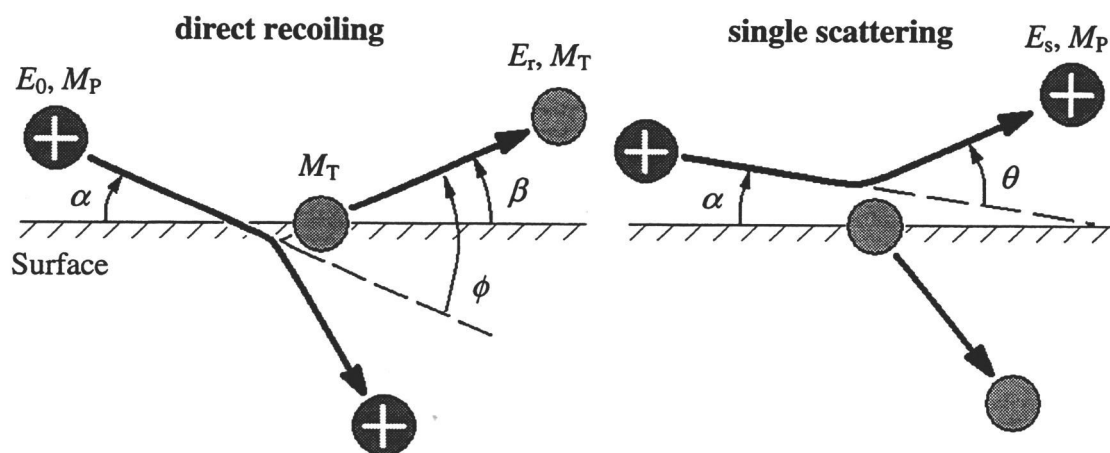


Fig. 1.2 Definition of angles and other experimental parameters. α - incident angle; β - exit angle; θ - scattering angle; ϕ - recoil angle; E_0, M_P - kinetic energy and mass of primary projectile; E_r, M_T - kinetic energy transferred to and mass of recoiled target atom; E_s, M_P - kinetic energy of scattered primary projectile after collision.

1.5.2.1. Single Scattering (SS)

The primary ion suffers one large-angle deflection, which might be preceded and followed by a few small-angle deflections. This normally produces a sharp scattering peak (labeled SS in Fig. 1.1) whose energy is near the theoretical single-collision energy, which is given by

$$E_s = E_0 \left(\cos \theta \pm \sqrt{A^2 - \sin^2 \theta} \right)^2 / (1 + A)^2, \quad (1.1)$$

where $A = M_T / M_P$. The positive sign in Eq. (1.1) is used for $M_P \leq M_T$. When the incident projectile is heavier than the target atom, $M_P > M_T$, the expression is double-valued and both signs apply. This means that for each scattering angle, θ , there are two E_s . Which energy the scattered projectile will end up with depends on the impact parameter. Additionally, for $M_P > M_T$, the projectiles do not experience backscattering, and a maximum or critical scattering angle, θ_c , exists that depends on the mass ratio,

$$\theta_c = \sin^{-1}(M_T / M_P). \quad (1.2)$$

The final energy of the scattered primary ion can be converted into a time-of-flight, t_{SS} , based on the drift length, L , from the sample to the detector and is given by

$$t_{SS} = \left\{ L(1 + A) / \left(\sqrt{2E_0 / M_P} \left(\cos \theta \pm \sqrt{A^2 - \sin^2 \theta} \right) \right) \right\} \times U, \quad (1.3)$$

with

$$U = \sqrt{e / amu} \times 10^{-4} = 0.9823. \quad (1.4)$$

Here, e is the elementary charge, 1.60219×10^{-19} C, and amu stands for atomic mass unit, 1.66057×10^{-27} kg. The factor U in Eq. (1.3) facilitates a convenient unit conversion so that t_{SS} is obtained in microseconds while L , E_0 , and M_P are entered in centimeters, electronvolts, and mass number, respectively.

1.5.2.2. Multiple Scattering (MS)

The phrase ‘multiple scattering’ encompasses a variety of different collision scenarios. The typical result is a rather broad spectral feature, denoted by MS in Fig. 1.1, which extends to either side of the single scattering peak. Here, at least two large-angle deflections that are preceded and followed by smaller ones are suffered by the ion. Repeated application of Eq. (1.1) with fractions of the scattering angle such as $\theta/2$ and $\theta/3$ for double and triple collisions, respectively, allows the approximation of the high-energy limit of the MS feature. MS sequences producing slower scattered particles often include backscattering ($> 90^\circ$, $M_P < M_T$). The breadth of the MS peak arises from the various multiple-angle combinations, which can result in deflection into the laboratory scattering angle θ .

One has to keep in mind that the MS feature in Fig. 1.1 results from macroscopic in-plane collision sequences. Here, macroscopic means that the initial and final velocity vectors (\mathbf{v}_i and \mathbf{v}_f , respectively) of the projectile before and after collisions with target atoms lie in planes that are parallel to each other ($\mathbf{v}_i \parallel \mathbf{v}_f$). Only then, a multiply scattered projectile will reach the detector. Obviously, the vast majority of MS sequences is characterized by $\mathbf{v}_i \nparallel \mathbf{v}_f$ and, thus, is removed from the TOF spectrum.

1.5.2.3. Direct Recoiling (DR)

While in Section 1.5.2.1 above the scattered ion leaves the collision site with energy E_s , the energy transferred to the collision partner is given by E_r ,

$$E_r = E_0 \left(4A / (1 + A)^2 \right) \cos^2 \phi. \quad (1.5)$$

The time-of-flight, t_{DR} , corresponding to E_r can be written down similar to Eq. (1.3) and is expressed as

$$t_{DR} = \left\{ L(1 + A) / \left(\cos \phi \sqrt{8E_0 / M_P} \right) \right\} \times U. \quad (1.6)$$

Using $A = M_T / M_P$ and solving Eq. (1.6) for M_T yields

$$M_T = \left\{ t_{DR} \cos \phi \sqrt{8E_0 / M_P} / (L \times U) \right\} - M_P. \quad (1.7)$$

Thus, in principle, every DR peak in a TOF spectrum can be assigned a mass number based on its measured position, t_{DR} , along the time axis which allows qualitative identification of atoms recoiled from the target surface. This basic idea is identical to the one exploited in time-of-flight secondary ion mass spectrometry (TOF-SIMS).

1.5.2.4. Surface Recoiling and Deflect Recoiling

The collision mechanisms shown in Fig. 1.3 involve a combination of both recoiling and scattering collisions. In surface recoiling, a primary projectile directly recoils a target atom into a forward direction, and this recoil can then be scattered from neighboring target atoms. This sequence is particularly sensitive to light adsorbates such as hydrogen. For H, it can be observed, under specific experimental conditions, as a low-intensity, broad feature on the high-energy side of the hydrogen DR peak. A target atom can also be recoiled by a primary ion previously scattered by another target atom. This process is called deflect recoiling [35].

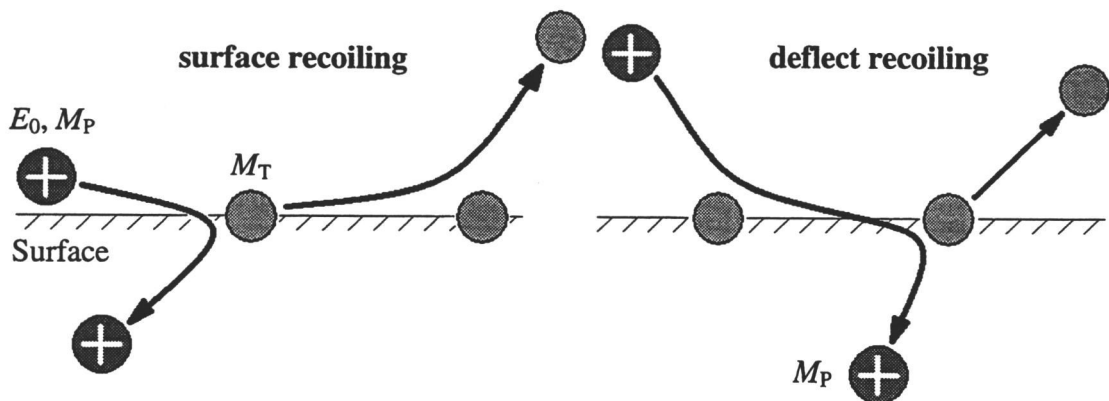


Fig. 1.3 Schematic drawing of surface recoiling and deflect recoiling processes. Combinations of both also occur.

Of course, the combination of both recoiling effects is possible, as is double recoiling. However, the latter case is not very likely because its total cross-section is very low [36].

1.5.2.5. Cascade Sputtering

Cascade sputtering results when the energy of the primary ion is dissipated to target atoms through collision cascades. Some of these cascades are eventually directed toward the surface, causing atom, molecule, and cluster ejection. The energy distributions of such sputtered atoms are very broad and peak at low energies (1 to 20 eV). The low velocities of such particles do not permit their detection in a channel electron multiplier because they fall under the detection threshold.

1.5.3. Projectile–Target Interaction Cross-Sections

Relationships such as Eqs. (1.1) and (1.5) merely *connect* the initial state of a moving projectile with the final states of the original projectile and the struck target atom. No attempt is made to *predict* a final energy or a scattering angle. In order to engage in the latter, one has to look more closely at the collision process and investigate the distribution of final energies and scattering angles, which would result from collisions at various impact parameters. Detailed derivations of these fundamental parameters, called differential scattering or energy-transfer cross-sections, can be found in various texts [33,34,37-39]. In this context, only a brief introduction to the differential scattering cross-section shall be given with the focus placed on concepts and formulas in their final form. Functional dependencies shown in exemplary graphs below will emphasize experimental parameters such as angles, energies, and projectile/target mass combinations that are typical for this work.

The probability of scattering a projectile into the solid angle $d\Omega$ at some center-of-mass (CM) scattering angle between θ_{CM} and $\theta_{\text{CM}} + d\theta_{\text{CM}}$ is called the differential scattering cross-section, $\sigma(\theta_{\text{CM}})$, and is defined as [34]

$$\sigma(\theta_{\text{CM}}) = \frac{d\sigma}{d\Omega} = \frac{\left(\begin{array}{c} \text{Number of interactions per target particle that} \\ \text{lead to scattering into } d\Omega \text{ at the angle } \theta_{\text{CM}} \end{array} \right)}{\text{Number of incident particles per unit area}} \quad (1.8)$$

The assumption of conservation of the number of particles scattered in a central force field leads to the well-known expression for the differential scattering cross-section,

$$\sigma(\theta_{\text{CM}}) = \frac{p}{\sin \theta_{\text{CM}}} \left| \frac{d\theta_{\text{CM}}}{dp} \right|^{-1} \quad (1.9)$$

The quantity $\theta_{\text{CM}}(p)$ is called the scattering integral and relates the scattering angle to the impact parameter (see also Section 1.6.2). $\theta_{\text{CM}}(p)$ depends on the potential that governs the interaction between the colliding particles. For example, atomic interactions of high-energy charged particles are well described by the Coulomb potential,

$$V(r) = Z_1 Z_2 e^2 / r, \quad (1.10)$$

where Z_1 and Z_2 are the atomic numbers of the colliding particles, r is their distance of separation, and e is the elementary charge. Determination of $\theta_{\text{CM}}(p)$ using the Coulomb potential and subsequent evaluation of Eq. (1.9) lead to an analytical solution for $\sigma(\theta_{\text{CM}})$ which is known as the Rutherford scattering formula [34],

$$\sigma(\theta_{\text{CM}}) = \frac{Z_1 Z_2 e^2}{(4E'_0)^2} \frac{1}{\sin^4(\theta_{\text{CM}}/2)}, \quad (1.11)$$

with E'_0 being the initial relative kinetic energy in the CM-system. In the case of the Coulomb and inverse-power potentials, $V(r) \propto 1/r^n$, one may write simple analytical expressions for $\sigma(\theta_{\text{CM}})$. However, frequent use is made of empirically derived potentials for which a solution to Eq. (1.9) has to be found numerically. The empirical potential that was extensively used in this work is the Molière potential. It is merely mentioned at this point because it was employed in calculating differential cross-

sections for the graphs shown below in this section. The Molière potential shall be introduced in more detail in Section 1.6.3.

The relationship between the differential scattering cross-section in the CM-system and that in the laboratory system follows from the transformation formulae for the scattering angles between the two coordinate systems [33,34,37]. The laboratory differential scattering cross-section, $\sigma^s(\theta)$, can be derived as a function of either the CM-scattering angle, θ_{CM} , [37] or the laboratory scattering angle, θ , [40] and is given by

$$\sigma^s(\theta) = \frac{(1 + \gamma^2 + 2\gamma \cos \theta_{\text{CM}})^{3/2}}{|1 + \gamma \cos \theta_{\text{CM}}|} \sigma(\theta_{\text{CM}}) = \frac{(\gamma \cos \theta + \sqrt{1 - \gamma^2 \sin^2 \theta})^2}{\sqrt{1 - \gamma^2 \sin^2 \theta}} \sigma(\theta_{\text{CM}}), \quad (1.12)$$

where $\gamma = A^{-1} = M_P / M_T$. A relation similar to Eq. (1.12) can also be obtained for the differential recoil cross-section, $\sigma^r(\phi)$, which is a measure of the probability of recoiling a target atom into a particular angle, ϕ , at the outcome of a collision with a projectile. $\sigma^r(\phi)$ is given by [40]

$$\sigma^r(\phi) = 4 \sin(\theta_{\text{CM}}/2) \sigma(\theta_{\text{CM}}) = 4 \cos(\phi) \sigma(\theta_{\text{CM}}). \quad (1.13)$$

Examples of differential scattering cross-sections $\sigma^s(\theta)$ as a function of the scattering angle θ are shown in Fig. 1.4 for 2.5 keV Ar projectiles scattering from O and Br atoms (solid curves). $\sigma^s(\theta)$ decreases monotonically with θ when the projectile is lighter than the target (Ar→Br). For projectiles heavier than the target, $\sigma^s(\theta)$ exhibits a high-energy branch and a low-energy branch in accord with Eq. (1.1). The former results from collisions with large impact parameters and has a higher cross-section than the latter. Both branches come together at the critical scattering angle expressed by Eq. (1.2). For Ar scattering from O this angle is 23.6°.

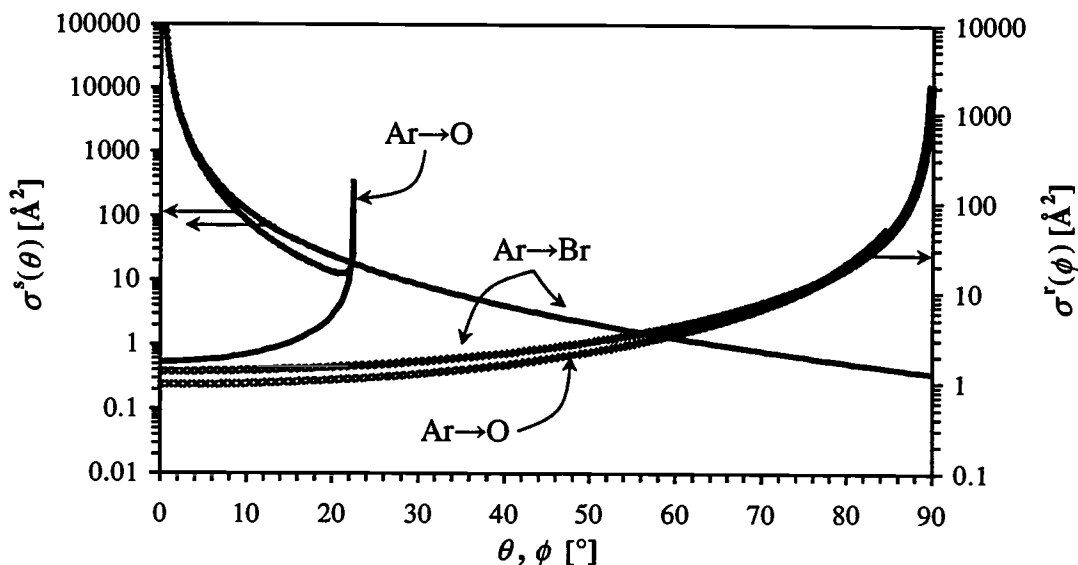


Fig. 1.4 Calculated differential scattering [$\sigma^s(\theta)$] and recoil [$\sigma^r(\phi)$] cross-sections as a function of the scattering angle θ and recoil angle ϕ . 2.5 keV Ar is incident on O and Br. Cross-sections were calculated using the Molière potential and the Firsov screening length (see Section 1.6.3 for definitions).

Fig. 1.4 also shows the corresponding differential recoil cross-sections $\sigma^r(\phi)$ for O and Br as a function of the recoil angle ϕ (crosses). One observes a monotonic increase of $\sigma^r(\phi)$ with ϕ . Although Fig. 1.4 only includes O and Br recoils, the general trend of $\sigma^r(\phi)$ as function of increasing target mass is an increase in cross-section.

Finally, Fig. 1.5 displays the dependence of the differential recoil cross-section on the projectile's initial kinetic energy E_0 for a C atom recoiled into an angle $\phi = 45^\circ$ by collisions with He, Ne, Ar, and Kr. From Fig. 1.5 is seen that the differential recoil cross-section decreases with increasing energy as expected from Eq. (1.11). Furthermore, $\sigma^r(\phi)$ increases as the mass of the projectile atom increases.

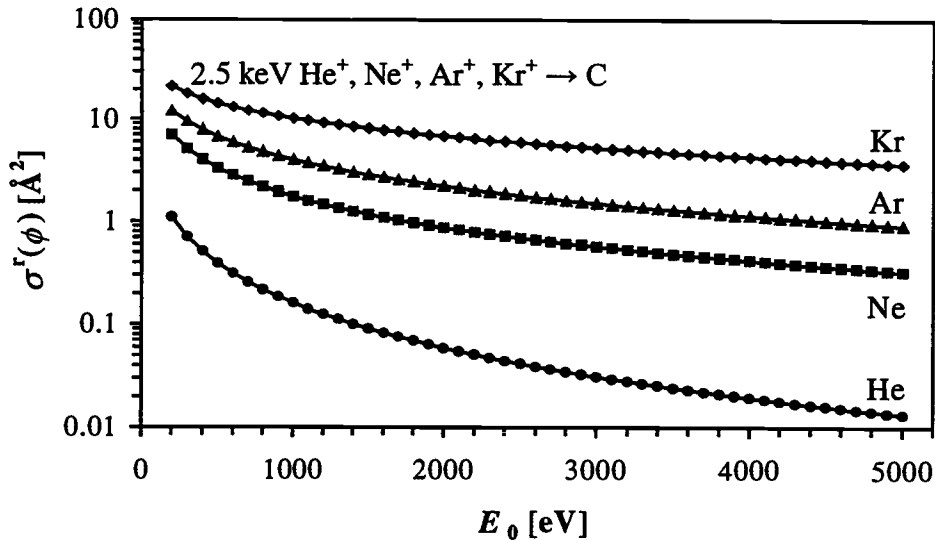


Fig. 1.5 Calculated differential recoil cross-section $\sigma^r(\phi)$ as a function of the projectile energy E_0 .
A carbon atom is being recoiled into an angle $\phi = 45^\circ$ by various inert gas projectiles. Cross-sections were calculated using the Molière potential and the Firsov screening length (see Section 1.6.3 for definitions).

1.6. The Binary Collision Computer Code MARLOWE

Chapters 4 and 5 below involve computer simulations performed with the binary collision code MARLOWE [29] (version 14c). Without going into detail about the specific simulations, for this will be done in the respective chapters, it is necessary to introduce MARLOWE and the physics that it is based on. The code, written in FORTRAN, and information about it is available from the Oak Ridge National Laboratory [41,42]. It is accompanied by a user's guide. Knowledge of FORTRAN programming is considered an essential asset for efficient use of the manual, which otherwise is rather user-unfriendly.

1.6.1. MARLOWE: Computer Simulation of Atomic Collisions in Crystalline Solids

The MARLOWE program simulates atomic collisions in crystalline targets using the binary collision approximation (BCA). It follows out the consequences of launching an energetic atomic projectile, from either an external beam or an interior

site, into a target [43]. The targets may have many material regions, each with its own arbitrary (triclinic) crystal structure and with many kinds of atoms. The program follows the slowing-down of the primary particle and, if desired, that of all target particles which are displaced from their lattice sites, until they either leave the target or fall below a selected low kinetic energy.

The particle trajectories are constructed as series of binary encounters between the projectiles and the initially stationary target atoms. Elastic scattering is governed by one of several interatomic potential functions. Inelastic effects are included in a low-energy approximation. A discussion of interatomic potentials and inelastic energy loss is given in Sections 1.6.3 and 1.6.4 below.

An associated program, TABULA, is also included in MARLOWE. It uses the MARLOWE interatomic potential energy functions to tabulate the classical scattering integrals and related quantities such as interaction cross-sections. It was used for Figs. 1.4 and 1.5 and for the study described in Chapter 5.

Some remarks regarding the use and applicability of the MARLOWE program in this work are necessary. As mentioned earlier in the objective of this project (Section 1.4), the broad goal of the computer simulations is to gain a better understanding of experimental TOF spectra and their interpretation. While the MARLOWE program was originally intended for simulations of atomic collisions in *crystalline solids*, it can also be used to simulate ion scattering off *liquids* as long as the molecules in the surface exhibit some collective orientational behavior. Additionally, azimuthal disorder in a surface can be simulated by allowing the incident ion to approach the target surface from random directions. This makes the transfer of results from solid-state targets to liquid surfaces more reasonable.

Finally, to the author's best knowledge, there does not exist a binary collision trajectory simulation program that models true liquid targets. Another program, called scattering and recoiling imagine code (SARIC) [44], was initially considered and used for simulations. However, because it is geared toward meeting the specific needs of the research group in which it originated, the use of SARIC was soon abandoned and MARLOWE was employed.

1.6.2. *The Binary Collision Approximation (BCA)*

The BCA involves several assumptions [45]. The atoms in an encounter are isolated from the rest of the system, implying that scattering lengths are less than typical interatomic distances in the target. The potential energy is neglected before and after each encounter, so that scattering may be evaluated as if the atoms began and ended infinitely apart. The colliding atoms are regarded as moving along their asymptotic straight-line paths. The interatomic forces are taken to be central and conservative; all inelastic (electronic excitation) energy losses are ignored in evaluating the scattering in the center-of-mass system. An encounter usually involves one moving atom and one initially stationary target atom; encounters between moving atoms are ignored. This reduces the scattering calculations to two dimensions.

The BCA as used in MARLOWE differs from treatments of elastic scattering found in standard texts [33,34]. The latter discuss the case where the scattered particles are detected in an apparatus at a macroscopic laboratory distance from the site of the collision. On this scale, the collision can be regarded as occurring at the initial target location. Only one scattering integral, the center-of-mass (CM) scattering angle, is needed [46]. In MARLOWE, however, the role of the detector is taken by the next collision partners of the scattered particles, which are located at typical interatomic distances of separation in crystals. In this situation, a second scattering integral, the so-called time integral, must be evaluated in order to locate the particle trajectories correctly in space and time. The classical equations of motion are solved in CM-coordinates to yield the CM-scattering angle, θ_{CM} , [33,34]:

$$\theta_{\text{CM}} = \pi - 2p \int_R^{\infty} dr [r^2 g(r)]^{-1} = \pi - p I_1 \quad (1.14)$$

and the time integral [29,47,48]:

$$\tau = (R^2 - p^2)^{1/2} - I_2, \quad (1.15)$$

where

$$I_2 = \int_R^{\infty} dr \left\{ [g(r)]^{-1} - (1 - p^2/r^2)^{-1/2} \right\}, \quad (1.16)$$

$$g(r) = \left[1 - p^2/r^2 - v(r) \right]^{1/2}, \quad (1.17)$$

$$v(r) = (1 + A) V(r)/A E_0, \quad (1.18)$$

r is the interatomic separation, p the impact parameter, $V(r)$ the interatomic potential energy, and R is the apsis (distance of closest approach) in the collision, defined by $g(R) = 0$. Robinson [45,46] discussed methods and numerical algorithms of evaluating the scattering integrals accurately. His approach includes Eqs. (1.14) to (1.18) and more on evaluating differential scattering cross-sections. MARLOWE follows these algorithms closely.

1.6.3. Interatomic Potential Energy Functions in MARLOWE

While users of MARLOWE may supply their own procedures, the program supports five interatomic potential energy functions:

(1) The Molière potential [49];

a repulsive Coulomb potential screened by a sum of three exponentials, designed as an approximation to the Thomas-Fermi screening function. This potential energy function was used in most simulations described in this work. It is represented by

$$V(r) = (Z_1 Z_2 e^2 / r) \sum_{i=1}^3 \alpha_i \exp(-\beta_i r/a_{i2}), \quad (1.19)$$

where the Z_i are the atomic numbers of the colliding atoms, r is their separation, e is the electron charge,

$$\alpha = \{0.35, 0.55, 0.10\}, \quad \beta = \{-0.3, -1.2, -6.0\}, \quad (1.20)$$

$$a_{12} = a_F = (9\pi^2/128)^{1/3} a_0 (Z_1^{1/2} + Z_2^{1/2})^{-2/3}, \quad (1.21)$$

and a_0 is the Bohr radius, 0.529 Å. a_F describes the screening length as introduced by Firsov [50]. The Molière potential is probably the most widely used interatomic potential energy function because it is particularly efficient computationally.

(2) The ‘universal’ ZBL potential [51];

a generalization of the Molière potential which it includes as a special case, but is less efficient since the parameters are completely general. It takes the form of Eq. (1.19), except that $i = 1, \dots, 4$ and

$$\begin{aligned} \alpha &= \{0.1818, 0.5099, 0.2802, 0.02817\}, \\ \beta &= \{-3.2, -0.9423, -0.4028, -0.2016\}, \end{aligned} \quad (1.22)$$

$$a_{12} = (9\pi^2/128)^{1/3} a_0 (Z_1^{0.23} + Z_2^{0.23})^{-1}. \quad (1.23)$$

Ziegler et al. [51] used a local density model, with electron distributions from self-consistent Hartree–Fock atomic wavefunctions and free electron corrections to the electron kinetic energy and for exchange and correlation, to evaluate interatomic potential energy functions. The resulting potentials for many pairs of atoms were then used as the basis for constructing an averaged ‘universal’ potential, given by Eqs. (1.19), (1.22), and (1.23).

(3) The average modified Lenz–Jensen (AMLJ) potential [52–54];

a repulsive Coulomb potential, screened by an exponential with a polynomial exponent,

$$V(r) = (Z_1 Z_2 e^2 / r) \exp(-\alpha_1 r + \alpha_2 r^{3/2} - \alpha_3 r^2), \quad (1.24)$$

where [54]

$$\begin{aligned}
\alpha_1 &= (1.706/a_0) \left(Z_1^{0.307} + Z_2^{0.307} \right)^{2/3}, \\
\alpha_2 &= (0.916/a_0^{3/2}) \left(Z_1^{0.169} + Z_2^{0.169} \right), \\
\alpha_3 &= (0.244/a_0^2) \left(Z_1^{0.0418} + Z_2^{0.0418} \right)^{4/3}.
\end{aligned} \tag{1.25}$$

The AMLJ potential is an alternative to the ZBL potential and may be the most accurate function currently available for calculations involving the binary collision approximation. It is based on calculations like those of Ziegler et al., but using atomic electron distributions with relativistic corrections, as well as confining the atoms to Wigner–Seitz cells representing the densities of the appropriate solids. The ZBL and AMLJ potentials were used in this work only for test purposes, which were to ensure that results drawn from simulations would not depend, to any significant extent, on the approximation used for the interatomic potential energy function.

(4) The Born–Mayer potential [55];

an exponential-sum screened Coulomb potential with parameters from Ref. [56].

(5) The Morse potential [57];

this potential is comprised of two exponentials, such that there is an attractive region outside a repulsive core. The Born–Mayer and Morse potentials were not considered in this work.

1.6.4. Modeling of Inelastic Energy Losses in MARLOWE

Robinson [46,58,59] discussed inelastic energy loss models used in MARLOWE in detail, and only a basic description for a general understanding shall be given in this context. The discussion will be limited to electronic stopping (electron excitations) which dominates over the nuclear stopping (excitations of the nucleus) in the low keV-energy range.

Besides losing energy in scattering from the atoms of the target, energetic particles also lose energy by exciting electrons, both those of the medium and those of the particles themselves. If such losses depend on the particle kinetic energy and the distance traversed, but are independent of the particular surroundings of a trajectory

segment (impulse approximation), they are termed *nonlocal* inelastic losses. Here, elastic and inelastic energy losses are uncorrelated. The rate of energy loss by electron excitation is the *electronic stopping power* [59]

$$(-dE/dx)_e = n S_e(E), \quad (1.26)$$

where n is the atomic density of the target and $S_e(E)$ is the electronic stopping cross-section, so called because it has the units of energy times area. The stopping power in Eq. (1.26) is a force:

$$\begin{aligned} (-dE/dx)_e &= -mv \, dv/dx \\ &= -m \, dv/dt = -m\ddot{x}, \end{aligned}$$

where m and v are the mass and speed of a fast particle. Thus, a decelerating force $-n S_e(E)$ can be added to the equations of motion of energetic particles. At low energies (< 25 keV [59]), $S_e(E)$ takes the form [60,61]

$$S_e = k E^{1/2}, \quad (1.27)$$

where E is the projectile kinetic energy and the parameter k is derived from experiment, from the LSS (Lindhard–Scharff–Schjøtt) theory [61,62], or otherwise.

An alternative formulation of the inelastic stopping problem incorporates strong correlation between the elastic and inelastic energy losses. It makes the energy lost inelastically in a collision depend on how closely two atoms approach each other. These losses are termed *local* and become significant at higher collision energies. Oen and Robinson's expression for the stopping cross-section then becomes [63]

$$S_e^{\text{OR}} = 2\pi \int dp [p Q(p, E)] = k E^{1/2} D, \quad (1.28)$$

with

$$Q(p, E) = k E^{1/2} (\gamma^2 / 2\pi a^2) \exp[-\gamma R(p, E)/a], \quad (1.29)$$

where $R(p,E)$ is the collision apsis, a is a screening length, and γ is a parameter (0.3 [63]). Under the conditions of the impulse approximation, the deflection function D in Eq. (1.28) is unity, but it is smaller at lower energies.

MARLOWE supports both the local and the nonlocal inelastic energy loss models represented by Eqs. (1.27) and (1.28). Both were included as occurring simultaneously in the computer simulations that are part of this work.

1.7. Dissertation Outline

This dissertation adheres to the manuscript style, i.e. the following chapters, except Chapter 2, are reproductions of articles that either have been published by this author or are in the submission stage of the publication process. Chapter 2 is written in the manuscript style and constitutes a much more expanded version of Ref. [27]. It is devoted to the first part of this project's objective as mentioned in Section 1.4 above. It discusses the design and capabilities of the time-of-flight spectrometer built by the author and his close co-worker, Tom Gannon [64], for the investigation of surface properties of liquids. The focus will be placed on the author's contributions to the construction efforts, and proper credit will be given to Tom Gannon for components solely contributed by him which are included for completeness sake. The effects of varying experimental parameters and geometries will be discussed based on data obtained from the initial testing.

Chapters 3, 4, and 5 talk about issues that are related to the quantification of results obtained from time-of-flight spectra in direct recoil spectrometry (TOF-DRS). First, the detection efficiency [65] of a channel electron multiplier, the detector of choice in TOF scattering and recoiling experiments, is investigated for low energy noble gas ions. The results obtained are generalized into a functional expression for the detection efficiency of any atomic specie recoiling from the target surface and striking the detector. This quantity is particularly important for the conversion of experimental data from raw TOF spectral peak intensities to absolute elemental surface concentrations for compositional and orientational analysis.

Chapter 4 reports the results of a computer simulation study [66] aimed at a better general understanding of experimental TOF spectra obtained by DRS. TOF spectra exhibit characteristic peak shapes whose detailed origin is not well understood to date. Scattering experiments are simulated and the collision history of atoms directly recoiling from model targets due to ion bombardment is investigated. Here, depth distributions of recoils and multiple scattering mechanisms are of particular interest. Simulated TOF spectra are compared to experimental data.

Beside the detection efficiencies addressed above, interaction cross-sections between the primary projectile and any type of target atom are also extremely important for quantitative surface analysis by DRS. In the author's laboratory, recent work has been focusing on the determination of the surface composition and average orientation of molecules in low vapor pressure molecular and ionic liquids [67,68]. These organic liquids consist primarily of H and C. Experimental and theoretical cross-sections from the literature for low-energy (1 to 10 keV) atomic interactions involving hydrogen have consistently been at variance. Chapter 5 discusses the origin of this discrepancy and describes an approach [69], combining experiment and computer simulation, to improve the convergence of calculated cross-sections involving H with experimentally derived ones. Particularly, a correction factor to the screening radius, specific to H, in interatomic potentials is proposed.

Finally, Chapter 6 constitutes a summary of the most important conclusions that can be drawn from this work.

Chapter 2

Ion Scattering and Recoiling from Liquid Surfaces

Michael Tassotto

2.1. Introduction

This chapter describes the design and performance of a unique time-of-flight scattering and recoiling spectrometer, which constitutes the backbone of a new method to study liquid surfaces. The significance and motivation for this work were discussed in detail in Chapter 1. The intent is to provide experimental molecular-level data on the composition of liquid surfaces and the average orientation of their constituent molecules in order to supplement data obtained through molecular dynamics and related computational techniques. The expectation is that experiments utilizing this new method will provide significant insight into such fundamental questions of liquid behavior as:

- What are the structure–property relationships that operate at the liquid–vapor interface? Can one formulate predictive rules that will link the segregation and orientation of molecules at the liquid surface with their structure, the presence of particular functional groups, and the presence of H–bonding?
- What is the surface concentration of solutions? How do experimental results compare with the predictions of thermodynamics and statistical mechanics?
- To what extent does chain-end accumulation occur at the surface of e.g. hydrocarbons?

If the method of time-of-flight scattering and recoiling spectrometry (TOF–SARS) can be extended to aqueous solutions, then this work has potential to also contribute to some important technological issues concerning, for instance, the segregation and orientation of pollutants or bio-active molecules at solution surfaces.

Ion scattering techniques require a vacuum for the transport of ions to the sample and on to the detector. When analyzing surfaces of solid-state materials, ultra-high vacuum conditions and surface purity are obtained in a number of ways. Outgassing of the instrument through baking at elevated temperatures, repeated annealing cycles, sputter cleaning of the sample surface by ion bombardment, and exposure of the sample to reactive gases such as O_2 and H_2 are some possibilities. However, this does not apply to liquid samples. Introducing liquids into a vacuum poses some concerns. The base pressure in the vacuum chamber containing the liquid is now largely

dominated by the liquid's vapor pressure. An increase in base pressure causes a decrease in the mean free path of the ions used for analysis and an increase in the rate of adsorption at the liquid's surface.

Contamination of the surface under investigation can be kept to a minimum by creating a continuously refreshed surface. The right balance has to be found between two time scales, τ_{eq} and τ_{ad} . τ_{eq} represents the time it takes molecules – having been displaced from the bulk to the surface of a liquid – to reorient themselves and reach equilibrium. τ_{ad} is the time required to form a monolayer of gas on a surface due to adsorption. Order-of-magnitude estimates for τ_{eq} can be obtained, for example, from dynamic methods of surface tension measurements [70]. The surface tension of water relaxes to its equilibrium value with a relaxation time of $\tau_{eq} \cong 0.6$ ms, while some surfactant solutions exhibit τ_{eq} -values in the 20-ms range. τ_{ad} is difficult to estimate because it is not solely related to the quality of the vacuum via the rate of collisions the molecules in the gas phase undergo at the liquid surface. Most importantly, it is also related to the so-called *sticking probability*, P_s , which can vary widely over many orders of magnitude. If every gas molecule hitting the surface is trapped, P_s is unity. A 'rule-of-thumb', frequently used by researchers in surface science, comes from the kinetic theory of gases and estimates that it takes about one second to form one monolayer of adsorbed air molecules at a pressure of 10^{-6} Torr, assuming $P_s = 1$. At the same pressure of 10^{-6} Torr and 273 K, Hudson [71] lists the monolayer time for N_2 gas on a surface as $\tau_{ad} \cong 2.5$ s. The sticking probability strongly depends on such factors as the gaseous specie's kinetic energy and reactivity, the degree to which the surface is already covered, and structural properties of the surface itself. Therefore, the foregoing considerations need to be kept in mind when designing the liquid-sample introduction system.

Unlike in ion scattering off solid materials, beam damage to the surface of liquid samples during the measurement period will not be of any concern. Suppose a freshly created liquid surface with atom density n_0 is exposed to an ion beam for a length of time t . An average pulsed ion beam current of $I_p \leq [(D/100) \cdot n_0 \cdot e]/(\gamma t)$ would cause a maximum beam damage of D percent. γ and e are the sputter yield and the elementary

charge, respectively. For example, assume there are 5×10^{14} carbon atoms/cm² in a liquid polymer surface, the sputter yield is unity, and the same surface area is exposed to ion bombardment for $t = 1$ s before the beam samples a refreshed surface. Then, a 0.1% beam damage to the surface, which is equivalent to the removal of 0.1% of a monolayer of C atoms, would require an average pulsed ion current of 80 nA/cm². Given a sweep rate of 20 kHz and pulse width of 100 ns, this corresponds to a continuous ion current of $(80 \text{ nA/cm}^2 \div 20 \text{ kHz} \div 100 \text{ ns} =) 40 \text{ }\mu\text{A/cm}^2$, which is about a factor of 10^3 larger than commonly seen in ISS experiments. The duration of bombardment ($t = 1$ s) is in itself an overly conservative assumption and, thus, the liquid polymer surface suffers virtually no damage from the ion beam.

It is essential that the ion source used in the time-of-flight (TOF) spectrometer can produce a variety of noble gas ions such as He⁺, Ne⁺, and Ar⁺ to serve as projectiles. The ion source's ability to produce sufficient quantities of multiply charged ions would be beneficial in extending the range of kinetic energies of the primary projectiles beyond the maximum acceleration potential.

It is critical that the ions be mass selected. Ions created from residual gases such as H₂O⁺, O⁺, N⁺, N₂⁺, and O₂⁺ need to be well separated from the noble gas ion of choice. The species Ne⁺ and H₂O⁺ are within 2 amu (atomic mass unit) of each other and exhibit the lowest mass difference of real concern. A resolution of about 1 amu should therefore suffice. It would be valuable to be able to check with a mass spectrometer that this purity is really being achieved.

The ion beam should be uniform across the impact area on the sample surface, and its intensity should not drift. The energy spread of the beam needs to be kept to a minimum in order to guarantee the best conditions for a mono-energetic ion beam.

Working with liquid samples requires that the main chamber housing the sample cell must be isolated from the rest of the vacuum system by small-diameter apertures facilitating differential pumping of the various parts of the spectrometer. Particularly, the ion gun and detector regions must be protected from contamination for obvious benefits such as prolonged life expectancy for filaments and stable detector characteristics (constant gain).

The number and quality of experiments that actually get done strongly depends on the ease of use of the spectrometer. Changing of sample fluids should be possible while maintaining a vacuum in most sections of the apparatus. It must be easy to steer the beam from the ion source to the sample and to check the beam profile quality and current, even while adjusting knobs.

For some experiments, it will be necessary to control the target temperature. This may include heating the sample beyond its melting point above room temperature or wanting to keep the temperature of the sample liquid constant about a particular value.

Finally, it would be ideal if experimental parameters such as the angle of beam incidence with respect to the sample surface (α) and the detector angle with respect to the initial direction of the primary ions (θ, ϕ) could be varied freely. While the former is readily made possible by a suitable sample manipulator and support, the latter can turn out to be cost-prohibitive. Multiple TOF legs, each with a separate particle detector, would provide a discrete choice of scattering and recoiling geometries. A freely variable detector angle is ideal but possible only if the TOF leg becomes part of the main chamber with the detector moving along a circular path about the target position. This would force a considerable increase in chamber volume and, thereby, constitute a much larger gas load for the vacuum pumps.

The spectrometer built meets many of the goals discussed above. Its design is based closely on the successful TOF-SARS machine used for solid materials by Rabalais and co-workers [72]. It has been shown to date to be able to serve as a useful tool to probe the surface composition and molecular structure of liquid surfaces, in particular those of a liquid siloxane and glycerol [27], bis(2-ethylhexyl)phthalate and bis(2-ethylhexyl)-chlorendate [67], and, for the first time, a room-temperature ionic liquid [64,68]. Details of the spectrometer design and operating methods are discussed in the following Section 2.2. The performance is demonstrated in the context of a number of exemplary TOF spectra in Section 2.3.

2.2. Spectrometer Design

2.2.1. Overview

The design of the TOF spectrometer is shown schematically in Fig. 2.1. There are five main components of the spectrometer: the ion source, the mass/velocity (Wien) filter, the first collimation region and pulsing optics, the target chamber with the sample cell, and the particle detector at the end of the drift tube. The ions are produced, extracted and formed into a continuous beam in the ion source, mass and velocity selected by a Wien filter, and collimated onto an aperture (behind d_2 in Fig. 2.1). The collimated beam is swept across the aperture in a square-pattern-like regime to create ion pulses, which are steered through another aperture (f_2) onto the sample. Collision products leaving the surface into the proper direction of the detector traverse the field-free drift tube before entering the channel electron multiplier.

2.2.2. Ion Source

The ion source currently in use is an ion sputtering gun (Model IG35/70, OCI Vacuum Microengineering) that utilizes hot-cathode emission to ionize noble gas atoms via electron impact. It is capable of producing ion beams with a total current of up to $\sim 1 \mu\text{A}$ at the exit aperture of the gun, depending on the beam energy and the gas used. The ion energy to ground is defined by the bias potential (0–2.5 kV) applied to the ionizer region in the gun. Generally, the lighter the ion mass and the lower the bias potential, the smaller the beam current will be. From experience, the useful bias potential range is limited to ≥ 1.0 kV due to a rapidly decreasing beam current at the sample position, which is about 75 cm down-beam from the gun.

Fig. 2.1 Schematic drawing of the major components of the time-of-flight ion scattering and recoiling spectrometer.
a – ion source, b – Wien filter, c – deflector plates, d – beam position monitor, e – Einzel lens, f – differential pumping aperture, g – Faraday cup.
B indicates the magnetic field of the Wien filter.

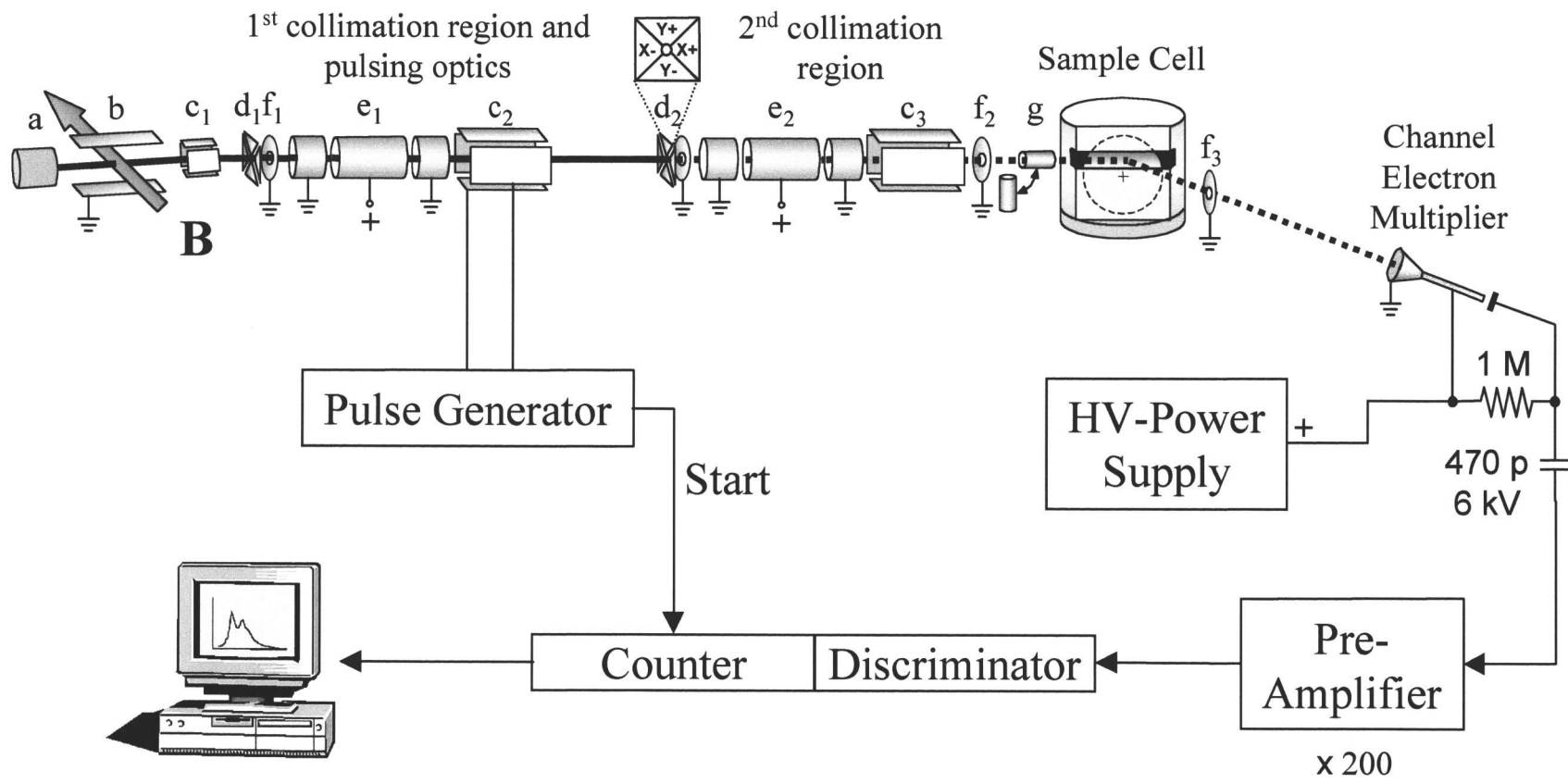


Fig. 2.1

2.2.3. Mass and Velocity Selection

A Wien filter with static crossed magnetic and electric fields is used in the spectrometer's beam line for mass and velocity selection of the inert gas ions. Fig. 2.2 shows a schematic drawing of the design. The beam diameter on the object side is defined by the ion gun's exit aperture, which is exchangeable from 3 to 5 mm and serves as the filter's entrance diaphragm. A 2-mm differential-pumping aperture located at the end of the drift region constitutes the exit diaphragm where the separation of ions occurs. In order to reduce edge effects at the entrance to and exit of the Wien filter, so-called μ -metal (Co-Netic[®] metal) with high permeability was made into shielding tubes that are slightly larger than the beam diameter. The edge effects of the fields within the filter were reduced by making the transverse dimension of the electric deflector plates (28 mm) and the pole tips of the permanent magnet (25 mm) substantially larger than the beam diameter.

Selection of different ions is facilitated by changing the positive voltage applied to the upper deflector plate while the magnetic field strength of the permanent magnet (1200 Gauss) remains constant. It is crucial that the ion beam be stripped of the flux of neutral particles. This is accomplished by putting the ion source off axis by a $\sim 4^\circ$ bend of the port aligner following the Wien filter in the beam line (see Fig. 2.2a).

Solov'ev and Tolstoguzov [73] derived an analytical expression for the mass dispersion of a Wien filter with uniform orthogonal fields. It was used to determine the optimal (necessary and minimal) distance between the end of the deflector plates and the exit diaphragm (drift region) in order to achieve the desired mass separation. The displacement, y_d , of the image of the filter's entrance diaphragm, e.g. the ion gun's exit aperture, along the vertical axis in the plane of the exit diaphragm, e.g. aperture f_1 in Fig. 2.2a, is given by [73]

$$y_d \equiv \frac{|M_p - M_{res}|}{M_p} \times \frac{l}{2\theta_1} \times \left(1 - \cos \theta_1 + \frac{d}{l} \theta_1 \sin \theta_1 \right), \quad (2.1)$$

where

$$\theta_1 = l B_0 (2\eta / U)^{1/2} / 2, \quad (2.2)$$

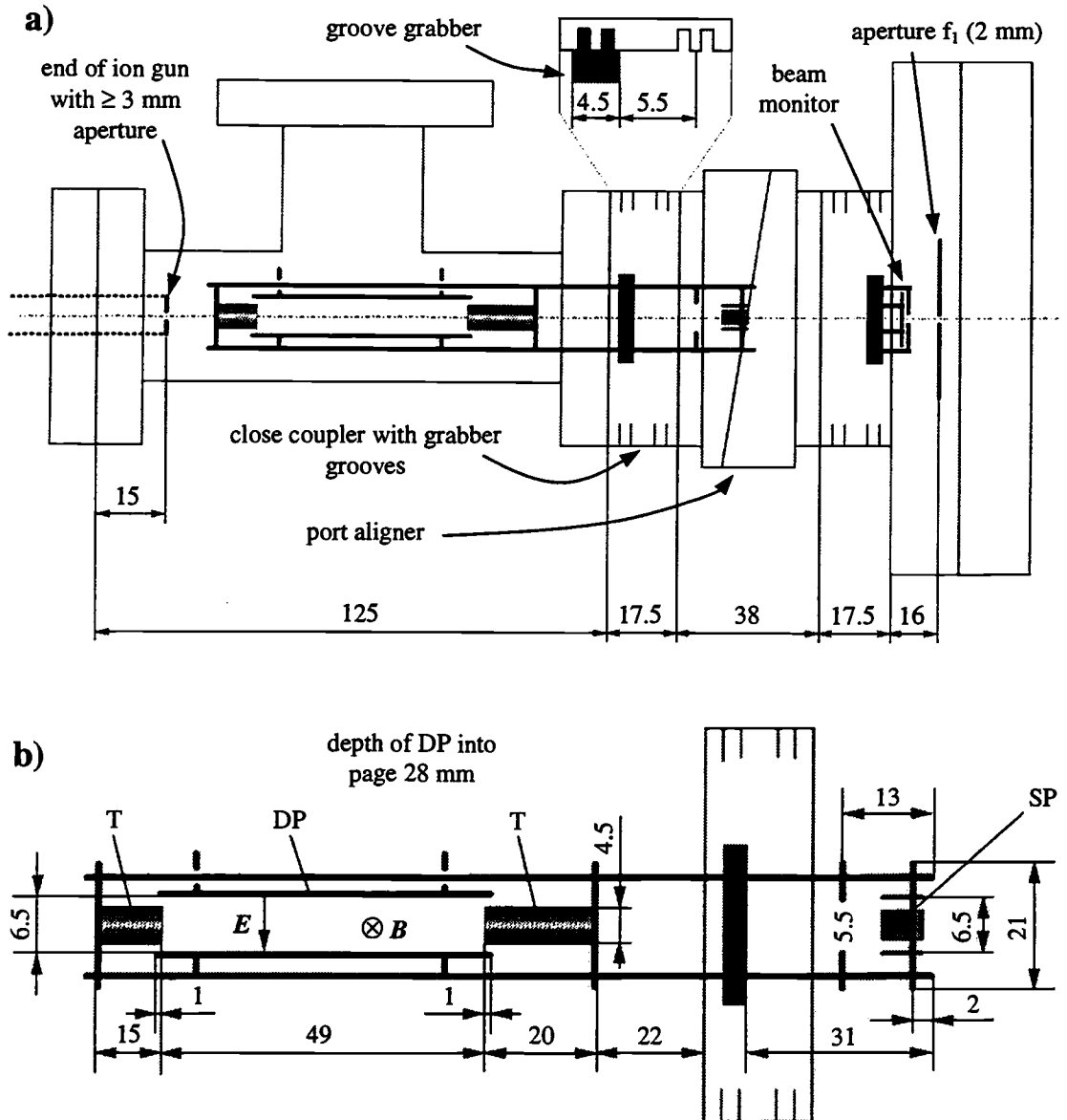


Fig. 2.2 Schematic drawing of the Wien filter assembly.
 a) Position of Wien filter, X/Y-steering plates (SP), and first beam position monitor in vacuum system. The ions enter from the left. b) Close-up of Wien filter design. Co-Netic[®] magnetic shielding tubes (T) are included for the purpose of fringe field reduction. The electric and magnetic fields are indicated by vectors E and B , respectively, with B pointing into the page. A variable, positive voltage on the upper deflector plate (DP) provides E , with the lower DP at ground potential. All dimensions listed are in mm.

M_P is the mass of the projectile ion of interest, M_{res} is the mass of the residual gas one wants to remove from the beam, l and d are the length of the deflector plates and the drift region, respectively, B_0 is the magnetic field strength, U is the beam acceleration voltage, and $\eta = ne/M_P$ is the charge-to-mass ratio of the separated ion. Eq. (2.1) is plotted in Fig. 2.3 for the most crucial cases of separating singly charged residual gas molecules such as H_2O^+ from Ne^+ ions and O_2^+ and N_2^+ from Ar^+ ions. U was set to the highest value possible with this ion gun, 2.5 keV, at which the smallest separation occurs. In the design of the Wien filter, aperture f_1 is located at a drift length $d = 130$ mm, as indicated by the solid vertical bar in Fig. 2.3. An inert gas ion passes through the Wien filter undeflected, while the residual gas molecule misses the aperture f_1 due to its different mass.

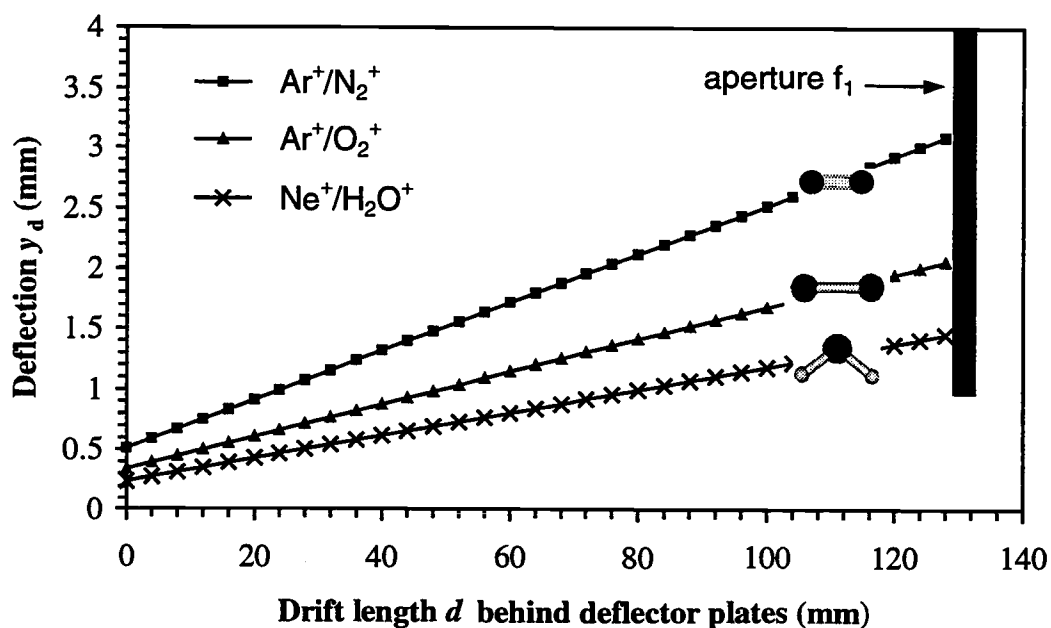


Fig. 2.3 Plot of the vertical deflection (due to changes in mass) of charged residual gas molecules as a function of their location behind the Wien-filter deflector plates.

The projectile energy is 2.5 keV. Only the cases of smallest separation and, thus, of biggest concern are shown. Other mass combinations between projectile ions and residual gas molecules exhibit better separations. The vertical bar indicates the location of the exit diaphragm (aperture f_1) as used in the TOF spectrometer design.

Fig. 2.3 takes into account only the dispersion in mass, $\Delta M/M_P$. The displacement y_d as a result of an identical relative change in energy ($\Delta E/E_P = \Delta M/M_P$) is equal in magnitude but opposite in sign [73].

2.2.4. Ion Optics

The first and second collimation regions schematically shown in Fig. 2.1 make up the ion optics of the TOF spectrometer. The original assembly of the ion optics was performed by co-worker T.J. Gannon and was closely based on a functioning design provided by J.W. Rabalais from the University of Houston, Texas. Some lens dimensions and wiring details were subsequently changed by the author, and a photograph of the ion optics currently in use is shown in Fig. 2.4. Two sets of an Einzel lens combined with a pair of horizontal and vertical deflector plates follow each other. A 1-mm aperture is placed between them. The purpose of collimation region 1 is to focus the ions and sweep them across the aperture in order to chop up the continuous beam into pulses.

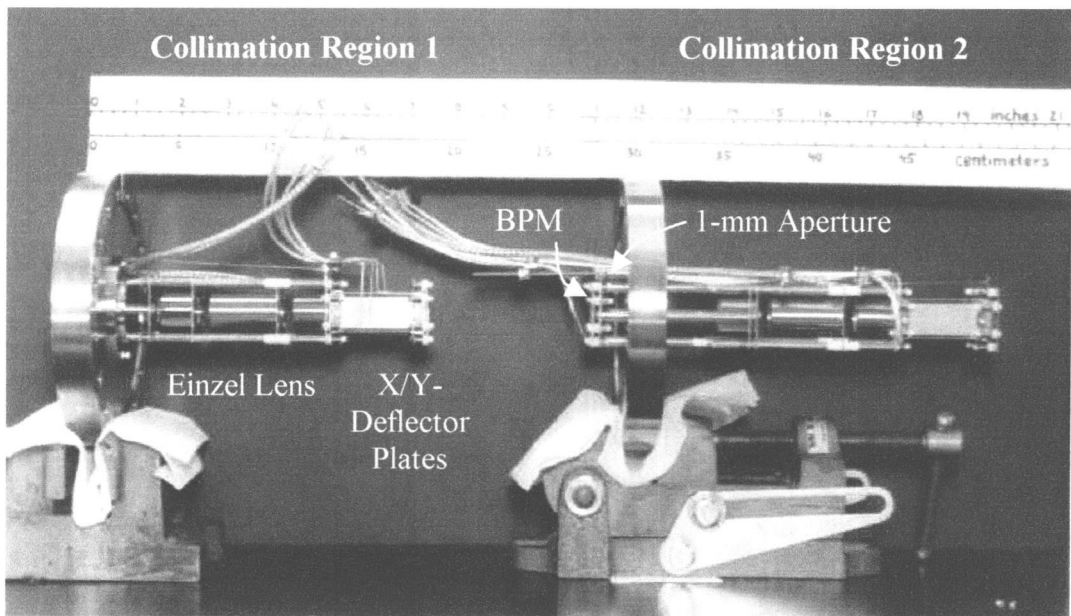


Fig. 2.4 Photograph of the ion optics assembly. A beam position monitor (BPM) is located immediately in front of the aperture used for pulsing the ion beam.

Collimation region 2 refocuses the ion pulses and directs them through another 1-mm aperture (f_2 in Fig. 2.1) onto the sample.

The (high) voltage requirements not only for the electrostatic lenses and deflector plates in collimation regions 1 and 2 but also for the Wien filter were met in this research group by designing and constructing an in-house, custom-made power supply [64,74]. Substantially lower costs compared to commercially available devices and exactly matching specifications are only two of the many advantages this power supply provides.

2.2.5. Beam Pulsing Scheme

In order to produce a pulsed ion beam with a high signal-to-noise ratio, a square-pattern-like pulsing regime as shown schematically in Fig. 2.5 has to be followed. A voltage difference applied to the vertical deflector plates (Y) is followed by an identical pulse applied to the horizontal plates (X). The delay $\delta = l(2E_0/M_P)^{-1/2}$ is the time it takes an ion of mass M_P and energy E_0 to traverse the length l of the deflector plates. The duration of each voltage pulse is 2δ . The trigger pulse (T) starting the

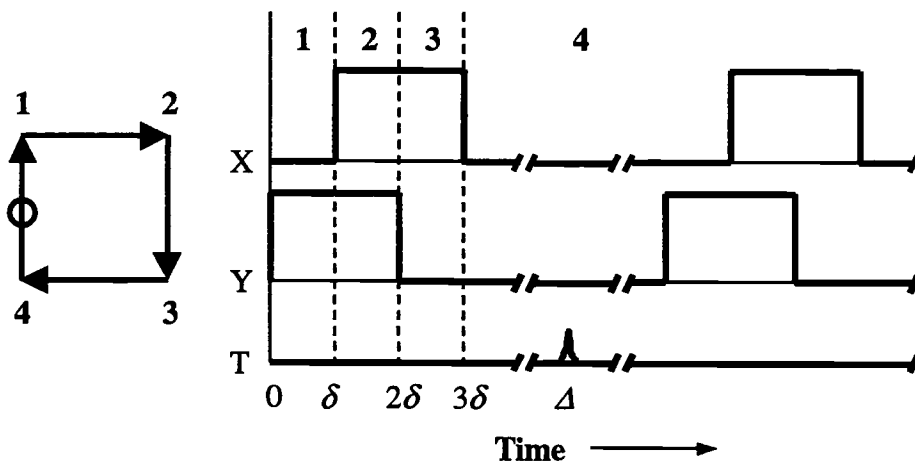


Fig. 2.5 Schematic diagram of the pulsing regime and voltage-pulse sequences. Numbers 1–4 indicate the positions of the ion beam at different times as the voltages on the vertical (Y) and horizontal (X) deflector plates are varied. The trigger pulse (T) starts the counting electronics. δ and Δ are defined in the text.

counting electronics (described in detail in Section 2.2.9) is usually set to the instant, Δ , at which an ion is 1 μs away from striking the sample surface. In this way, the so-called photon pulse caused by x-rays generated in inelastic collisions in the target surface can be seen in the TOF spectrum and provides a convenient way to calibrate time zero.

2.2.6. *Differential Pumping*

Dealing with ion scattering off liquid samples and the need to be able to acquire data over extended periods of time makes differential pumping a crucial requirement. Both the ion source and the particle detector need to be protected from contamination by sample vapor. The spectrometer's vacuum system is shown schematically in Fig. 2.6. A 2-mm aperture separates the ion source and Wien filter from the beam collimation regions. The latter are separated from the main chamber containing the sample cell by a 1-mm aperture that reaches into the main chamber as close to the sample surface as possible. The goal is to keep the path length that the projectile ions have to traverse in sample vapor to a minimum in order to avoid gas-phase scattering. Another aperture was planned as indicated in Fig. 2.6 (f_3 in Fig. 2.1) along the outgoing trajectory. However, the horizontal plane going through the center of the 6-inch flange through which the ion beam enters the main chamber is offset by $\sim 1/8$ inch (higher) from the horizontal plane defined by the center of the 6-inch flange through which scattered and recoiled particles, heading for the detector, exit. This is due to a flaw in the original manufacture of the main chamber, which was recycled from another apparatus. A pneumatic valve isolating the detector from the rest of the system is kept closed at all times except for data acquisition. Any possible contamination of the detector is thereby kept to a minimum.

The vacuum in the collimation regions, the main chamber, and part of the TOF arm is maintained by diffusion pumps (DP) that are backed by rotary pumps. A water-cooled baffle (above DP1) and two cold traps help to prevent pump oil from backstreaming into the vacuum system. The ion source and the detector are continually evacuated by a molecular dragpump and a turbo molecular pump,

respectively. Both provide very clean vacua compared to diffusion pumps. A specially designed control unit powers all diffusion pumps. This is a safety feature that is to prevent any damage to the pumps or other components of the TOF spectrometer in cases of power or equipment failures (see Section 2.2.10.2 below).

Fig. 2.6 Schematic drawing of the spectrometer's vacuum system. The differential pumping aperture between the sample chamber and the time-of-flight arm is currently removed due to slightly misaligned entrance and exit flanges (1/8 inch off) in the recycled sample chamber. The pneumatic valve is opened only during data acquisition in order to keep the detector from being contaminated.

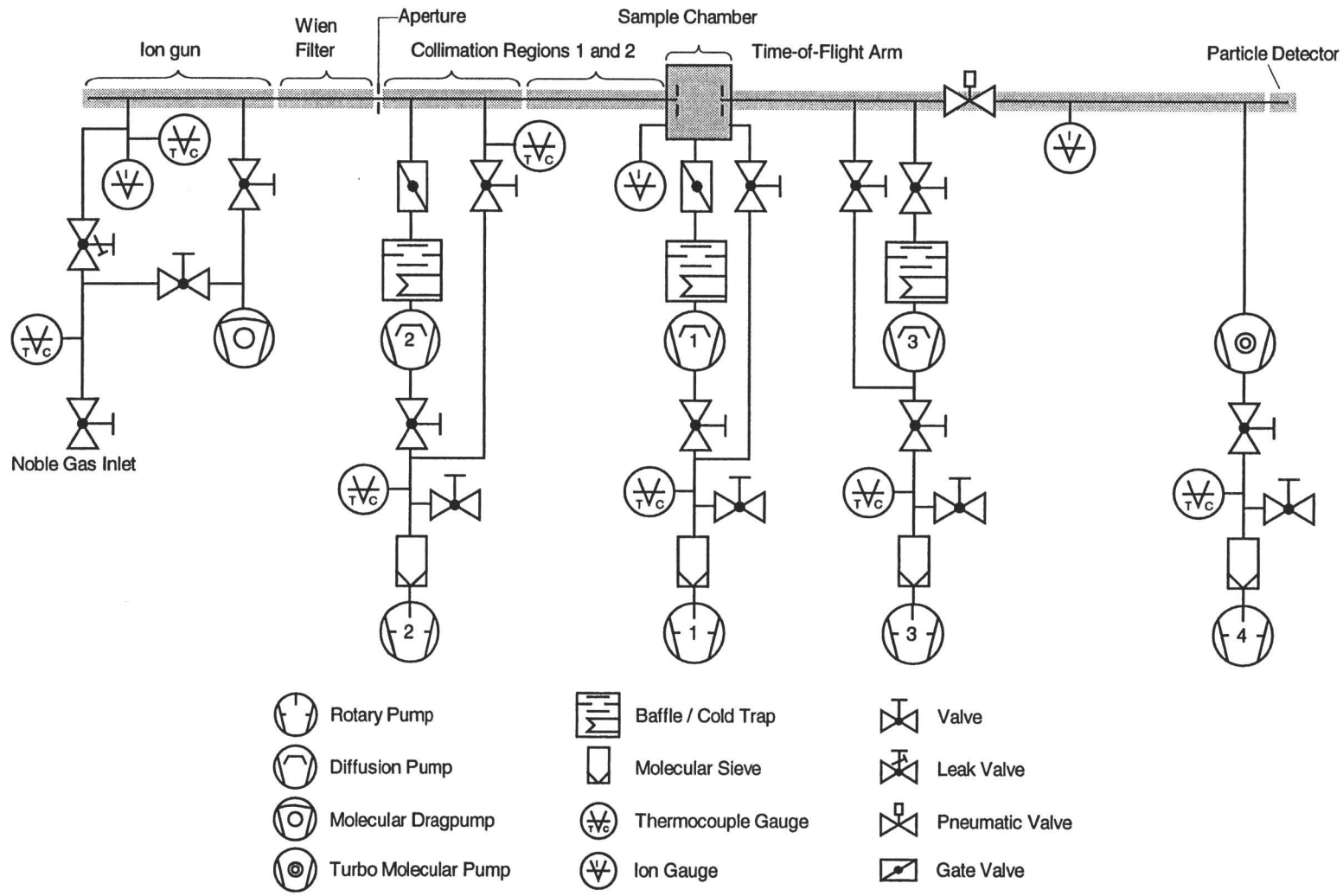


Fig. 2.6

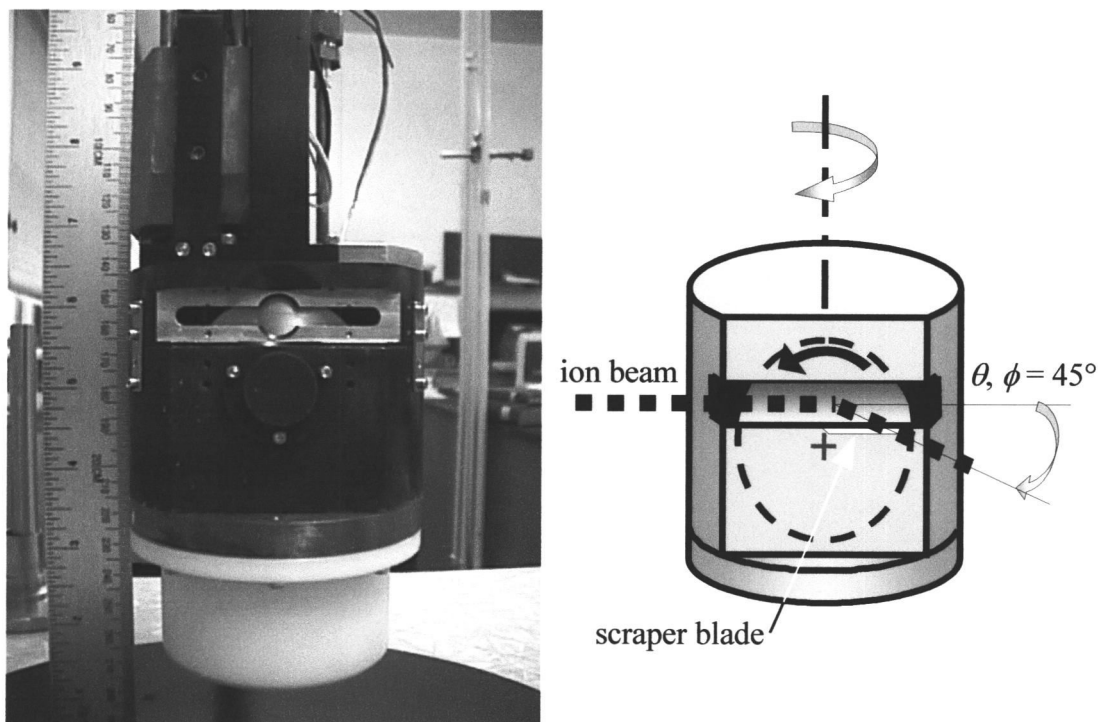


Fig. 2.7 Photograph and schematic drawing of the liquid sample cell. The cell is mounted to a manipulator, which allows rotation about a vertical axis going through the center of the stainless steel wheel's front surface. The cooling jackets for the motor driving the wheel are seen in the upper left part of the picture.

2.2.7. Sample Introduction

A successful design that Nathanson and co-workers [75] have used for their molecular beam scattering studies of liquid surfaces was exploited for this work. The sample cell currently in use was built by John Archibald and is shown in Fig. 2.7 along with a schematic drawing detailing the working principle. A rotating stainless steel wheel dips into a reservoir holding the liquid sample. The liquid film passes by a knife-edge which leaves a fresh surface behind, $\sim 0.1\text{--}0.2$ mm thick. The period of rotation is 2.7 s. As mentioned earlier in Section 2.1, when designing the liquid-sample introduction system for a continuously refreshed liquid surface the balance between two time scales – molecules reorienting and equilibrating themselves and gas-phase species adsorbing at the surface – has to be kept in mind. The ion beam

interacts with the sample after a quarter revolution is complete, e.g. 0.67 s or 670 ms after the initial exposure of the new surface. This delay is long enough to allow the molecules in the surface to rearrange themselves and equilibrate. At the same time, it is also short enough so that residual gases do not form an appreciable fraction of a monolayer due to adsorption. The design of the rotating wheel is very effective in creating uncontaminated liquid surfaces. The only drawback of the current design might be reflected in the requirement of a minimum sample volume, about 5 mL, due to the size of the cell.

2.2.8. Particle Detection

A continuous dynode electron multiplier (DeTech 407–EIC, Detector Technology) is sensitive to electrons, photons, and both charged and neutral particles of sufficient energy. In this context, it is used for the detection of ions and neutral particles that are scattered by or ejected from the target surface due to ion bombardment. The high gain of the multiplier enables the output to be recorded with standard electronic circuitry, see Fig. 2.1. The detector is used for individual event detection, e.g. it is operated in the pulse counting mode, for which it was designed with a high gain of about 10^{7-8} . Chapter 3 outlines in detail the necessity of accurately knowing the detector's response to impinging particles and discusses the results obtained for the calibration of the detection efficiency of the multiplier.

2.2.9. Data Acquisition Electronics

In order to obtain experimental data using the TOF spectrometer described in this chapter, a variety of electronic devices both for shaping the ion beam and for processing the signals received in the detector is necessary.

It is convenient to measure ion currents hitting key apertures along the beam line, but as this represents the ions that are missing the proper path, it is often not productive to tune up the source using these currents. On-line Faraday cups are better, and there is one immediately following the 1-mm aperture (f_2 in Fig. 2.1) inside the main chamber right in front of the sample. A motion feedthrough rotates the Faraday

cup into the ion path when desired. Two beam position monitors (see Section 2.2.10.1 below) allow an estimation of the total ion current at different locations in the beam line. The current measuring devices used are a Keithley 614 Electrometer and a Keithley 480 Picoammeter.

The conversion of the continuous ion beam into a pulsed one is accomplished with a pulse generator that was specifically designed for the application in this spectrometer (Avtech AVR-G1-P-C-OSU3). It outputs three independent voltages, two pulses of 0–200 V with variable duration and delay between each other and one trigger pulse (5 V, 100 ns). The beam pulsing scheme was illustrated in Fig. 2.5 above. The trigger pulse is sent to the data acquisition unit, which is a multichannel scaler (EG & G ORTEC Turbo-MCS) that records the counting rate of events as a function of time. When a scan is started, the MCS begins counting input events in the first channel of its digital memory and advances to subsequent channels as the preselected dwell time per channel elapses.

The instant at which the trigger pulse is sent to the MCS is crucial. The delay, Δ , is normally set to the time it takes an ion to travel the distance from the end of the deflector plates in collimation region one to the sample surface. This time depends on the ion's mass, its energy and the distance, which was measured to be 41.7 cm. For 2.5 keV Ar^+ ions $\Delta = 3.67 \mu\text{s}$. Usually, the MCS is started one microsecond early in order to also record the photon peak, which is a more precise calibration of time zero. However, the Avtech pulse generator is handicapped in one important aspect, which is best illustrated by an example. The delay (or advance) of the trigger pulse can be chosen in the range of $0.8 \leq \Delta \leq 4.5 \mu\text{s}$. A second trigger pulse, here referred to as *phantom*, appears on an oscilloscope whenever $\Delta \lesssim 2.1 \mu\text{s}$. This pulse is real and adversely affects the data acquisition. A 2.5 keV Ne^+ ion traverses the 41.7 cm in just 2.59 μs . If one microsecond is subtracted in order to include the photon pulse, then $\Delta = 1.59 \mu\text{s}$, which falls into the range where the *phantom* pulse shows up. Therefore, the toggle switch on the Avtech for the trigger pulse should be set to *advance* in this case, and Δ should be made larger than 2.1 μs . Data acquisition with a 1.5 keV Ne^+ beam, on the other hand, would be unaffected because $\Delta = 2.34 \mu\text{s}$.

Ions and neutral particles reaching the channel electron multiplier cause charge bursts that are coupled into a preamplifier (EG & G ORTEC VT120 fast preamp) via a 470-pF/6-kV capacitor separating the high voltage applied to the detector from the preamplifier. The 200-fold output of the VT120 serves as input to a discriminator that is part of the MCS. It is currently set to -0.06 V, the absolute value of which is high enough to screen out electronic noise and low enough to ensure that all true events are accounted for. The MCS is set to record the count rates for a predetermined period of time, generally 20–30 μ s, which is referred to as one pass. At the end of one pass, the MCS itself supplies the stop signal and waits for another start from the pulse generator. This is repeated for the number of passes, usually $3\text{--}5 \times 10^6$, while the recorded count rates are summed. The result is the desired time-of-flight spectrum.

2.2.10. Miscellaneous

2.2.10.1. Beam Position Monitors

A feature that adds particular convenience to the TOF spectrometer is a set of beam position monitors. They enable both finding the beam when it is badly mistuned and optimizing voltages on focusing lenses and deflector plates in order to maximize the current density at the position of the sample. The beam position monitors were constructed following the design given by Snowdon and Barber [76]. The first one is located down-beam from the Wien filter, ~ 10 mm in front of aperture f_1 . The second one, shown in Fig. 2.8, was placed at the end of collimation region one immediately in front of the aperture used for pulsing the ion beam. In both cases, the diameter of the central opening in the monitors is slightly larger than the following aperture. The ion current to each individual quadrant (Y+, Y-, X+, and X-) can be measured. The readings of two quadrants opposing each other can be selected via a switch box and are simultaneously displayed on two current measuring devices for visual comparison. This facilitates great ease for fine-tuning the ion beam.

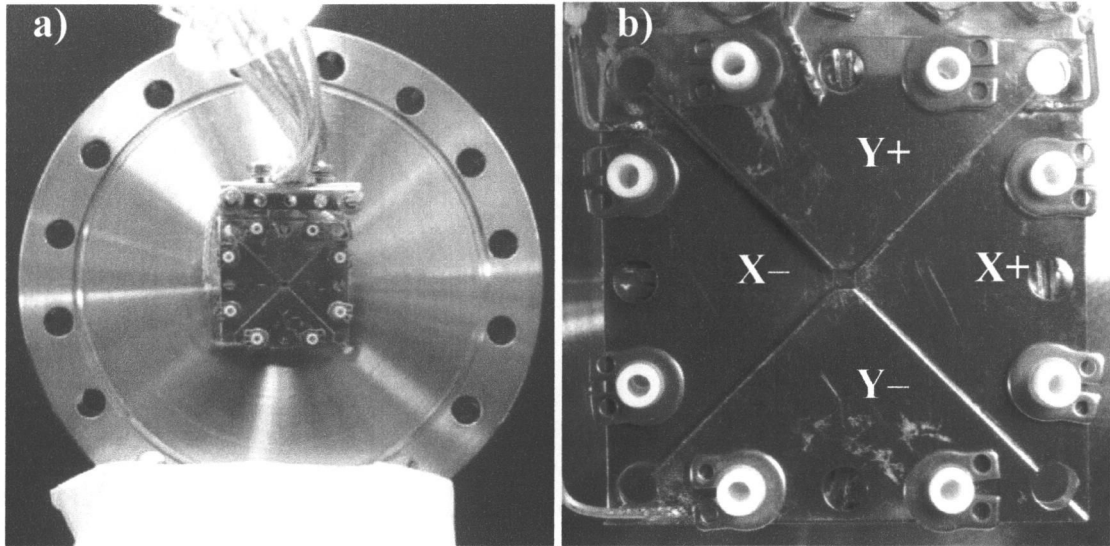


Fig. 2.8 Photograph of a beam-position monitor (BPM).
 a) BPM mounted to 6-inch Conflat flange. b) Close-up of BPM. This particular one is located down-beam from the first collimation region immediately in front of the aperture used for pulsing the ion beam. The ion's direction of travel is into the page. Kimball Physics eV Parts™ were used.

2.2.10.2. Diffusion Pump Protection Circuitry

A unique control unit powering the diffusion pumps (DPs) was included in the design of the TOF spectrometer's vacuum system. It serves multiple purposes. The power to all DPs is interrupted when the temperature of the cooling water gets too hot or the flow rate drops below a certain minimum. Fig. 2.9 shows the location of these sensor-driven switches in the circuitry controlling the flow of power to the pumps. Furthermore, details of the control unit protecting the DPs against overpressure conditions are given in Fig. 2.10. Thermocouple gauges monitoring the backing pressure of each individual DP are connected to Varian senTorr pressure gauge controllers. Analog voltages (0–10 V) proportional to the pressures are taken from the latter and serve as input to the control unit depicted in Fig. 2.10. If the backing pressure increases due to a failing rotary pump, the power to the respective DP is interrupted and, at the same time, a solenoid valve is opened, allowing cold water to quench the heating coil of the DP for a rapid cool-down. Exposure of the hot pump oil

to atmospheric oxygen as a result of a power outage or other equipment failure would, without this safety circuitry, result in substantial contamination of the vacuum system and damage to the diffusion pump.

The adjustable resistors (trimpots) in Fig. 2.10 enable fine-tuning of the upper and lower backing pressure limits for each DP at which the power to the DP is interrupted and restored, respectively. The hysteresis between the upper and lower limits can also be adjusted.

- Fig. 2.9 Schematic diagram showing the circuitry controlling the flow of power to the diffusion pumps.
OFF – power interrupt; TEMP – temperature sensing switch; FLOW – flow sensing switch; ON – set power switch; #'s 1,2,3 – switches for routing power through to diffusion pumps; RE – mechanical relay (SRE-202D); OV – override switch for solenoid valve; OD – override for diffusion pump power; PCL – pressure control light.
- Fig. 2.10 Schematic circuit diagram of the pressure sensing control unit.
TC/V – thermocouple gauge reading converted to analog input voltage; RE – mechanical relay (SRE-202D); R_f – resistor 10 M Ω ; R_b – resistor 1 M Ω ; T – transistor (2N2222A).

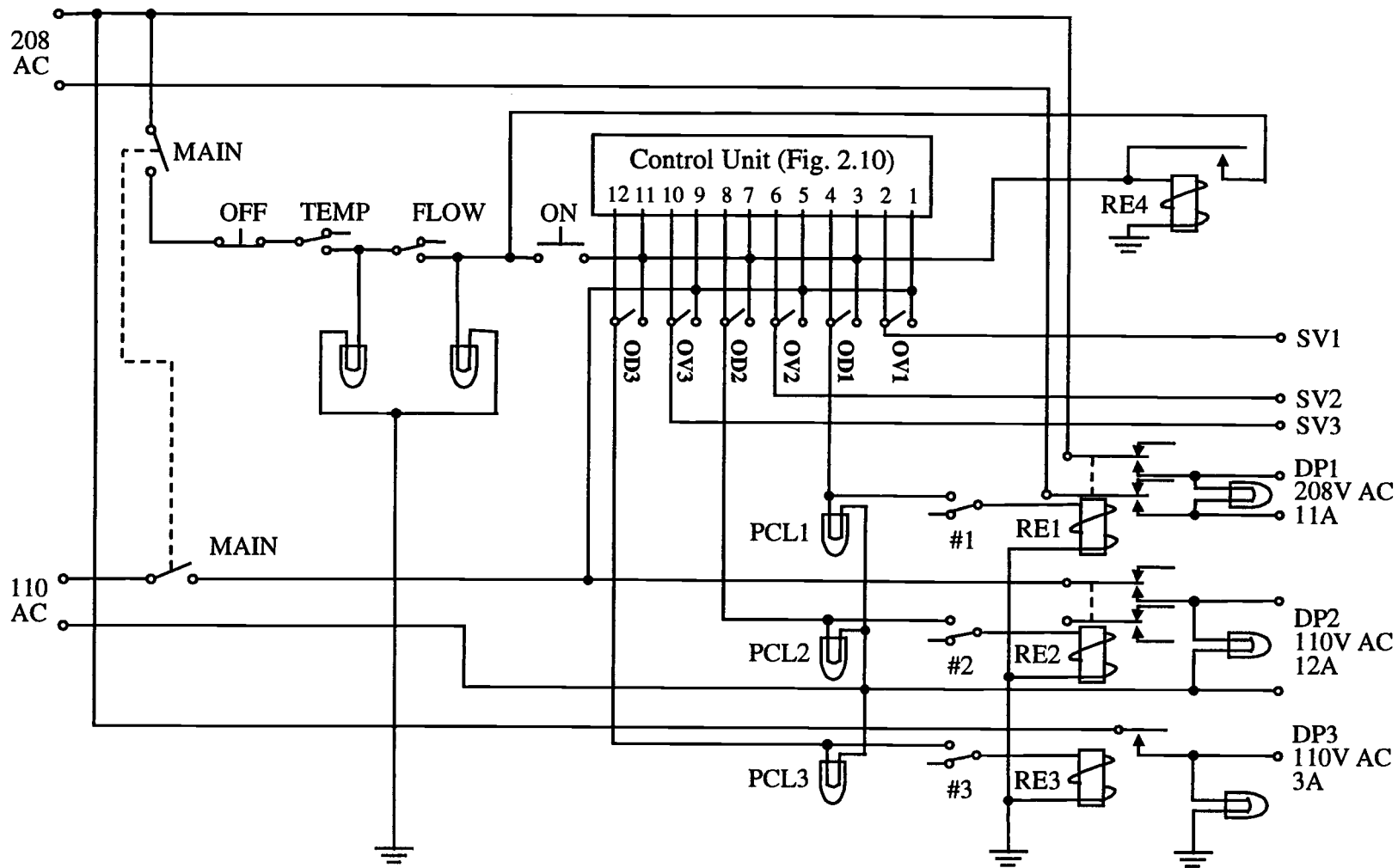


Fig. 2.9

2.3. Performance

The performance of the time-of-flight spectrometer is demonstrated in this section by exemplary TOF spectra obtained from liquid glycerol. Glycerol (99.5%, EM Scientific), $C_3H_8O_3$, is a relatively simple molecule with low enough a vapor pressure (9.6×10^{-5} Torr) that it represents an ideal first candidate for testing the spectrometer.

Fig. 2.11 demonstrates the influence of the inert gas projectile ion on the peak positions in a TOF spectrum. The graphs in the left column in Fig. 2.11, e.g. a, c, and e, display calculated flight times for various projectile ions as well as target atoms recoiled from the liquid surface as a function of the angle at which the detector is situated. The flight times were calculated for a 112-cm long drift region between the sample and the detector based on Eqs. (1.3) and (1.6) for scattered and recoiled particles, respectively. The TOF spectrum to the right of each calculated plot represents experimental data that was obtained under the exact same conditions.

A 2.5 keV He^+ ion beam is considered in Fig. 2.11a. The flight times of He^+ ions singly scattered by H, C, and O atoms are labeled He_{SS}/H , He_{SS}/C , and He_{SS}/O , respectively, while direct recoils are labeled H_{DR} , C_{DR} , and O_{DR} . As the scattering (θ) and recoiling (ϕ) angle are increased, e.g. the angle at which the detector is placed with respect to the initial direction of travel of the primary ions, both scattered He^+ ions and recoils from the surface take more time to traverse the distance to the detector. That is to be expected because the larger θ , the more kinetic energy is transferred to the collision partner, the maximum being found in backscattering where $\theta = 180^\circ$. Furthermore, in a near head-on collision, the recoiling target atom is ejected into a forward direction (small ϕ), which yields the fastest recoils. Notice, however, the loop that He_{SS}/H forms in Fig. 2.11a, e.g. the flight time is a double-valued function of θ . When the projectile is heavier than the target atom, both a large and a small impact parameter will lead to scattering into a particular angle θ [see Eq. (1.1)]. The former is much more likely and will result in fast scattered ions, while the latter causes low-energy ions. The maximum or critical scattering angle given by Eq. (1.2) can also be identified in Fig. 2.11a, being 14.47° for He_{SS}/H .

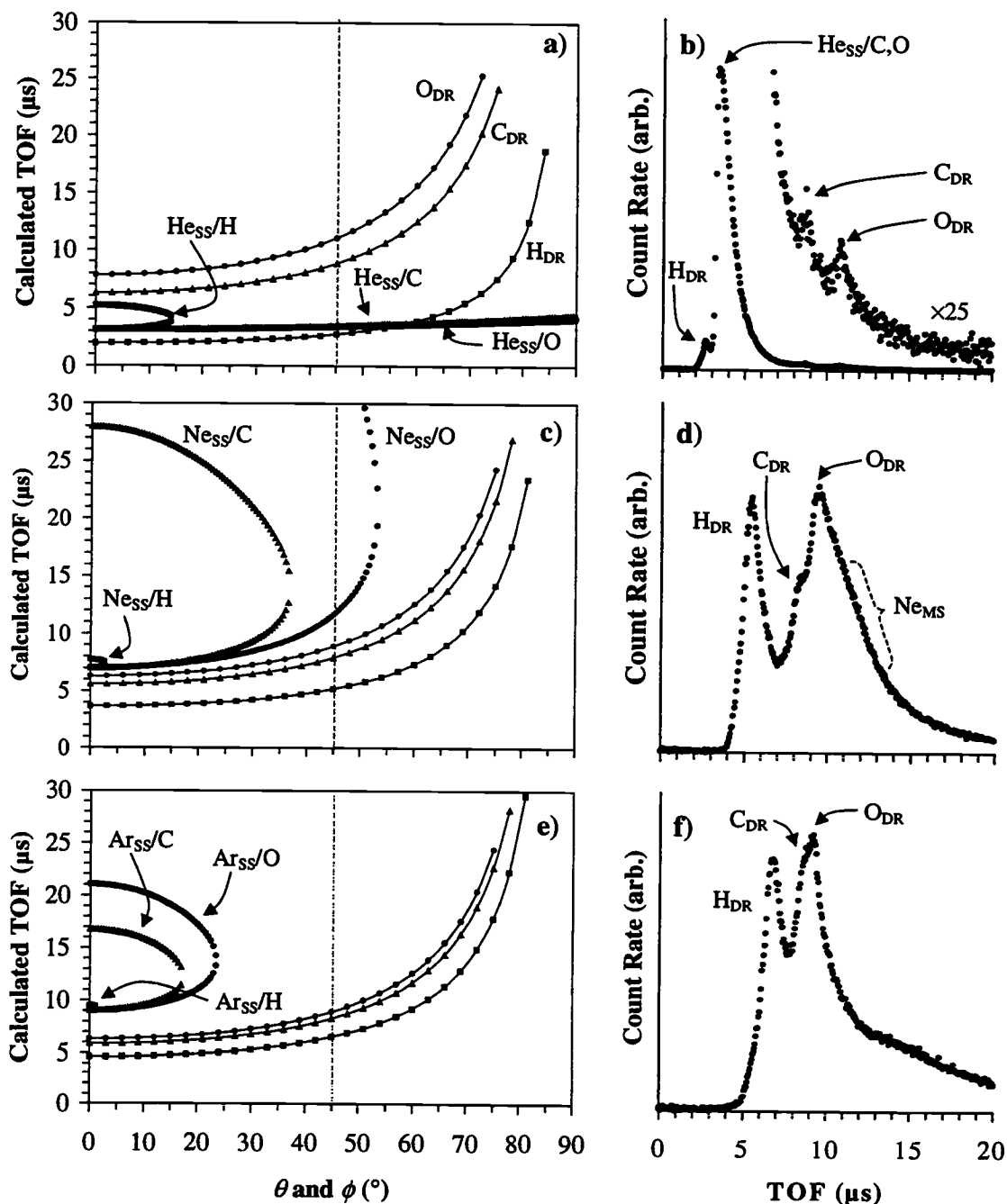


Fig. 2.11 Influence of the projectile ion type on the peak positions in a TOF spectrum.

a) Calculated flight times as a function of θ for 2.5 keV He⁺ ions scattering from H, C, and O atoms (denoted by He_{SS}/H etc.) and as a function of ϕ for H_{DR}, C_{DR}, and O_{DR} direct recoils. b) Experimental TOF spectrum for 2.5 keV He⁺ impinging upon glycerol, $\theta = \phi = 45^\circ$. c), d) same as a) and b) except for 2.5 keV Ne⁺. e), f) same as a) and b) except for 3.0 keV Ar⁺. See text for details.

The scattering and recoiling angles are fixed and equal in the TOF spectrometer described in this work, $\theta = \phi = 45^\circ$. This angle is indicated by the dotted line in Fig. 2.11a. By following this line from shorter to longer flight times, one is able to assess the peak separation obtained under the specific experimental conditions employed. For a 2.5 keV He^+ ion beam, a peak due to directly recoiled hydrogen, H_{DR} , is expected first, which is followed by two overlapping single-scattering peaks due to He^+ scattering from C and O. Two more spectral features are expected for C_{DR} and O_{DR} , well separated from the other peaks. The confirmation of the predicted flight times from Fig. 2.11a is demonstrated in Fig. 2.11b. Here, the most striking observation is the strong dominance in the count rate by the scattering signal.

Time-of-flight direct recoil spectrometry (TOF–DRS) is run under conditions that exclude the single-scattering features from the TOF spectrum, as shown in Figs. 2.11c–f. In Figs. 2.11c and d, 2.5 keV Ne^+ bombardment of the liquid surface of glycerol is considered, while Figs. 2.11e and f show the outcome for 3.0 keV Ar^+ . Interestingly, Fig. 2.11c suggests that three recoil peaks due to H_{DR} , C_{DR} , and O_{DR} are followed by a single-scattering peak due to Ne^+ scattering from oxygen. However, Fig. 2.11d does not show a distinct scattering feature at the predicted flight time, as did Fig. 2.11b for the analogous case of He^+ scattering. The reason for the apparent absence of the scattering peak is the experimental geometry. The angle $\theta = 45^\circ$ is close to $\theta_c = 53.1^\circ$, which is the critical scattering angle for $\text{Ne}_{\text{SS}}/\text{O}$, see Eq. (1.2). According to Fig. 1.4, the scattering cross-section is lowest right before θ_c , which minimizes the yield of singly scattered Ne^+ ions. Instead, a multiple-scattering background contributes to the spectral intensity right around the peak position predicted for single-scattering events. The region is indicated by Ne_{MS} in Fig. 2.11d.

The TOF spectrum in Fig. 2.11f, where 3.0 keV Ar^+ ions were used, is mostly free of any scattered Ar projectiles. The position and separation of the direct recoil peaks mirror the calculated values from Fig. 2.11e. Considering the change of the primary ion from He^+ to Ar^+ , a noteworthy observation can be made from Fig. 2.11. The heavier the projectile ion becomes, the more closely spaced the direct recoil peaks appear in the TOF spectrum. Peak overlap becomes more pronounced, which is one of

the adversaries of quantitative analysis. Thus, it is the combination of more than one single experimental parameter that has to be considered *prior* to actual data acquisition during the planning stage of an experiment. Unfortunately, this TOF spectrometer is currently limited to only one detector angle, 45° , which is the result of using a decommissioned vacuum chamber as the main sample cell housing. A freely adjustable detector position would greatly increase the versatility of the existing TOF spectrometer (at the price of higher costs, of course).

Finally, the effect of changing the angle of incidence of the primary ion beam with respect to the sample surface is demonstrated in Fig. 2.12 for 2.5 keV Ne^+ ions impinging on the glycerol surface. The change in the relative peak intensities can be exploited in order to determine the average orientation of molecules in the surface of a liquid [27,64,67,68]. The recoil yield as a function of the incident angle goes through a maximum and is considerably reduced for large α .

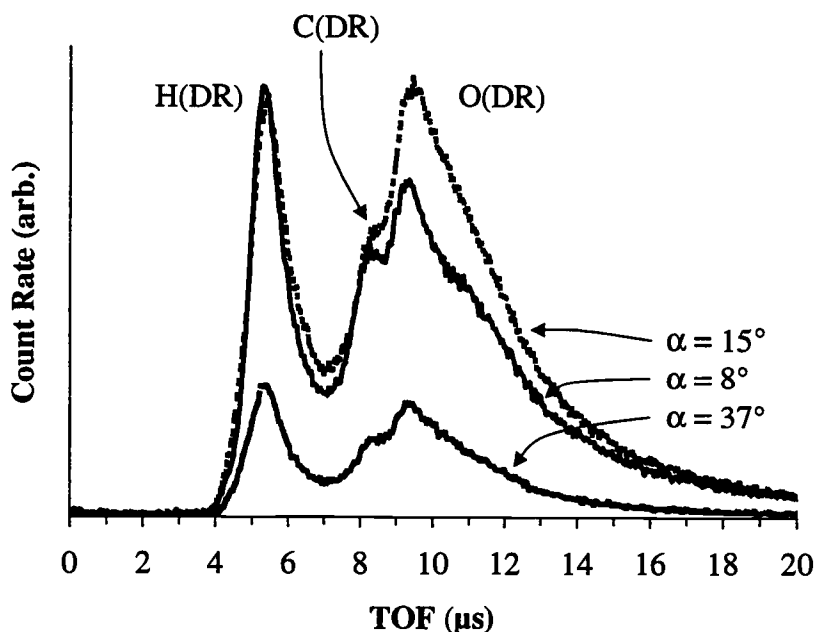


Fig. 2.12 Time-of-flight spectra from glycerol using 2.5 keV Ne^+ ions at $\phi = 45^\circ$. Note the change in relative peak intensities due to varying angles of incidence.

A more detailed discussion of the TOF spectra shown in this chapter is given in Ref. [27]. In this context, only the spectrometer's capability of generating an uncontaminated and representative surface of a low vapor pressure liquid (glycerol) was intended. Clearly, the TOF spectrometer built is capable of providing qualitative surface composition data.

The TOF spectra shown in Figs. 2.11 and 2.12 exhibit rather complex peak shapes that include tails to longer flight times. The extraction of quantitative numbers from such experimental data is a challenge, three major aspects of which will be discussed in the following chapters. While each peak in the TOF spectrum has an inherent width due to the vast variety of collision processes occurring in the liquid's surface, improvements of the spectral quality of the data are certainly possible. The most promising one in the author's opinion would be the use of a more powerful ion source with better beam definition, e.g. as narrow an energy spread as possible.

Chapter 3

Detection Efficiency of a Channel Electron Multiplier for Low Energy Incident Noble Gas Ions

Michael Tassotto and Philip R. Watson

Reprinted with permission from
Tassotto, M., Watson, P.R., "*Detection Efficiency of a Channel Electron Multiplier for Low Energy Incident Noble Gas Ions*",
Review of Scientific Instruments, **71**(7) (2000) 2704
© 2000, American Institute of Physics

3.1. Abstract

The absolute detection efficiency of a continuous channel electron multiplier (DeTech 407-EIC) has been measured for the noble gas ions He^+ , Ar^+ , and Xe^+ , with energies up to 4.9 keV. For all ions, the detection efficiency initially rises linearly as a function of velocity. Our results and a reanalysis of literature data show that the threshold velocity below which a multiplier does not respond to impinging ions cannot be regarded as independent of the ion's atomic number, Z , as previously reported. Instead, the threshold velocity is proportional to Z^c . The experimentally obtained efficiency-versus-velocity curves for our detector have been analyzed in the region of linear increase. The resulting expression for the detector efficiency, ε , is a function of the ion's atomic number and velocity, v , and can be written as $\varepsilon(v, Z) = a \left(v - b/Z^c \right) Z^n$, with a , b , c , and n being constants.

3.2. Introduction

Continuous channel electron multipliers (CCEMs) have been used extensively for the detection of electrons, and to a lesser extent photons, ions, and neutral particles. Due to their ability to register single events in the pulse-counting mode, CCEMs have become part of many surface science analytical instruments, such as mass spectrometers and electron spectrometers. Data obtained from surface sensitive tools such as these readily provide qualitative information on surface composition. However, quantitative analysis of surface properties is complicated by the need for knowledge of the detector efficiency. In instruments where only charged particles are detected, preacceleration to several kiloelectronvolts allows the investigator to assure uniform counting efficiencies (here, uniform does not necessarily mean 100 percent). In surface analytical techniques such as time-of-flight ion scattering and recoiling spectrometry [25,77] and one of its derived methods, direct recoiling spectrometry [31] (DRS), the ion fraction is minimal and primarily neutral particles reach the detector [31]. In these techniques both CCEMs and microchannel plates are used as detectors. In this article we will limit the discussion to CCEMs. Postionization of the neutrals by electron bombardment for possible preacceleration into the detector is not

feasible due to the low ionization cross-section for this process. The extraction of quantitative information on surface composition in DRS is based on the ability to relate measured peak intensities of different elements to each other. The measured peak intensity is directly proportional to the efficiency with which the CCEM registers an impinging particle. Without detailed knowledge of that response, quantitative analysis is rendered impossible.

A number of experimental studies have focused on the determination of the detection efficiency of channel electron multipliers for ions. They report multiplier gain factors [78], secondary electron yields [79], and relative [80] or absolute [81-87] counting efficiencies for ions as a function of particle velocity or energy. Schram et al. [78] showed experimentally that the multiplier gain factors for various ions satisfy a linear dependence on the ion's velocity independent of the charge state of the ions. This observation supports the assumed independence of the secondary electron yield on the charge of the exciting ion in Parilis and Kishinevskii's theoretical treatment [88] of ion-induced electron emission. Charge independence further implies that detection efficiencies for ions can also be applied to their neutral atoms, a necessary requirement for quantitative work in DRS. The equivalence of ions and neutrals as exciting projectiles for a CCEM has been confirmed experimentally by Chen et al. [89].

Dietz and Sheffield [79] showed that the ion-induced secondary emission coefficient of electrons, γ , from Al_2O_3 and BeO films is identical for isotopes of different masses with the same impact velocity. They also found that γ depends strongly on the electronic shell structure of the impinging ion. Hence, the atomic number, Z , not the ion's mass, is the important parameter in ion-electron emission. Another characteristic property and yet unresolved issue for CCEMs is their threshold behavior in secondary electron emission as a function of ion velocity. A CCEM does not register an impinging ion unless it enters with a velocity $v > v^{\text{th}}$ (threshold velocity). The literature reveals varying opinions about the Z dependence of this threshold velocity. The data of Burrous et al. [80] points to a different v^{th} for each type of ion. Both Schram et al. [78] and Dietz and Sheffield [79] forced extrapolated lines

from their data to pass through a common intercept on the velocity axis for $v^{\text{th}} = 5.5 \times 10^4$ m/s. However, the latter group admits that in the region of low ion velocities the actual secondary electron yield behavior is not well defined and suggests that additional work should be done to verify whether or not the velocity intercept is different for different ion-target combinations. Although Ravon's data [87] for rare gases show threshold velocities that vary less, they too depend on Z . Burrous et al. empirically found that the relative efficiency data for all the ions studied roughly followed the same trend when plotted as a function of the product of velocity and atomic number to the 0.4 power. Other authors have quoted this value, but the analysis ignores the Z dependence of the threshold velocity.

Comparing results from different sources in the literature can lead to some frustration. As Paschmann et al. [90] pointed out, experimental setups and techniques vary greatly from experiment to experiment. There can be gross differences in the intrinsic efficiencies of CCEMs depending on their geometry, manufacturing processes, and handling. Fricke et al. [82] clearly illustrated this important point in a compilation of data of absolute detection efficiencies of various channel electron multipliers for protons as a function of energy. The wide scatter of the data reflects the difficulties that experimenters face with particle detectors.

The present work was motivated by the aforementioned lack of consistency in the available data in the literature and the need to determine the absolute detection efficiency of a CCEM Model 407-EIC (Detector Technology, Inc.). This detector is used in our laboratory in a time-of-flight direct recoil spectrometer for counting atoms and ions recoiling from liquid surfaces after atomic collisions induced by an inert gas ion beam. The absolute detection efficiencies were determined for He^+ , Ar^+ , and Xe^+ ions ranging in energy from 0.15-1.7 keV for He^+ to 0.7- 4.9 keV for Xe^+ .

3.3. Experimental Method

The resistive layer of the CCEM under investigation is silica, while the bulk glass is lead-doped silica [91]. Mass-separated inert gas ion beams (Xe – MG Industries; Ar, He – Matheson; all scientific grade) were produced and focused in our time-of-flight direct recoil spectrometer. A detailed description of this apparatus is given elsewhere [27,74]. In order to obtain absolute detection efficiencies it is necessary to compare the CCEM's signal with absolute ion currents. To do this, a specially designed Faraday cup and the CCEM were mounted together on a precision manipulator. The schematic diagram of the experimental setup is shown in Fig. 3.1. A weldable grounded-shield, single-ended BNC (Bayonet Naval Connector) coaxial feedthrough was used as the Faraday cup holder for maximum shielding against electronic noise. The inside rear end of the Faraday cup had tightly spaced, concentric grooves in it, and the front end was beveled at a 45° angle with a 2.2 mm aperture to ensure against loss of ions and secondary electrons. The Faraday cup itself was fully

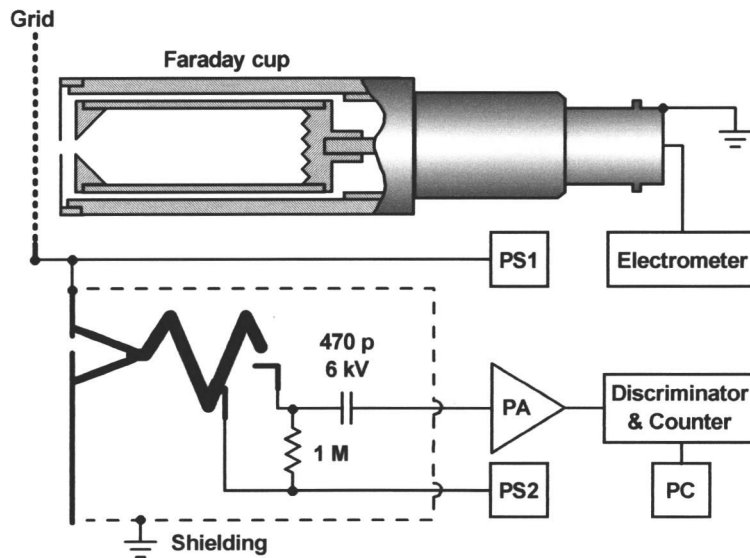


Fig. 3.1 Schematic diagram of the experimental setup. Components include: Keithley 614 Electrometer, PS1, PS2 – HV Power Supply, PA – EG&G ORTEC VT120 Fast Preamp, Discriminator & Counter – EG&G ORTEC Turbo MCS.

encapsulated by a grounded cylinder with a 2 mm front aperture. The horn of the CCEM was mounted to a metal plate with a 2mm aperture that was positioned off axis so incident ions would strike the inside of the cone. A grounded box surrounded the back end of the detector. The precision manipulator provided reproducible vertical displacement of the assembly setup so that the Faraday cup and the CCEM could be alternately exposed to the ion beam.

The measured count rates in the CCEM, and hence its absolute detection efficiency, can also depend upon the settings used in the detection electronics, particularly the discriminator (Fig. 3.1). Ideally, one would generate a beam current of N ions per second and adjust the discriminator and gain settings so that N events are registered by the counter. N has to be chosen small enough in order not to overload the CCEM ($< 10^6 \dots 10^8$ ions/s depending on the dynamic range of the detector). N also has to be large enough to fall within the reliable sensitivity range of the device used to measure the ion current entering the Faraday cup. In our case, the Keithley 614 Electrometer had a sensitivity of 10 fA but a reliable current measurement could only be taken to within 0.1 pA because of noise fluctuations. Thus, a reasonable lower limit for N would be 6×10^6 ions/s \cong 1 pA. In order to equate the ion current with the CCEM count rate, the ion beam energy has to be high enough to guarantee registration of all N ions with unity efficiency (plateau behavior of a CCEM). This last requirement could not be met with our experimental setup because the available ion beam energy is limited to ≤ 2.5 keV. Additionally, the energy at which the detection efficiency starts to saturate and reach unity is unknown until the experiment has been completed. Therefore, the discriminator setting was adjusted to the lowest level possible (-0.06 V) to give zero count rate when the ion beam was turned off, and the noise from other electronic devices was blocked from entering the preamplifier. We feel that this arrangement provides measurements that are good approximations to the true absolute efficiency.

A gold-coated metal grid (81% transmission) placed 3.5 mm in front of the Faraday cup served a dual purpose. First, a suppressor voltage of -30 V applied to it was used to test for loss of any secondary electrons from the Faraday cup. If such a

loss were occurring, the measured Faraday cup current (I_{FC}) would decrease when the suppressor voltage is applied. Biasing the grid in this way did not have any measurable effect on I_{FC} . The design proved to be very effective for trapping all incident ions as well as secondary electrons. Therefore, no suppressor voltage was applied to the grid during data acquisition. Second, increasing a positive retarding voltage (V_{RET}) applied to the grid up to the point where I_{FC} vanishes allowed us to test the energy profile of the ion beam. A typical I_{FC} - V_{RET} profile is shown in Fig. 3.2 for helium ions. The true ion beam energy used to determine the ion velocity for a set of measurements was obtained from the position of the maximum of the derivative in the I_{FC} - V_{RET} profile.

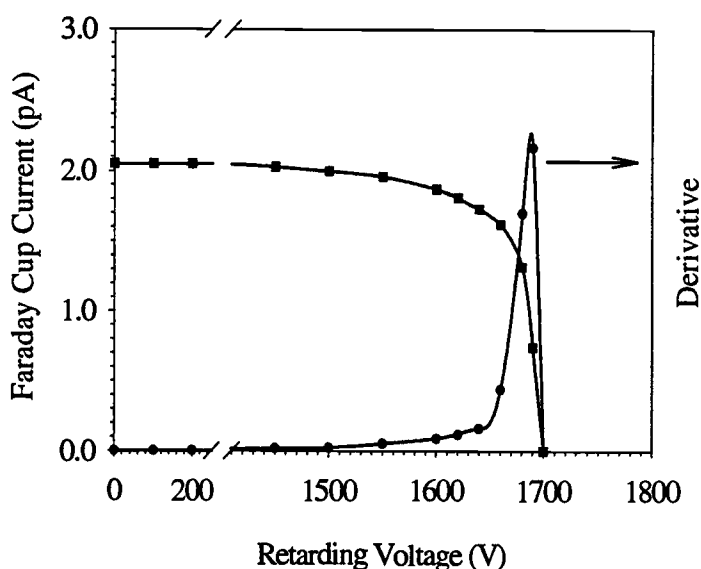


Fig. 3.2 Faraday cup current (I_{FC}) as function of retarding voltage (V_{RET}) for He^+ ions. The maximum of the derivative is found at $V_{RET} = 1690$ V.

The actual beam diameter at the position of the entrance apertures was measured to be approximately 1 mm. This was determined by simultaneously monitoring I_{FC} and the micrometer readings on the manipulator dials for horizontal and vertical motion.

Prolonged exposure of the CCEM to ion beams of high input current (~ 2 pA, 1.2×10^7 ions/s) caused an exponential loss of gain of one order of magnitude in about 40 min of continuous ion bombardment. Recovery of the CCEM gain took several

hours. This is a characteristic result of an increase in temperature at the output end of the detector. The resulting change in internal resistance of the CCEM is accompanied by a shift of voltage to the front end and a loss in gain as long as the temperature gradient exists [91]. Such a deterioration of performance was avoided by moving the CCEM into the beam, taking a measurement for 5 s, and removing it again. The potential difference across the CCEM was kept constant at 2.3 kV with the back end of the CCEM being more positive.

All measurements of the count rate as function of ion velocity were carried out with a single CCEM. Data acquisition for each type of ion was done according to the following procedure:

- (1) The $I_{FC}-V_{RET}$ profile was determined in the Faraday cup.
- (2) Positive retarding voltages were applied to the front end of the CCEM, and its response was measured for 5 s.
- (3) Step two was repeated for negative accelerating voltages in the case of Xe^+ .

3.4. Results

The number of counts measured in the CCEM was normalized to counts per second, N_{CCEM}^0 . Similarly, I_{FC} was converted to number of ions entering the Faraday cup per second, N_{FC}^0 (correcting for the transmission coefficient of the grid in front of the Faraday cup). The efficiency of the CCEM, ε , is then found from

$$\varepsilon = N_{CCEM}^0 / N_{FC}^0 \quad . \quad (3.1)$$

The variation of ε , as defined in Eq. (3.1), as a function of ion velocity for the three different inert gas ions is shown in Fig. 3.3. The relatively low absolute efficiencies might well be due to the fact that the detector has been in use for some time. The internal resistance of a CCEM can sometimes double in just a few months [91], thereby lowering the bias current. This would result in a reduced dynamic range of the multiplier and a loss of gain.

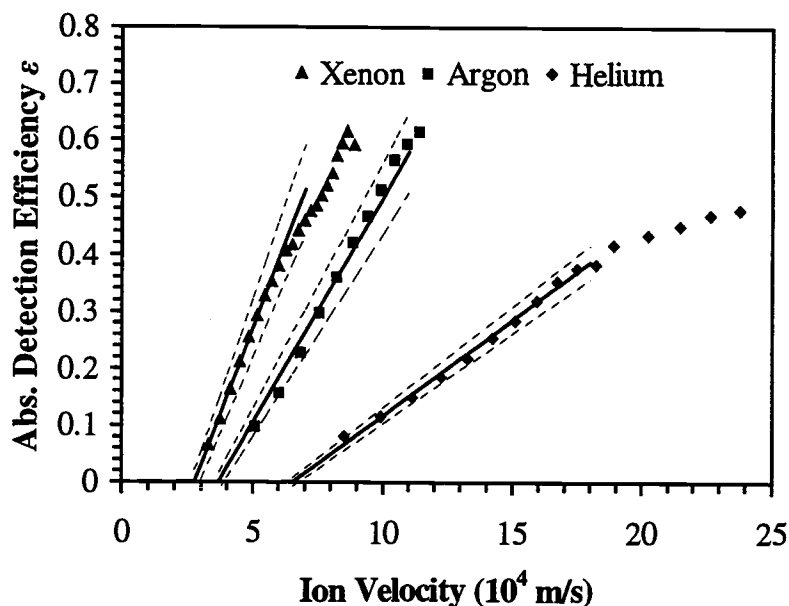


Fig. 3.3 Absolute detection efficiency for Xe^+ , Ar^+ and He^+ as function of ion velocity. Experimental data is shown as symbols. The threshold velocity is different for each type of ion. Solid and dashed lines represent solutions to Eq. (3.5) for $Z = 54, 18,$ and 2 and upper and lower limits, respectively.

The linear regions of the curves in Fig. 3.3 are of particular interest in DRS experiments with low energy incident noble gas ions. They represent the velocity ranges into which directly recoiled surface atoms can fall.

Table 3.1 List of energy and corresponding velocity ranges exhibiting linear increase of the detection efficiency for the noble gas ions He^+ , Ar^+ , and Xe^+ as seen in Fig. 3.3. All calculations in this chapter were carried out based on these subsets of experimental data.

Ion	Energy range (eV)	Velocity range ($\times 10^4$ m/s)
He^+	140 – 690	8.5 – 19
Ar^+	500 – 2500	5.1 – 11
Xe^+	680 – 2480	3.3 – 6.3

Table 3.1 lists the experimental velocity and energy ranges of linear response for the noble gas ions considered in this study. It is desirable to find a universal expression for ε in the region of linear increase that could be applied to every atom/ion entering the detector. In accord with previous researchers, we assume a dependence of ε on velocity, v , and atomic number, Z , in the functional form

$$\varepsilon_i(v, Z_i) = a (v - v_i^{\text{th}}) Z_i^n \quad (3.2)$$

Here, a and n are constants to be determined, v_i^{th} are threshold velocities, and i refers to the inert gas ion. The linear portion of each curve in Fig. 3.3 was extrapolated to $\varepsilon_i = 0$ in order to determine the v_i^{th} . The extrapolation as well as all subsequent calculations were carried out on the subsets of data listed in Table 3.1. Fig. 3.4 shows the Z dependence of v^{th} from our data, and the values of the v_i^{th} can be found in Table 3.2.

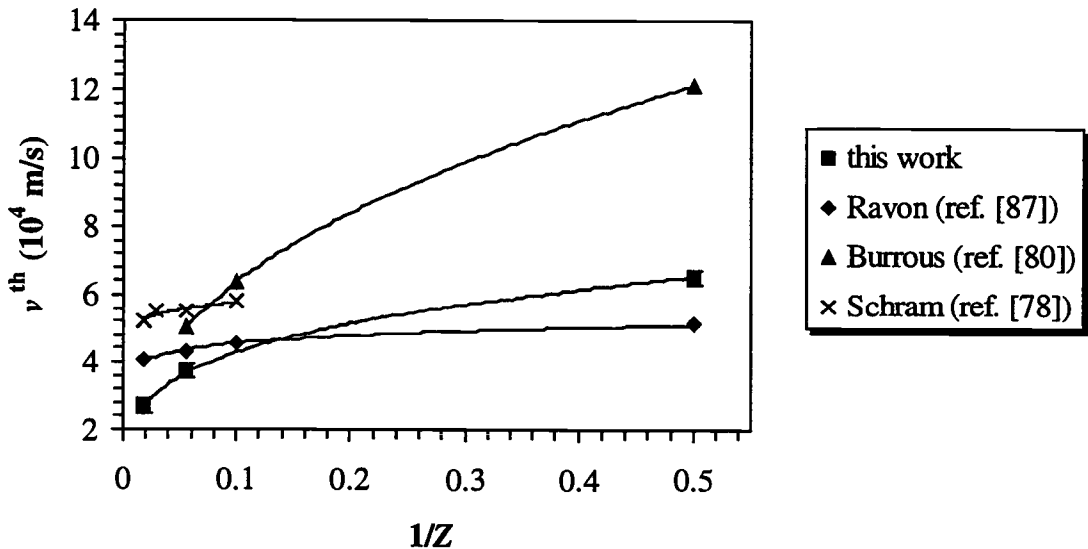


Fig. 3.4 Threshold velocity, v^{th} , as function of inverse atomic number. Results from this work are compared to data from the literature (see also Table 3.2). Error bars were estimated to be 0.2×10^4 m/s.

Table 3.2 Threshold velocities v^{th} from this work compared with literature values. The values were obtained by performing a linear fit to the experimental efficiency–ion velocity data points for each gas and extrapolating to zero efficiency.

Study	Threshold Velocity ($\times 10^4$ m/s)			
	He	Ne	Ar	Xe
This work	6.50	-	3.73	2.71
Ravon et al. [87]	5.14	4.53	4.31	4.18
Burrous et al. [80]	9.6	4.8	2.9	-
Schram et al. [78]	-	5.8 ^a	5.5 ^a	5.2 ^a

^a Found by extrapolation by Schram et al.

We find that v^{th} varies significantly with the identity of the ion and can express this variation in a power law of the form

$$v^{\text{th}}(Z) = b/Z^c \quad (3.3)$$

In Eq. (3.3), Z is the atomic number of the ion and b and c are constants. Here, the constant b can be interpreted as the threshold velocity for hydrogen ions.

Let us rewrite Eq. (3.2) to give

$$\log \left(\varepsilon_i / (v - v_i^{\text{th}}) \right) = n \log Z_i + \log a \quad (3.4)$$

Values for the left-hand side of Eq. (3.4) are obtained from Figs. 3.3 and 3.4 and plotted as function of $\log Z_i$ in Fig. 3.5. Linear regression yields constants a and n . If we now drop the index i from Eq. (3.2) and make use of Eq. (3.3), we can write a universal expression for ε as

$$\varepsilon(v, Z) = a \left(v - b/Z^c \right) Z^n \quad (3.5)$$

Constants b and c are determined similarly to a and n as described above. All constants are listed in Table 3.3 with their respective standard deviations. Solutions to Eq. (3.5) for $Z = 54, 18,$ and 2 are included as the solid lines in Fig. 3.3. The dashed lines in Fig. 3.3 represent upper and lower limits for $\varepsilon(v,Z)$ based on the propagation of error of the standard deviations.

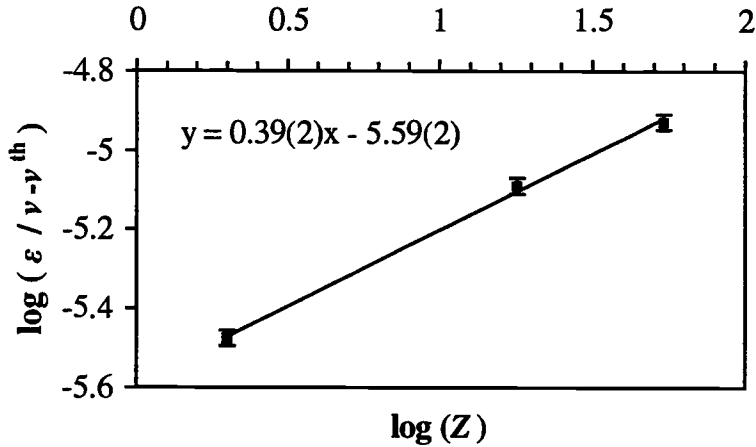


Fig. 3.5 Linear regression for the determination of constants a and n in Eq. (3.4). Error bars are based on those in Fig. 3.4 for the threshold velocity.

Table 3.3 Values of the constants $a, b, c,$ and n for $\varepsilon(v, Z) = a(v - b/Z^c)Z^n$. Literature values were derived as described in the text. For data from this work, standard deviations are given in parentheses.

Study	a ($\times 10^{-6}$ s/m)	b ($\times 10^4$ m/s)	c	n
This work	2.6(1)	7.8(2)	0.26(1)	0.39(2)
Ravon et al. [87]	3.6	5.8	0.07	0.55
Burrous et al. [80]	3.2	15.8	0.40	0.50
Schram et al. [78]	26 ^a	6.6	0.06	0.46

^a This value is not directly comparable to the others as it does not refer to absolute efficiencies (see text).

3.5. Discussion

The critical elements for discussion in the operation of a CCEM are the Z dependence of the threshold velocity, v^{th} , and the variation of the slope of the efficiency-velocity line with Z . We will address the threshold velocity issue first. Unfortunately, most researchers have not investigated the detector response in the low-velocity range and, furthermore, often extrapolate their data in such a way as to force an intersection on the velocity axis at one threshold value for all ions. The best available data in the literature is that of Schram et al. [78], Burrous et al. [80], and Ravon [87]. Schram et al. determined the threshold velocity for each ion by extrapolation and found values (see Table 3.2) that decreased with increased ion size. They did not regard their data as sufficiently accurate to permit an estimate of v^{th} for He. The variation in v^{th} was not large and, as the theory of Parilis and Kishinevskii [88] predicts that the threshold velocity should be independent of Z , Schram et al. chose to average their v^{th} values to 5.5×10^4 m/s. Burrous et al. did not explicitly extrapolate their efficiency-velocity data to find v^{th} . However, an inspection of their data shows that it is not possible for v^{th} to be a constant for different ions. Our extrapolation of their data in Table 3.2 reveals a relatively wide variation of threshold velocity values that follow the same pattern of decrease with increasing ion size. Ravon [87] also did not provide threshold velocity values, but once again our extrapolated values in Table 3.2 show a decreasing trend for v^{th} with increasing Z . This trend is more pronounced than that of Schram et al., but less so than Burrous et al. Our data are also shown in Table 3.2 and confirm this trend. They cover a range of threshold velocities that is somewhat larger than those of Ravon's.

The relationship of v^{th} to Z can be described quantitatively by fitting the values shown in Table 3.2 to an appropriate function. The type of function giving the best fit to the $v^{\text{th}}-Z$ data is one inversely proportional to the atomic number, as given in Eq. (3.3). A visual comparison of the fitted trendlines for data from both this work and the literature is given in Fig. 3.4. Explicit values for parameters b and c that relate to the threshold velocity in Eqs. (3.3) and (3.5) can be found in Table 3.3. The data of Schram et al. is difficult to evaluate as the low- Z point (He) is not available in Fig. 3.4.

In the case of the data from Burrous et al., the extrapolations are not very reliable as they provide very few data points (often only 2) that are usually for velocities much greater than threshold. The data in Ravon's article is only shown as lines without data points. Although the extrapolation is well defined here, its accuracy is not clear. Compared to our observations, the threshold velocity from Burrous et al. is a stronger function of $(1/Z)$, while that of Ravon's is much more similar. The sources of the difference to Burrous et al. may be rooted in the different types and ages of CCEMs used, but more likely originate in the long extrapolation from few data points available in analyzing Burrous' data. We feel much more confident in the curve derived from Ravon's data, and we believe that both his data and our own do not support the previously held view that the threshold velocity can be treated as a constant.

Having established the nature of the relationship of the threshold velocity with Z , we can now consider the dependence of the efficiency itself. Following the analysis procedure for our data as outlined in Section 3.4, we generated values for the left-hand side of Eq. (3.4) based on Ravon's and Burrous et al. data sets. Constants for parameters a and n in Eqs. (3.4) and (3.5) were obtained from plots similar to Fig. 3.5. This approach could not be used for the data of Schram et al., as they only measured gain values, γ , and did not measure absolute efficiencies. In this case we used the equation quoted by Schram et al.

$$\gamma_i(v, Z_i) = C_i (v - v_i^{\text{th}}), \quad (3.6)$$

from which we redefine via Eq. (3.4)

$$\log C_i = n \log Z_i + \log a'_i, \quad (3.7)$$

and v^{th} can be written as in Eq. (3.3). Then, a linear fit of Eq. (3.7) yields values for a' and n for Schram's data. Note that the scaling factor a' is not equivalent to the factor a used elsewhere because of the use of gain values and not absolute efficiencies by Schram et al. The resulting values for a , b , c and n for all the studies are shown in Table 3.3. The parameter a is a scaling constant that we expect to vary with the type of multiplier used and its age, yet the values of parameter a from the three studies using

absolute efficiencies are closely grouped. There is also close agreement in the values for the parameter b (effectively the threshold velocity for H ions) at $(7 \pm 1) \times 10^4$ m/s for the three studies where the extrapolations involved are most secure, i.e., excluding the very high value from the work of Burrous et al. The values of the c parameter that characterizes the Z dependence of the threshold velocity are more scattered, which may reflect true differences in multiplier response or the difficulties in reliably extrapolating high-velocity data. The variation in the values of the n parameter between the four studies is also not large, being between 0.39 and 0.55. The concordance of values for the parameters of Eq. (3.5) from studies performed with different detectors over a period of over 30 years is noteworthy. It gives us confidence that our assertion that the response of such detectors needs to include a Z dependence in the threshold velocity, despite theoretical predictions to the contrary, is valid.

Finally, the relation between the detection efficiency and the ion's atomic number and velocity was empirically derived for the region of linear increase of $\varepsilon(v,Z)$. Our assumed model clearly breaks down at higher energies where $\varepsilon(v,Z)$ begins to level off and saturate. At least two reasons can cause detection efficiencies less than 100% at lower velocities. First, below v^{th} , input events do not hit the detector surface hard enough to create any secondary electrons. Second, once v^{th} is surpassed, there exists the possibility that secondary electrons are scattered out of the cone and, thus, are unable to create an electron avalanche cascading down the multiplier channel. This depends on such factors as the detector design and the fields surrounding the opening of the cone [91]. Deviation from linearity and saturation of the detection efficiency is reached at higher ion velocities when every input event creates sufficiently many secondary electrons upon impact. Then, the probability of at least one secondary electron resulting in a charge burst at the collector output of the detector will approach unity.

Chapter 4

Simulation of Time-of-Flight Spectra in Direct Recoil Spectrometry for the Study of Recoil Depth Distributions and Multiple Scattering Contributions

Michael Tassotto and Philip R. Watson

Reprinted with permission from
Tassotto, M., Watson, P.R., "*Simulation of Time-of-Flight Spectra in Direct Recoil
Spectrometry for the Study of Recoil Depth Distributions and Multiple Scattering
Contributions*", *Surface Science* **464**(2-3) (2000) 251
© 2000, Elsevier Science, North-Holland, The Netherlands

4.1. Abstract

Intensity distributions of atoms ejected from model target surfaces due to ion impact in Time-of-Flight Direct Recoil Spectrometry (TOF–DRS) have been simulated in order to investigate the depth of origin of recoils and the shape of the low-energy TOF tail. The MARLOWE computer code was used to calculate the trajectories of 2–4 keV Ar⁺/Ne⁺ ions impinging on a diamond and an alkane polymer surface. The calculations were converted to actual TOF spectra, which allows comparison with experimental data. The simulation results confirm the high surface sensitivity of DRS and reveal the strong dependence of the sampling depth on the primary ion type and energy. A recoil's location in the TOF-intensity tail results from complex multiple-collision mechanisms and is not directly correlated to its depth of origin. In the case of H recoils, the Thomas–Fermi-type potential used to model atomic interactions appears to overestimate the differential recoiling cross-section, which may indicate a breakdown of fundamental assumptions in the interaction potential.

4.2. Introduction

The technique of Direct Recoil Spectrometry (DRS), first suggested by Chen et al. [30], has been used in the past for adsorbate surface structure determinations, investigations of chemisorption processes, and thin film growth and nucleation studies. For detailed applications see the reviews by Rabalais [31] and Hammond et al. [32]. More recently, DRS has also been applied to liquids to determine the average orientation of molecules at the surface [27,67,68]. In these studies, DRS has experimentally been proven to be very surface-sensitive. A pulsed ion beam is directed onto a target surface. The ions can both scatter from and eject target atoms due to atomic collisions. Spectral features due to the latter are the primary source of information in DRS, and collision geometries are chosen in such a way as to suppress the intense scattering peaks. In this article, all atoms ejected from the target surface due to ion beam impact will be referred to as *recoils*. Both qualitative and quantitative information on surface composition and structure can be obtained from time-of-flight

(TOF) spectra. Intensity distributions of recoils as a function of flight time are monitored while experimental parameters are varied. Those parameters typically include the polar and azimuthal angles of incidence of the primary ion, its type and initial energy, and the exit, or recoil, angle to the detector. In analyzing TOF-DRS spectra, it is common practice to obtain intensities by integrating the DR peak areas over narrow time windows. However, two problems arise immediately. First, the peaks frequently exhibit long tails to longer flight times, which often overlap with neighboring peaks. This fact greatly complicates the extraction of absolute numbers for quantitative analysis. Without accurate background removal, only trends in intensity-ratio variations can be considered. Secondly, even with accurate background removal, the depth distribution of recoils contributing to the DR peak intensity that is being integrated over has to be taken into account. This is important especially when atomic ratios for surface composition are to be determined.

The dependence of the sampling depth on primary ion type and energy has been investigated for time-of-flight ion scattering [92]. It was found that the sampling depth is determined by the size of shadowing and blocking cones which, in turn, depend on the type and energy of the projectile ion and the type of the target atom. In general, the more normal the direction of incidence of the primary ion beam with respect to the target surface, the deeper the sampling depth. While large-mass/low-energy projectiles probe the top atomic layer at shallow incidence, low-mass/high-energy projectiles at larger incident angles are favored in studying subsurface properties. Few simulation studies have attempted to extract information on the multiple scattering background in ion scattering spectroscopy [93,94]. To our knowledge, no such studies have been reported for DRS.

This article focuses on two aspects of DRS. First, the history of target atoms directly recoiling from collisions with low energy ions is investigated. This includes such recoil parameters as their original depth, number of post-displacement collisions suffered, recoil angles, and final kinetic energy (which is converted to an actual time-of-flight). Second, the actual shape of the background intensity due to multiple scattering of recoils is investigated. For these purposes, the MARLOWE [29] computer

code (version 14c) was used to calculate the trajectories of atoms recoiling from both a simple unreconstructed diamond model surface and a more complex surface of an alkane polymer. Recoiling target atoms were generated by collisions with 2 and 4 keV Ne^+ and Ar^+ primary ions. The trajectory calculations have been converted to actual TOF spectra. Here it is important to account for varying detection efficiencies [65] as well as broadening of the simulated DR peak due to the finite pulse width of the ion beam.

4.3. Simulation Model

In our laboratory, DRS is applied to samples that contain, among other elements, primarily hydrogen and carbon. The present simulation study focuses on crystalline targets with simple chemical makeup. The first target was to include carbon only, the second one both carbon and hydrogen. The benefits are ease of extraction of fundamental information and minimization of computing time. Fig. 4.1 displays the targets chosen. Carbon atoms arranged in the diamond lattice structure (unit cell edge length 3.57 Å) and the surface obtained by exposing the {001} crystal face are shown in Fig. 4.1a. Little is known about the surface structure of diamond. The {111} crystal face is believed to show unreconstructed, ideal bulk termination and is probably stabilized by hydrogen [95,96]. For the purposes of this study, the actual surface structure is not important, so the {001} face was chosen for convenience. Fig. 4.1b shows the model used to represent alkane polymer chains that are terminated by methyl groups at the top and truncated at the bottom. The structural parameters used are those for orthorhombic hexatriacontane (HTC) [97]. The crystal plane irradiated in the simulation is the methyl-terminated {001} face; i.e. the carbon backbones of all polymer chains are oriented vertically in the surface. Both the diamond and the polymer target were configured to extend laterally without boundaries.

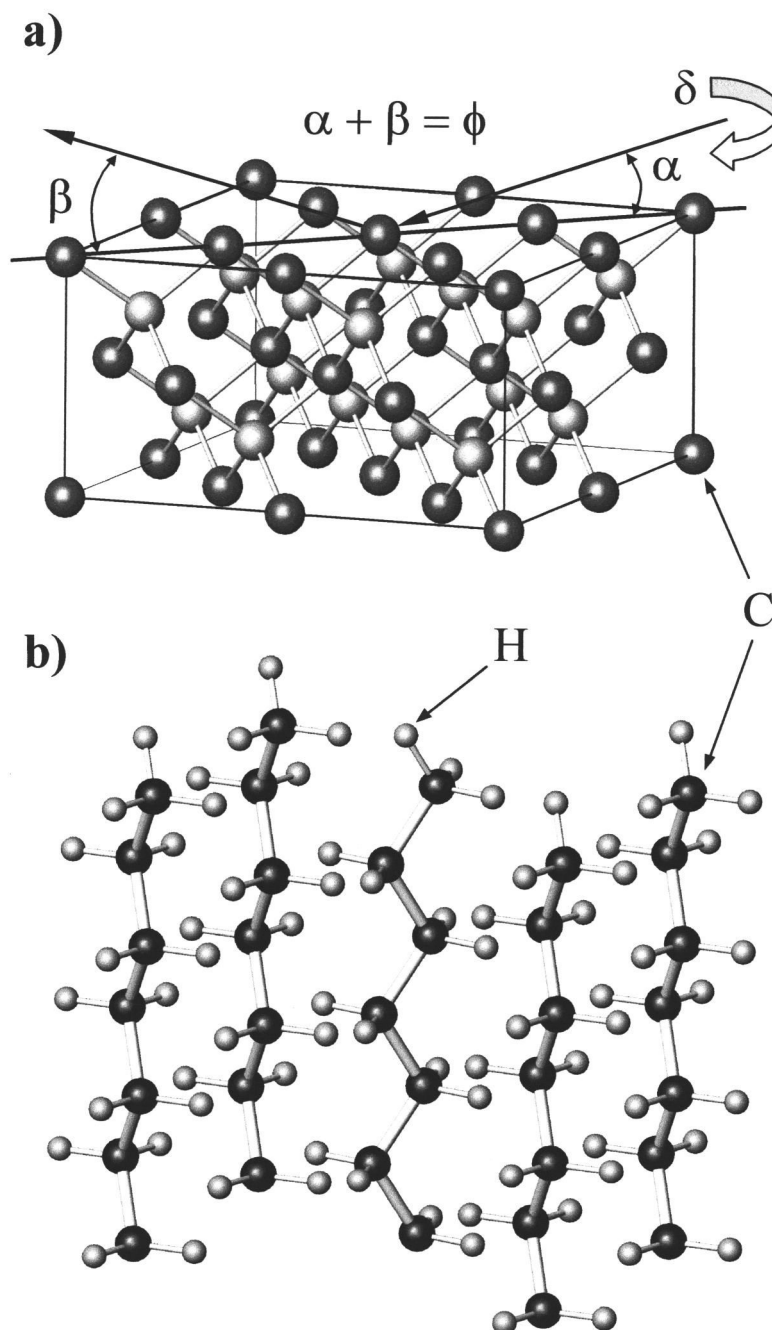


Fig. 4.1 Model surfaces chosen for DRS simulations.
 a) Carbon atoms arranged in the diamond lattice structure. The simulated external irradiation is incident at an angle α with respect to the surface and recoils are detected at an exit angle β , where $\alpha + \beta =$ recoil angle ϕ . The azimuth δ was chosen randomly. b) Vertically oriented alkane polymer chains that are terminated by methyl groups at the surface (top) and truncated at the bottom. Structural parameters were taken from [97]. In both Fig. 4.1a and b, the $\{001\}$ crystal face is exposed at the top.

The target depth of the former was infinite, while for the latter it was limited to 30 Å. This restriction was imposed in order to minimize the increase in computation time introduced by a more complex target. It had no effect on the results of the calculation whatsoever. The thickness chosen was more than sufficient. Both model surfaces are atomically smooth except for thermal vibrations (see below).

The impact points on the surface for 3×10^6 primary projectiles were uniformly distributed in an impact area corresponding to a surface unit cell ($3.57 \times 3.57 \text{ \AA}^2$ for diamond and $7.42 \times 4.96 \text{ \AA}^2$ for the polymer). In these simulations, the polar angle of incidence (α , defined in Fig. 4.1a) with respect to the surface plane was changed systematically. The azimuthal direction, δ , of beam incidence was not fixed to a particular value. Instead, the original MARLOWE code was edited to allow for randomization of δ . This was done in order to avoid the complications introduced by shadowing of incident projectiles or blocking of recoils [31]. The goal is to gain insight into the history of recoils and relate their properties to general peak shapes observed. Naturally, shadowing and/or blocking effects at certain azimuths as well as a particular choice of crystal face will influence the angular distribution of the recoil intensity. Fixing the azimuth at a particular angle may lead to results that are only specific to that angle and cannot be generalized. However, by randomizing the beam azimuth, dominant, unique effects introduced by a single scattering and recoiling geometry are greatly reduced if not eliminated. This strategy also allows the comparison of the simulation results on the alkane polymer with experimental data on azimuthally disordered solid hexatriacontane [98] and liquid heptadecane. Furthermore, the use of azimuthal randomization makes the transfer of our solid state results to liquid surfaces (our primary interest) more reasonable.

Screened Coulomb potentials, with screening functions based on the Thomas–Fermi statistical atomic model, have been extensively used to describe the physics of atomic collisions between charged particles and matter. The choice of the screening function depends on the conditions of the problem under consideration and on the accuracy required. The books by Torrens [38] and Mashkova and Molchanov [37] contain detailed discussions on interaction potentials. In this study, Molière's

approximation [49], which is computationally fast, was used with the Firsov screening length [50]. The influence of using other approximations to the Thomas–Fermi screening function was investigated for the “universal” (ZBL) potential [51] and the average modified Lenz–Jensen (AMLJ) potential [52,54]. The ZBL potential is a generalization of the Molière potential, which it includes as a special case. However, it is less efficient because its parameters are completely general [43]. The AMLJ potential may be the most accurate potential currently available for calculations involving the binary collision approximation. It includes corrections for electron exchange and correlation in the atoms. Comparison of identical calculations based on the aforementioned interaction potentials revealed that the overall recoil intensities were slightly affected. That is to be expected because the potential chosen to represent the interaction between collision partners directly influences the differential recoiling cross-section. More importantly, characteristic properties such as the depth distributions of recoils contributing to the simulated TOF spectra did not exhibit any significant changes with the underlying model potential. For these reasons, the Molière potential was employed throughout all calculations. Inelastic energy losses due to electronic excitations were treated in a low-energy approximation and were based on local [61] and non-local models [63].

The target atoms were allowed to undergo uncorrelated thermal vibrations with a surface temperature of 293 K. The vibrational amplitudes were based on mean square amplitudes for diatomic molecules [99] and were on the order of 0.1 Å or smaller. Certainly, this model is oversimplified. However, the outcome of the calculations was not significantly affected when amplitudes were chosen to be three times as large or even zero.

A particle detector was situated in the simulation at a recoil angle $\phi = 45^\circ$ with respect to the initial direction of travel of the primary ion. Final kinetic energies of recoils leaving the target into the proper direction were converted to actual flight times based on a path length of 112 cm. Those numbers correspond to our experimental setup, a description of which can be found elsewhere [27]. The simulated detector had an acceptance angle of 3° , which is five times more than the real detector. This

reduced calculation times by a factor of 25. Finally, the calculated TOF intensity distributions of recoils were adjusted in two ways. First, the raw TOF data were convoluted with a Gaussian (area) function to simulate the finite pulse width (170 ns) of the incident ion beam in the experiment. The peak broadening already introduced by the increased acceptance angle is of the same order of magnitude as the broadening caused by this convolution. Thus, the Gaussian convolution effectively acts as a smoothing procedure without further increase of the peak width. Secondly, because in MARLOWE all recoils are detected with unity efficiency, a function, $\varepsilon(v,Z)$, representing the detection efficiency of the real particle detector was applied to the calculated intensity distributions. This function is expressed as [65]

$$\varepsilon(v,Z) = a \left(v - b/Z^c \right) Z^n \quad (4.1)$$

Here, Z is the atomic number of the recoil impinging upon the detector, v its velocity, and a , b , c , and n are constants. For our detector, $a = (2.6 \pm 0.1) \times 10^{-6}$ s/m, $b = (7.8 \pm 0.2) \times 10^4$ m/s, $c = 0.26 \pm 0.01$, and $n = 0.39 \pm 0.02$.

The time resolution of all calculated TOF spectra, that is the time interval between points, was set to 250 ns, which helped improve the statistics of the simulations.

The calculations were performed on IBM workstations: RS/6000 Model 375 and Power PC Model 43P with a 604 processor, 512K level 2 cache, and 96 MB memory. The time necessary to complete one simulation ranged from 30 to 100 hours.

4.4. Results and Discussion

4.4.1. 2 keV Ar⁺ Bombardment of the Diamond {001} Surface

Fig. 4.2 shows calculated TOF spectra for carbon recoils as the result of bombarding the diamond {001} surface with 2 keV Ar⁺ ions. The incident angle α was varied from 12 to 30°. Outside this range, the obtained recoil yield was too low for useful statistics. The increments on each graph's ordinate are identical, so that direct comparison of peak intensities is possible.

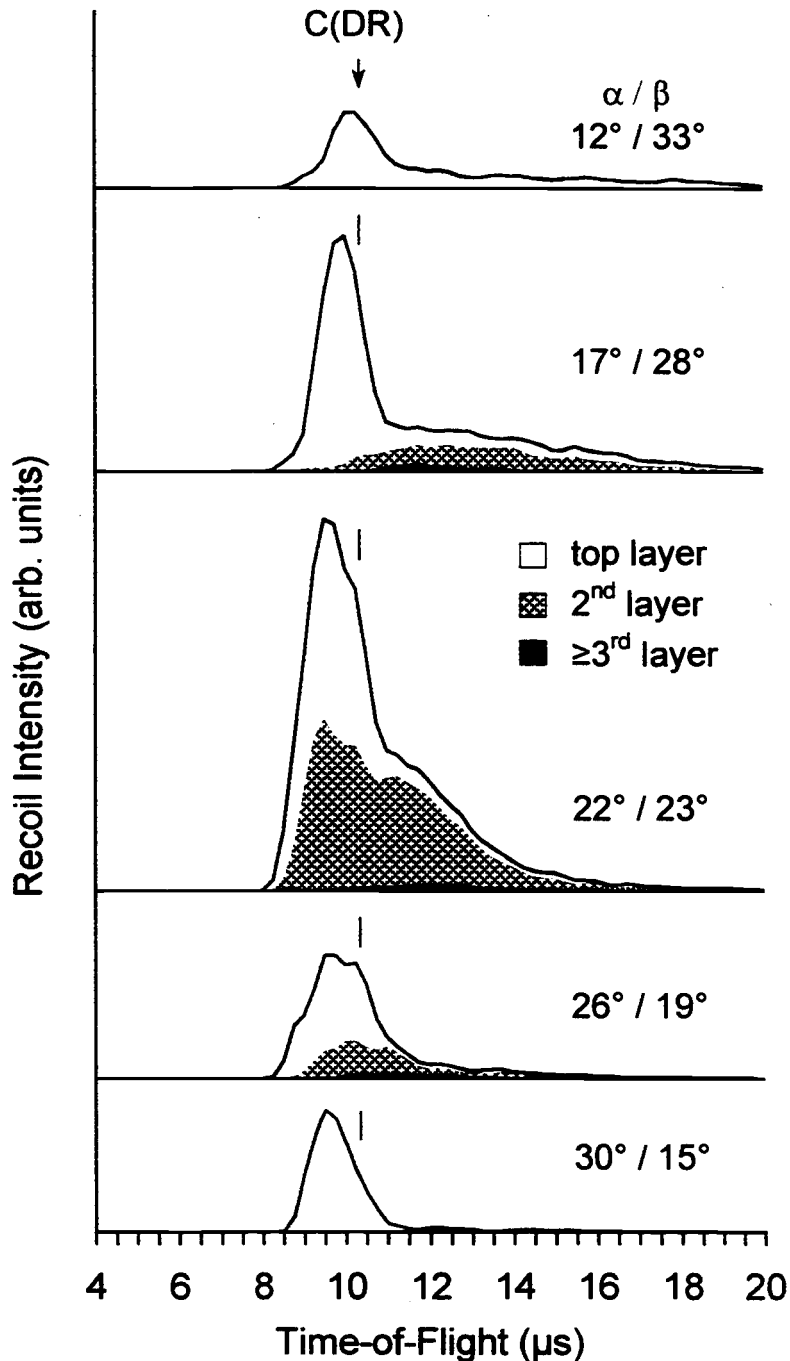


Fig. 4.2 Calculated TOF-DRS spectra for 2 keV Ar^+ bombardment of the diamond $\{001\}$ surface with overlaid area plots of depth distribution. Differently shaded portions of the peak indicate the layer of origin for the recoils. The angle of incidence, α , varies from 12 to 30°. The predicted TOF for directly recoiled carbon, C(DR), is marked by an arrow (10.1 μs). ($\phi = 45^\circ$, drift length 112 cm).

In each spectrum, the overall dark solid line constitutes the envelope of the calculated TOF spectrum. The areas under the peak, comprising overlaid area plots, are composed of differently shaded portions, each one representing a different depth of origin for the carbon recoils. Included are first, second, and third-or-deeper atomic layers (0, 0.89, and ≥ 1.79 Å, respectively). One can clearly see that the overall peak intensity increases as α increases. It reaches a maximum when the incident angle α and exit angle β are of equal magnitude ($\sim 22^\circ$). Further increase in α leads to a decline in intensity again. Almost all recoils exclusively originated in the uppermost two atomic layers. Only an insignificantly small contribution from lower lying layers can be seen for this recoiling geometry ($\alpha + \beta = \phi = 45^\circ$).

The energy, E_{DR} , of directly recoiled carbon atoms, C(DR), and their time-of-flight, t_{DR} , can be calculated from ion scattering kinematics based on the conservation of energy and linear momentum and are expressed [31] as

$$E_{\text{DR}} = E_{\text{p}} \left(4A / (1 + A)^2 \right) \cos^2 \phi, \quad (4.2)$$

$$t_{\text{DR}} = F (M_{\text{p}} + M_{\text{r}}), \quad (4.3)$$

with $A = M_{\text{r}} / M_{\text{p}}$ and $F = L / (\cos \phi (8M_{\text{p}}E_{\text{p}})^{1/2})$. M_{p} and M_{r} are the projectile and recoil atom mass, respectively, L measures the distance from the sample to the detector, ϕ is the recoil angle, and E_{p} is the projectile's initial kinetic energy. For the simulation conditions in Fig. 4.2, $F = 0.194$ $\mu\text{s}/\text{amu}$. The arrow in Fig. 4.2 marks t_{DR} as predicted for directly recoiled carbon atoms ($t_{\text{DR}} = 10.1$ μs , $E_{\text{DR}} = 710$ eV). At $\alpha = 12^\circ$, the recoil peak is fairly broad and centered close to t_{DR} . As α increases to 22° , the peak maximum starts to shift to shorter flight times, leaving a shoulder feature behind. Two overlapping peak components of approximately equal magnitude can be distinguished at $\alpha = 26^\circ$. Finally at $\alpha = 30^\circ$, the recoil peak has almost fully shifted to shorter flight times.

This shift in peak position can be understood by examining collision parameters of recoiled carbon atoms contributing to the peak maxima in Fig. 4.2. The history of

such recoils includes collisions that both precede and follow their displacement. Just prior to a displacement, the projectile ion may have suffered N_P deflections due to scattering from other target atoms, thereby changing its initial incident angle α to a local value, α_L . In this process, the projectile's kinetic energy was reduced from the initial value, E_P , to its current one, E_P' . The recoil itself, after having been displaced, leaves the collision site with energy E_R into a local recoil angle ϕ_L . It may undergo N_R more deflections before heading off into the detector. Fig. 4.3 defines both the local incident angle α_L and local recoil angle ϕ_L for the simplified case of in-plane scattering and recoiling. Whereas the angles α , β , and α_L are always measured in a plane normal to the surface, ϕ and ϕ_L have to be understood as three-dimensional recoil angles because MARLOWE calculates three-dimensional trajectories.

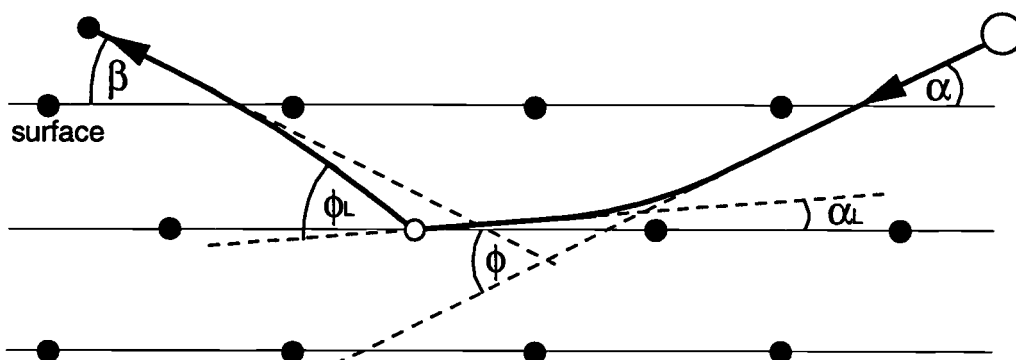


Fig. 4.3 Definition of the local incident angle α_L and local recoil angle ϕ_L . For the sake of simplicity, in-plane scattering and recoiling is considered.

During each of the 3×10^6 collision cascades per simulation, numerical values for the parameters N_P , α_L , E_P' , ϕ_L , E_R , and N_R of all recoils that struck the detector and of the projectiles that ejected them were written to an output file. This was accomplished by additional FORTRAN subroutines that were added to MARLOWE by the authors. Fig. 4.4 shows average values of these parameters calculated for first-layer recoils contributing to the main spectral features (peak, shoulder) in Fig. 4.2. This translates into a 0.5 and 0.9 μs wide time window for $\alpha = 12/17/30^\circ$ and $\alpha = 22/26^\circ$,

respectively. Recoils from subsurface atomic layers were not included in the averages because the gradual shift in the position of the peak maxima in Fig. 4.2 can almost entirely be attributed to first-layer recoils. The graphs in Fig. 4.4 display trends in the properties of these recoils that reflect two recoiling mechanisms which are known in the literature as *deflect recoiling* and *surface recoiling* [35]. The former is enhanced at low incident angle α and the latter at low exit angle β .

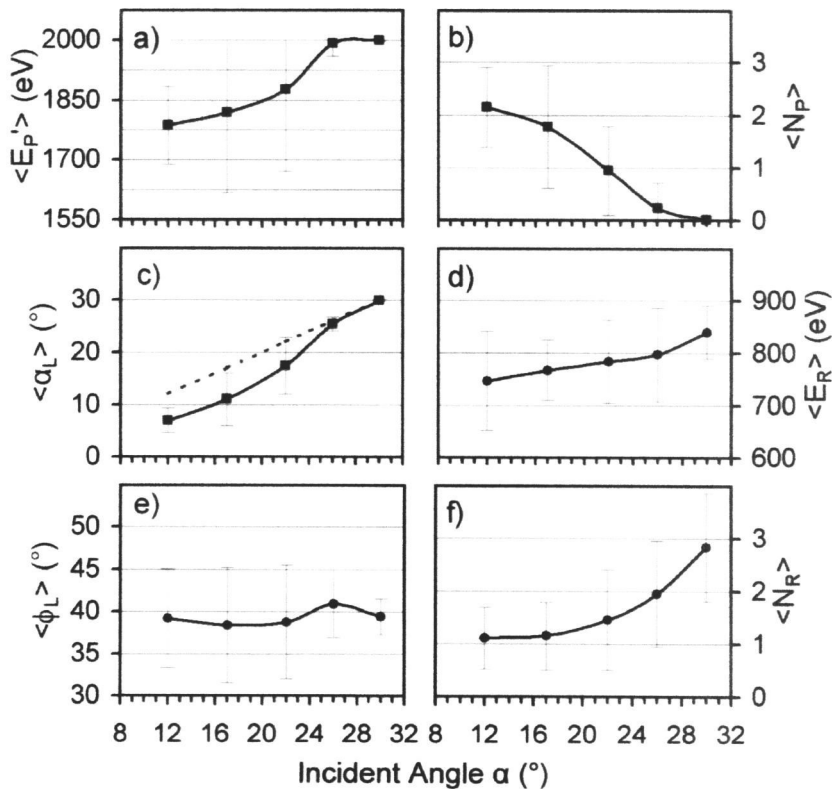


Fig. 4.4 Calculated average values of collision parameters between Ar projectiles and first-layer C atoms.

a) kinetic energy of projectile $\langle E_P' \rangle$, b) number of pre-collision deflections for projectile $\langle N_P \rangle$, c) local angle of incidence $\langle \alpha_L \rangle$, d) initial kinetic energy of recoil $\langle E_R \rangle$, e) local recoil angle $\langle \phi_L \rangle$, and f) number of post-displacement deflections for recoil $\langle N_R \rangle$. Averages were calculated over small time windows centered about the C(DR) peak in Fig. 4.2. See text for details. Error bars represent standard deviations. The dotted line in Fig. 4.4c indicates $\langle \alpha_L \rangle = \alpha$.

Considering the low- α data (12°) of Fig. 4.4, the Ar projectiles lost on average 200 eV ($\langle E_P \rangle \sim 1800$ eV) due to 2–3 deflections ($\langle N_P \rangle = 2.2$) prior to their collision with a carbon target atom (*deflect recoiling*). Their local incident angle was thereby reduced to $\langle \alpha_L \rangle \sim 7^\circ$ from the initial value of 12° (see deviation from dotted line in Fig. 4.4c). The newly displaced carbon recoil was ejected into a local recoil angle of $\langle \phi_L \rangle \sim 39^\circ$, with a kinetic energy $\langle E_R \rangle \sim 750$ eV. Due to the large exit angle β , these recoils suffer on average only one additional small-angle deflection ($\langle N_R \rangle = 1.1$) before heading to the detector. The relationships $\langle E_P \rangle < E_P$ and $\langle \phi_L \rangle < \phi$ introduce two competing effects in Eq. (4.3). The former causes an increase in t_{DR} , whereas the latter decreases t_{DR} . For $\alpha = 12^\circ$, both effects almost cancel completely so that the peak maximum is located very close to the position predicted for direct recoils (marked by an arrow in Fig. 4.2).

On the contrary, for large α (30°), on average the Ar projectiles suffered no loss of kinetic energy ($\langle E_P \rangle \sim 2000$ eV = E_P) and were not deflected ($\langle N_P \rangle = 0$) before being incident upon the target atoms. As a result, the average kinetic energy of the recoils ($\langle E_R \rangle \sim 840$ eV) is now about 100 eV higher than for $\alpha = 12^\circ$. The newly displaced recoils were also ejected into a local recoil angle of $\langle \phi_L \rangle \sim 39^\circ$. However, now because of the small exit angle β , these recoils suffer about three more additional small-angle deflections ($\langle N_R \rangle \sim 2.8$) due to scattering from atoms in the surface (*surface recoiling*).

Comparison of $\langle \phi_L \rangle$ and $\langle E_P \rangle$ for $\alpha = 12$ and 30° shows that while the local recoil angles are almost identical, the kinetic energies of the projectiles differ considerably. Thus, it is the high local projectile kinetic energy $\langle E_P \rangle$ that causes the surface recoil peak ($\alpha = 30^\circ$) to be located at shorter flight times compared to the deflect recoil peak ($\alpha = 12^\circ$). Applying the average values $\langle \phi_L \rangle$ and $\langle E_P \rangle$ from Fig. 4.4 to Eq. (4.3) leads to a difference in flight time of ~ 0.5 μ s, which reproduces the observed peak shift in Fig. 4.2.

The exit angle β has a significant effect on the spectral peak shape. For large β , a long tail of low-energy recoils follows the peak. The tail shortens as β decreases. This

change in peak shape is a direct result of the interaction between recoils and other target atoms in the surface. The lower the kinetic energy of a recoil, the higher its differential scattering cross-section becomes. Furthermore, the more grazing the exit angle, the more time this recoil spends close to the target surface. It is therefore more likely to be deflected from the trajectory that would deliver it into the detector. The influence of β on the spectral peak shape might be worth considering in choosing experimental geometries in DRS. However, the apparent advantage of a diminished recoil tail intensity seems to come at a price, as the overall count rate for recoils at low exit angles β is also reduced.

4.4.2. Influence of Projectile Type and Energy on Recoil Intensity and Peak Shape

Calculations similar to the ones shown in Fig. 4.2 were performed for 4 keV Ar⁺ and 2 keV Ne⁺ ions. Fig. 4.5 shows a comparison of TOF spectra calculated for $\alpha = 22^\circ$. This particular angle of incidence was chosen because of maximal recoil yield. The arrows indicate the flight times, t_{DR} , for directly recoiled target atoms. The change in projectile mass and energy causes peak shifts according to Eq. (4.3). The variation in overall peak intensity is due to changes in both the interaction cross-section between collision partners and the detection efficiency, ε . The latter strongly depends on the recoil's velocity. According to Eq. (4.1), the sensitivity ratio of the simulated detector for carbon recoils at t_{DR} is $\varepsilon_{4\text{keV Ar}} : \varepsilon_{2\text{keV Ne}} : \varepsilon_{2\text{keV Ar}} = 1.75 : 1.27 : 1$, which reflects the largely increased peak intensity in the 4 keV case study. The differential recoiling cross-section becomes smaller as the projectile's energy increases and its mass decreases. As evident from Fig. 4.5, ions faster or lighter than 2 keV Ar⁺ can more easily produce recoils that originate at greater depth. This confirms the findings of Bu et al. [92] for scattered ions mentioned in the introduction in Section 4.2. The increased sampling depth of low-mass/high-energy projectiles is a direct result of the reduced size of the shadow cone behind target atoms.

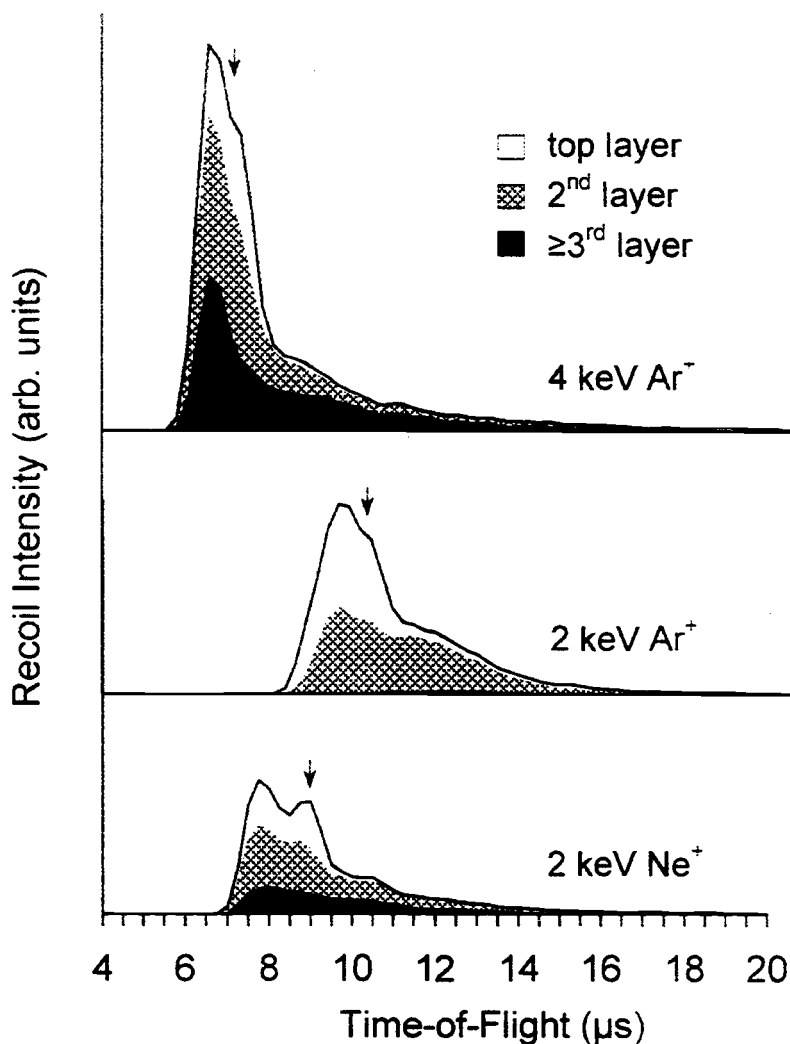


Fig. 4.5 Comparison of calculated TOF-DRS spectra for bombardment of the diamond {001} surface by projectiles of varying type and energy with overlaid area plots of depth distribution. Differently shaded portions of the peak represent the layer of origin for the recoils. The incident angle $\alpha = 22^\circ$ in all simulations. The predicted TOF for directly recoiled carbon is marked by an arrow. ($\phi = 45^\circ$, drift length 112 cm)

Two local maxima in the peak intensity of carbon recoils are clearly visible for the 2 keV Ne simulation in Fig. 4.5. The peak structure is primarily due to recoils coming from the topmost atomic layer. The second and deeper layers have a smoother structure. Examining the properties of first layer recoils contributing to the maximum

around t_{DR} ($\langle N_P \rangle = 0.2$, $\langle E_P \rangle = 1985\text{eV}$, $\langle \alpha_L \rangle = 21.3^\circ$, $\langle \phi_L \rangle = 43.2^\circ$, $\langle N_R \rangle = 1.5$), shows that they behave very much like true direct recoils ($\langle N_P \rangle = 0$, $\langle E_P \rangle = 2000\text{eV}$, $\langle \alpha_L \rangle = 22^\circ$, $\langle \phi_L \rangle = 45^\circ$, $\langle N_R \rangle = 0$). However, first layer recoils from the maximum at shorter flight time exhibit average values of the collision properties ($\langle N_P \rangle = 1.4$, $\langle E_P \rangle = 1893\text{eV}$, $\langle \alpha_L \rangle = 14.4^\circ$, $\langle \phi_L \rangle = 31.2^\circ$, $\langle N_R \rangle = 2.2$) that are indicative of surface recoiling. Note the difference in local recoil angles, 43.2° versus 31.2° . The smaller the recoil angle, the more kinetic energy is transferred from the projectile to the recoil in an elastic collision. A difference in flight time can be calculated from Eq. (4.3) for the average values above. The result of $\sim 1.1 \mu\text{s}$ reproduces the observed peak separation very well.

Projectiles reaching subsurface atomic layers have most likely been deflected multiple times before displacing a recoil which, in turn, is very likely to scatter from other target atoms along its path to the surface and on to the detector. Often these recoils are referred to as the multiple-scattering background contribution to the spectrum. Unfortunately, the spectral shape of that background contribution does not seem to be universal. Instead, it emerges as an integral part of the overall peak shape with a rather complex structure (see Fig. 4.5). It is safe to assume that not only the projectile's type and initial kinetic energy play a major role in the changing nature of this background structure, but that parameters such as target density and composition also play a part. Further systematic calculations are necessary to study the subsurface recoil contribution to spectral peak intensities in DRS.

4.4.3. *2 keV Ar⁺ Bombardment of the Alkane Polymer {001} Surface*

Fig. 4.6 shows calculated TOF spectra for the bombardment of the alkane polymer {001} surface with 2 keV Ar⁺ ions. The two peaks in the spectra are due to recoiling hydrogen and carbon target atoms. The incident angle α was varied from 3 to 30°. As in Fig. 4.2, the increments on each graph's ordinate are identical, so that direct comparison of peak intensities is possible. Again, recoils with varying depths of origin are indicated by differently shaded contributions to the overall peak areas.

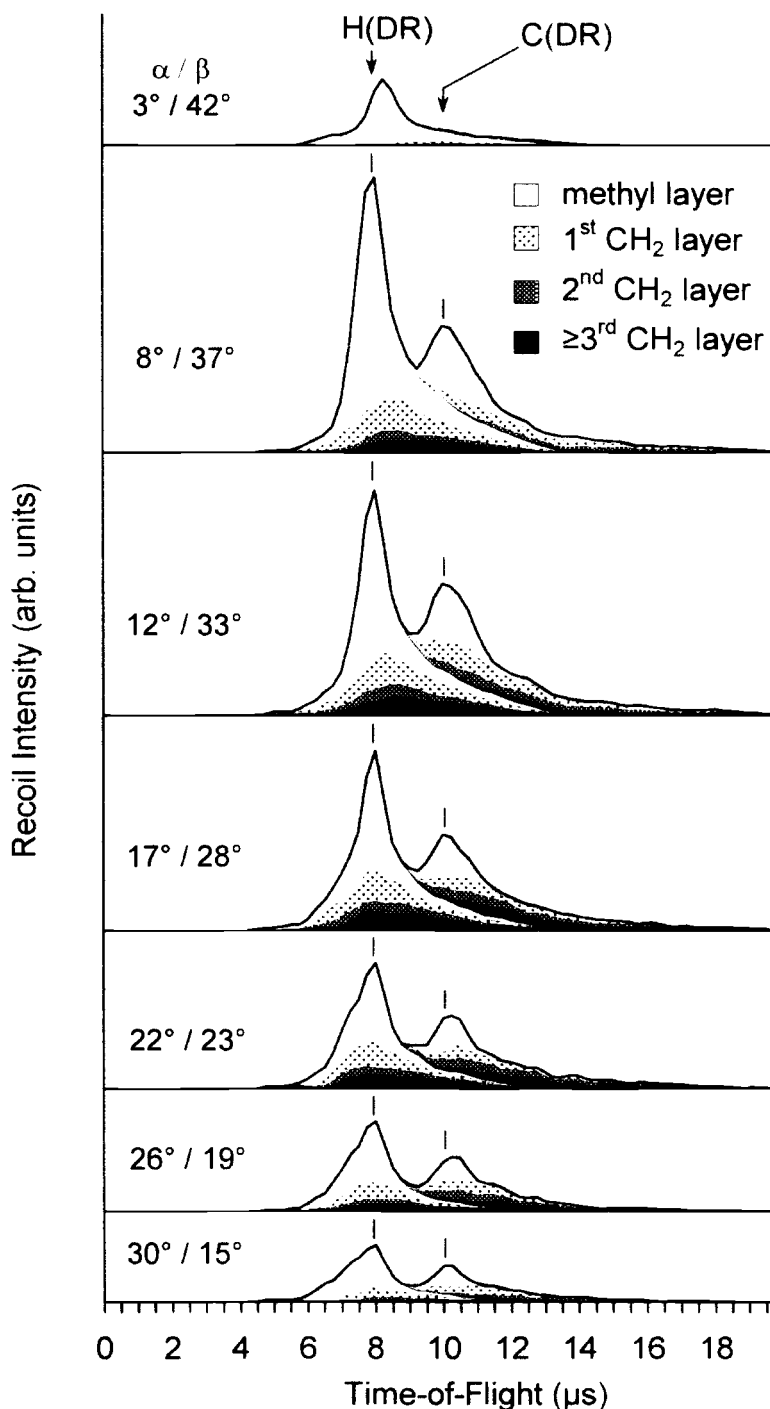


Fig. 4.6 Calculated TOF-DRS spectra for 2 keV Ar^+ bombardment of the alkane polymer {001} surface with overlaid area plots of depth distribution. Differently shaded portions of the peak indicate the layer of origin for the recoils. The angle of incidence, α , varies from 3 to 30° . The predicted TOF for directly recoiled hydrogen atoms, H(DR), and carbon atoms, C(DR), are marked by arrows ($7.97 \mu\text{s}$ and $10.1 \mu\text{s}$). ($\phi = 45^\circ$, drift length 112 cm).

The different shades distinguish between hydrogen and carbon recoils coming from the methyl group that terminates the surface and the adjacent, lower lying first, second, and third-or-deeper CH₂ groups.

Unlike the diamond surface where the overall recoil yield peaked around specular angles of incidence ($\alpha \cong \beta$), the polymer surface exhibits a shift of the maximum recoil yield to smaller α (~ 8 and $\sim 12^\circ$ for hydrogen and carbon, respectively). This is due to the change in chemical makeup and interatomic distances in the polymer target. The density of diamond is $3.51 \text{ g}\cdot\text{cm}^{-3}$. Every carbon atom is tetrahedrally bonded to its nearest neighbors with a covalent bond length of $\sqrt{3} a/4 = 1.55 \text{ \AA}$. In the {001} surface plane, the nearest neighbor separation is $3.57/\sqrt{2} = 2.52 \text{ \AA}$. The density of the polymer is much smaller, only $0.961 \text{ g}\cdot\text{cm}^{-3}$ for HTC. The *intramolecular* C–C bond length of 1.533 \AA is very close to the covalent bond length in diamond. However, the nearest *intermolecular* C–C distance is on the order of $(4.96^2 + 7.42^2)^{1/2}/2 = 4.46 \text{ \AA}$, giving the polymer a much more open structure compared to diamond. Furthermore, the hydrogen-rich polymer surface is readily penetrated by impinging Ar projectiles as is evident from the depth distribution of recoils in Fig. 4.6. The critical or maximum scattering angle, θ_c , into which an incident projectile of mass M_p can be deflected due to a single collision with a lighter target atom of mass M_T ($M_T \leq M_p$) is [31]

$$\theta_c = \sin^{-1} (M_T / M_p). \quad (4.4)$$

Eq. (4.4) yields 1.45 and 17.5° for argon colliding with hydrogen and carbon, respectively. This means that the diamond surface reflects an incoming ion beam much more effectively at shallow incident angles than does the polymer surface.

The predicted times-of-flight for H(DR) and C(DR), based on Eq. (4.3) and indicated by arrows in Fig. 4.6, match the recoil peak maxima well for almost all α . The only exception is the $\alpha = 3^\circ$ hydrogen recoil peak which is shifted to longer flight times. The consistency in peak position, which stands in contrast to the noticeable peak shift observed for carbon atoms recoiling from diamond (see Fig. 4.2), can be

explained by a close examination of the recoils' collision history. Fig. 4.7 shows a compilation of calculated average values of collision parameters for carbon recoils similar to Fig. 4.4. Averages were calculated over 0.5 μs wide time windows centered about the C(DR) peak in Fig. 4.6. Only carbon recoils from the methyl group terminating the surface were included in calculating the averages, because the lower lying CH_2 groups contribute primarily to a broad intensity distribution underlying the recoil peak maximum.

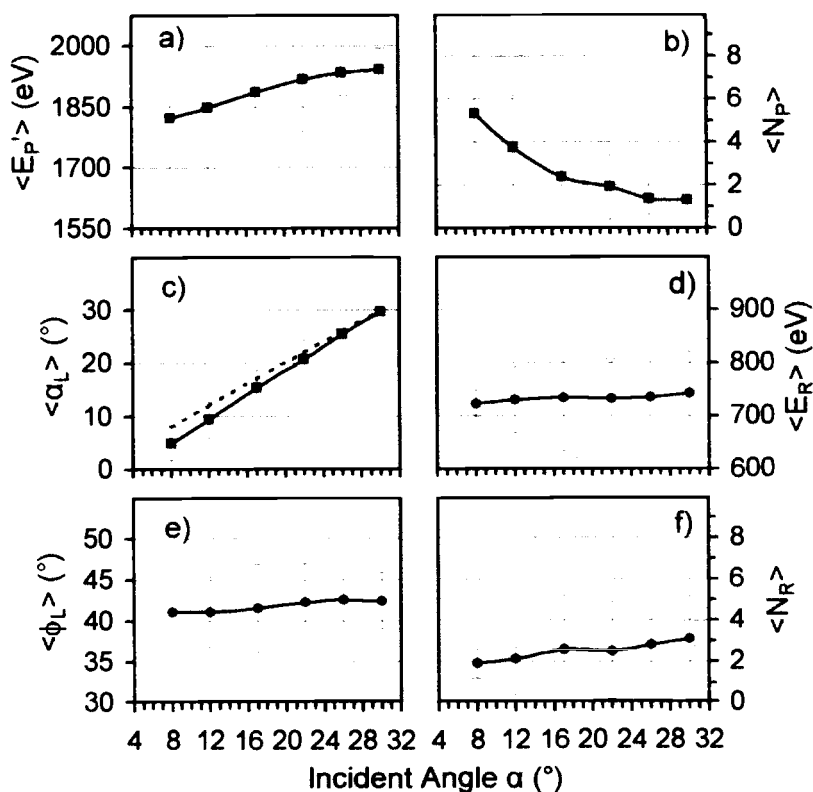


Fig. 4.7 Calculated average values of collision parameters between Ar projectiles and methyl-group C atoms. a) kinetic energy of projectile $\langle E_P' \rangle$, b) number of pre-collision deflections for projectile $\langle N_P \rangle$, c) local angle of incidence $\langle \alpha_L \rangle$, d) initial kinetic energy of recoil $\langle E_R \rangle$, e) local recoil angle $\langle \phi_L \rangle$, and f) number of post-displacement deflections for recoil $\langle N_R \rangle$. Averages were calculated over 0.5 μs wide time windows centered about the C(DR) peak in Fig. 4.6. See text for details. Error bars represent standard deviations. The dotted line in Fig. 4.7c indicates $\langle \alpha_L \rangle = \alpha$.

The exact C recoil peak position is chiefly influenced by what happens to the C atoms in the methyl group. Calculated averages for hydrogen recoils are not shown here, however, they exhibit the same trend behavior as the carbon recoils.

At any given incident angle α , the Ar projectiles are deflected about twice as often by target atoms before creating a carbon recoil when incident upon the polymer surface compared to the diamond surface (see Figs. 4.7b and 4.4b). However, in the polymer case, these interactions primarily happen with hydrogen atoms and, therefore, do not cause the projectile to deviate much from its original course. This is supported by Fig. 4.7c, where the average local incident angle $\langle\alpha_L\rangle$ follows α rather closely (dashed line $\langle\alpha_L\rangle = \alpha$). The consistency in recoil peak position can be attributed to the largely α -independent behavior of both the average kinetic energy of the recoils $\langle E_R\rangle$ and their local recoil angle $\langle\phi_L\rangle$, as seen in Figs. 4.7d and 4.7e, respectively. Notice that $\langle\phi_L\rangle$ in Fig. 4.7e is closer to $\phi = 45^\circ$ than in Fig. 4.4e, the diamond case study. This is directly related to both the structural openness and richness in hydrogen of the polymer in comparison to the dense diamond target.

The simulated ion beam pulse width of 170 ns, which was based on experimental parameters, contributes to broadening of the recoil peaks. While pulsed ion beam widths of much shorter duration would sharpen the individual spectral features, the recoil intensity between the H and C peak maxima would still not reach the baseline for our experimental geometry even at a low projectile energy, where the largest peak separation occurs. This is due to a tail of low energy recoils (refer to Fig. 4.6) that follows *every* recoil peak in DRS. The points along the time-of-flight axis at which these tails drop to zero depend on the sensitivity of the particle detector to slow recoils. Eq. (4.1) was experimentally determined by the authors [65] and used throughout this simulation study to describe the threshold behavior of a real particle detector. It yields, for example, a minimum velocity for the detection of hydrogen recoils of $78,000 \text{ m}\cdot\text{s}^{-1}$ which equals a kinetic energy of roughly 30 eV (14.3 μs flight time for 112 cm drift length). Hydrogen recoils of even lower energy are naturally being produced in collision cascades in the polymer target. However, when incident upon the detector they fall below the detection limit and are not registered.

The depth distributions of H and C recoils given by area plots in Fig. 4.6 reveal an interesting property of the TOF recoil intensity tail. Hydrogen and Carbon atoms not only from various CH₂ groups below the surface but also from the methyl group contribute to the recoil tail intensity. All depths from the topmost methyl group to maximum penetration are represented in the TOF tail. This demonstrates the absence of a straightforward correlation between the depth of origin of a recoil and its final kinetic energy and hence its location in the TOF tail. Instead, a variety of complex mechanisms of multiple collisions is responsible for this low-energy recoil intensity tail.

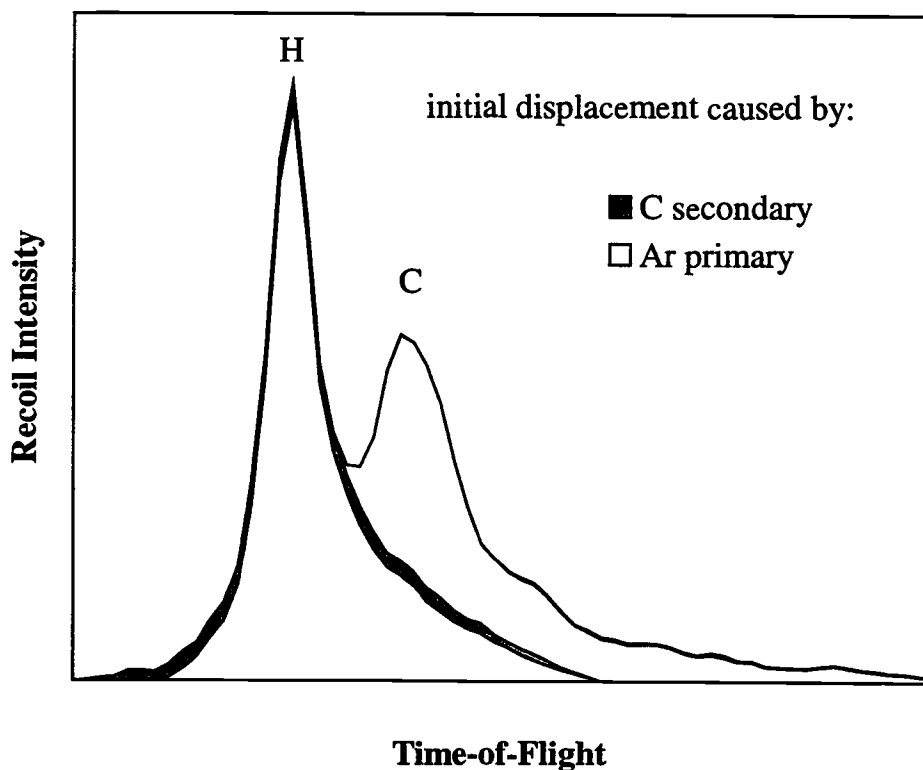


Fig. 4.8 Example of an area plot revealing the identity of the collision partner that caused the initial displacement of hydrogen and carbon recoils. (2 keV Ar⁺ ion beam, $\alpha = 12^\circ$).

When considering multiple collision mechanisms, it is important to examine what types of collision sequences most strongly contribute to the recoil tail intensity. In other words, are primary projectiles or secondary particles in the collision cascade responsible for the initial displacement of low energy recoils? An example of an area plot revealing the identity of the collision partner is shown in Fig. 4.8 for 2 keV Ar⁺ ions incident on the polymer target at an angle $\alpha = 12^\circ$. Area plots for other simulation geometries and energies are very similar to the example shown. Fig. 4.8 clearly demonstrates that virtually all carbon recoils and the vast majority of hydrogen recoils in the TOF tail result from collisions with primary Ar⁺ ions. The recoils' final kinetic energies are products of energy loss combinations due to multiple collisions suffered by the primary Ar⁺ ion and the displaced recoils themselves. Only a small fraction of the spectral intensity is due to hydrogen recoils that were initially displaced by secondary carbon atoms. Notice that the few, very fast hydrogen recoils are produced by secondary carbon atoms.

4.4.4. Comparison to Experimental Data

4.4.4.1. Liquid Heptadecane

Heptadecane (C₁₇H₃₆) belongs to a group of n-alkanes that have been reported to form an ordered surface layer in the liquid at a temperature, T_s , 2–3 °C above their bulk freezing points. See, for instance, Ref. [11] and references therein. On cooling, a phase change occurs at T_s , producing an ordered monolayer in which the molecules' carbon backbones are aligned parallel to the surface normal. The alkane polymer model chosen in this study closely resembles the arrangement of the molecules in the ordered surface monolayer of heptadecane. Only the intermolecular spacing needed to be adjusted with respect to the previously discussed calculations. Hexagonal packing for the monolayer of C₁₇H₃₆ molecules was assumed with a chain–chain separation of 4.77 Å [100].

A TOF–DRS spectrum of liquid heptadecane was recorded in our laboratory with a 2.5 keV Ar⁺ ion beam incident at $\alpha = 16^\circ$ ($\phi = 45^\circ$, drift length 112 cm). The

liquid's temperature was held constant at $23 \pm 1^\circ\text{C}$ (freezing point is 22°C). Fig. 4.9 compares the experimental spectrum to the simulation. Spectral intensities were normalized to the C(DR) peak maximum. While the simulation reproduces the separation of the H(DR) and C(DR) peaks quite well, the H(DR)/C(DR) peak intensity ratio is grossly overestimated. One possible source of error is the formula in Eq. (4.1) used to represent the detection efficiency. However, this formula was specifically determined for the type of detector used in our experimental setup, and one would not expect an error in relative detection efficiency for H and C direct recoils of this magnitude. In fact, a propagation of the error tolerances for parameters a , b , c , and n used in Eq. (4.1) leads to a possible change in the H(DR) peak height of only $\leq 16\%$ of

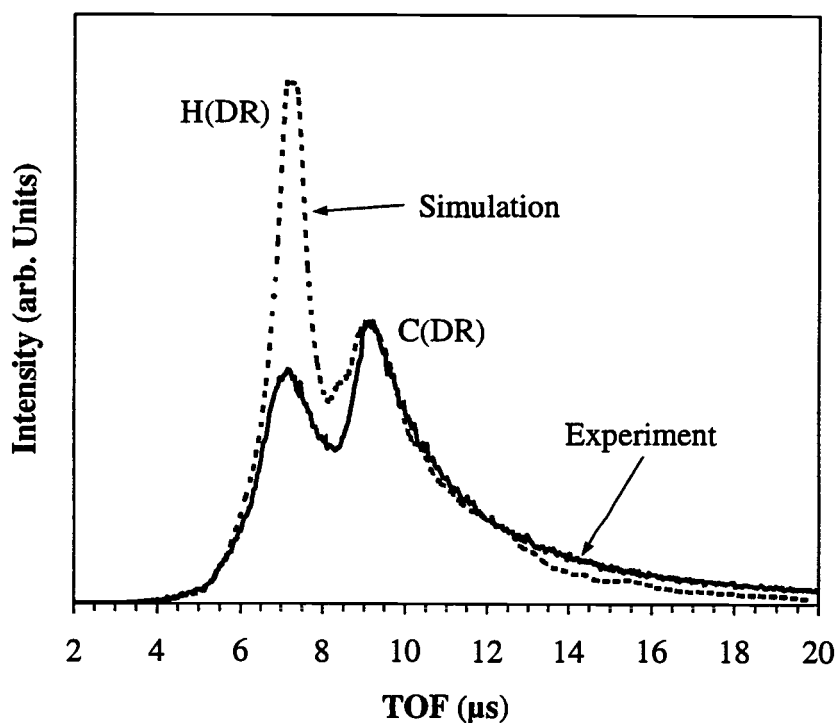


Fig. 4.9 Comparison of an experimental TOF-DRS spectrum for liquid heptadecane with simulation. Intensities were normalized to the C(DR) peak maximum. The significantly higher H/C ratio in the simulation appears to be rooted in an overestimated differential recoil cross-section for hydrogen. See text for details. (2.5 keV Ar^+ , $\alpha = 16^\circ$, $\phi = 45^\circ$, $T = 23^\circ\text{C}$, drift length 112 cm).

the peak maximum. This certainly does not account for the observed discrepancy in peak intensity ratio. Instead, the problem appears to be rooted in an overestimation of the differential recoiling cross-section for hydrogen. This would imply that the screening length for hydrogen interacting with another collision partner is too high. It is common practice to adjust the screening length in cases where calculated results are at variance with experiment. The correction factor provided by O'Connor and MacDonald [101] did not provide any improvement of the H(DR)/C(DR) ratio.

Hydrogen with $Z=1$ represents an extreme case in atomic collisions. The Thomas–Fermi statistical atomic model is based on the assumption that the electrons around an atomic nucleus can be regarded as a degenerate electron gas with its charge density uniformly distributed. Consequently, individual properties of the electrons are lost in the statistical model. The Thomas–Fermi theory is mainly applicable to many-electron systems where a statistical treatment is justified. Furthermore, the collision of a moderate speed heavy atom with a stationary H atom corresponds, in the center-of-mass system, to a collision of a slow H atom with a stationary heavy atom. This emphasizes the low-energy and large-separation regions of the potential energy functions, just where they are least well known for condensed matter targets. Hydrogen's calculated, abnormally high differential recoiling cross-section is currently being investigated further by the authors.

4.4.4.2. Monocrystalline Hexatriacontane

Bertrand et al. [98] applied DRS to obtain the molecular orientation at the surface of organic polymers. They measured the fluxes of H and C atoms recoiling from 4 keV Ar^+ collisions with the surface of monocrystalline hexatriacontane (paraffin). The paraffin's carbon backbone was oriented vertically in the surface, which was terminated by methyl groups. Their example of a TOF spectrum is shown in Fig. 4.10 together with our calculated spectrum. The experimental parameters include a recoil angle of $\phi = 35^\circ$ and a drift length of 90 cm. Bertrand et al. do not explicitly state the angle of incidence, α , for this particular TOF spectrum. An incident angle of $\alpha = 6^\circ$ was chosen for the calculation based on an inspection of their α -scan

data. Furthermore, the exact response function of the particle detector used by Bertrand et al. is unknown to us. Eq. (4.1) was therefore employed as an estimate to adjust the calculated TOF spectrum. Fig. 4.10 shows the similar trend in calculated recoil intensity as did Fig. 4.9. The H(DR)–C(DR) peak separation is very closely reproduced, while the H(DR)/C(DR) peak intensity ratio is grossly overestimated.

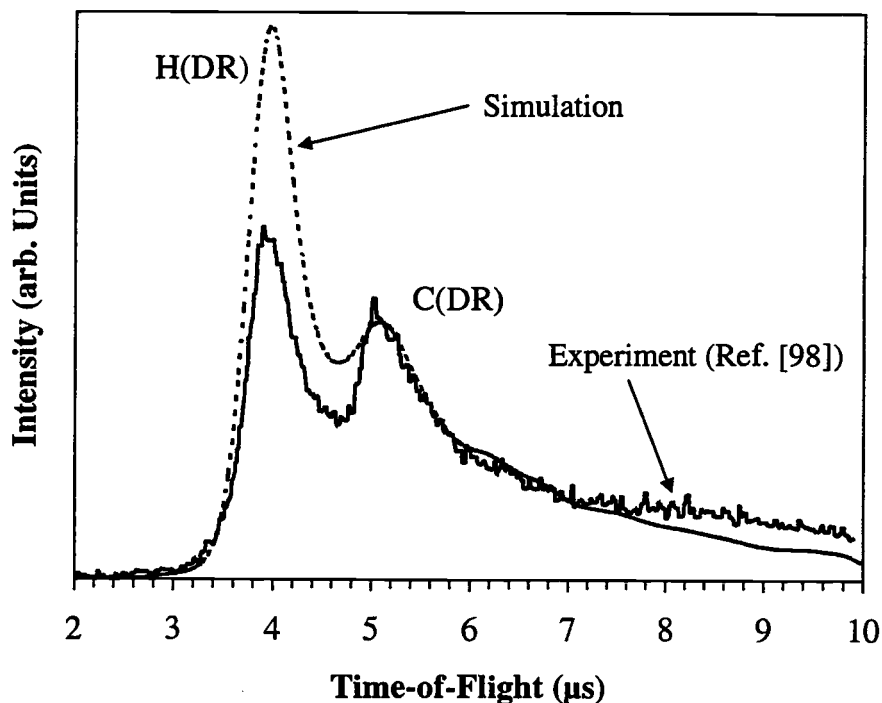


Fig. 4.10 Comparison of an experimental TOF–DRS spectrum for hexatriacontane with simulation. Intensities were normalized to the C(DR) peak maximum. Similar to Fig. 4.9, the significantly higher H/C ratio in the simulation appears to be rooted in an overestimated differential recoil cross-section for hydrogen. See text for details. (4 keV Ar⁺, $\alpha = 6^\circ$, $\phi = 35^\circ$, drift length 90 cm).

A detection-efficiency independent comparison of experimental data with simulation is provided by an α -scan, the variation of the C(DR) signal as a function of the incident angle α . Fig. 4.11 shows the experimental data, again those of Bertrand et al., compared to the results of our calculations. The intensities were obtained by

integrating narrow time windows (≈ 200 ns) centered under the carbon TOF peak maximum. The experimental and simulated α -scan maxima overlap in position very well. The slopes of the rising and falling edge of the calculated curve are steeper than those of the experiment, which suggests a difference in surface properties. The critical angle α_c , below which significant shadowing of the incident projectile by target atoms in the surface occurs, is defined as the α corresponding to 50% of the peak maximum on the low- α side of the scan. The critical angles based on the experimental data and the simulation are $\alpha_c^{\text{exp}} = 2.5^\circ \pm 1^\circ$ [98] and $\alpha_c^{\text{sim}} = 4.3^\circ \pm 0.5^\circ$, respectively.

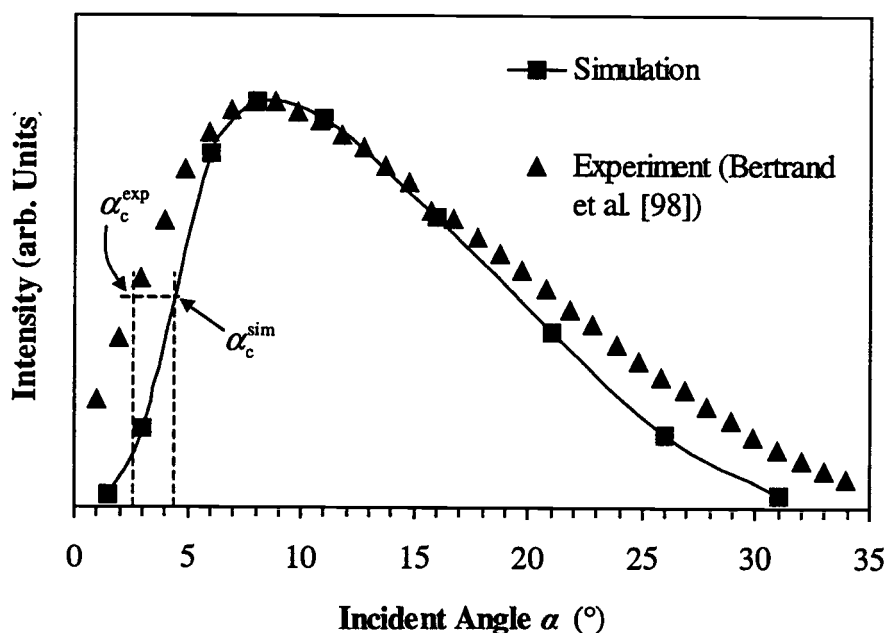


Fig. 4.11 Incident angle α -scan of directly recoiled carbon atoms from hexatriacontane. Experimental data were taken from Ref. [98] and compared to simulation (4 keV Ar^+ , $\phi = 35^\circ$). The α_c^{exp} and α_c^{sim} values are indicated.

The difference can be explained by the fact that the simulated HTC surface is atomically smooth. Vertical motion of the molecules with respect to each other was not considered in the simulation. Upwardly displaced molecular chains at random intervals would create varying sizes of the apparent surface unit cell. The shadow

cones of surface atoms no longer overlap with atomic positions of neighboring molecules unless the beam incident angle α is reduced. Introducing surface roughness into the simulation would cause α_c to be smaller and the slopes of both the rising and falling edge in the simulated α -scan to be less steep than for an atomically smooth HTC surface.

4.5. Summary

The simulation results confirm the high surface sensitivity of DRS and reveal the dependence of the sampling depth on the primary ion type and energy. Recoils originating at greater depths in the modeled targets are more easily produced by primary projectiles of low mass and high energy. In the case of diamond, mostly the top 1–2 Å were sampled by the 2–4 keV Ar⁺ and Ne⁺ simulated ion beams. The model of the hydrogen-rich and structurally less dense alkane polymer permits penetration to deeper layers. For small beam incident angles α or exit angles β , approximately (70±5)% of all recoils come from the methyl group (top 1 Å), and 30% stem from 2–5 Å below the surface. When $\alpha \cong \beta$, the methyl groups contribute roughly 50% to the recoil intensity, while the adjacent first (2–2.5 Å) and subsequent (3–10 Å) CH₂ groups contribute ~25% each.

A recoil's location in the TOF-intensity tail results from complex multiple-collision mechanisms and is not directly correlated to its depth of origin. Every target layer is represented in the TOF tail down to the maximum penetration depth.

Comparison of simulated and experimental results revealed that the Molière potential used to model the atomic collision cascades appears to overestimate the differential recoiling cross-section for hydrogen. The ZBL and AMLJ potentials as representatives of other interaction potentials widely used in trajectory calculations within the framework of the binary collision approximation did not yield any improvement. This seems to indicate a breakdown of fundamental assumptions in the interaction potential when applied to extremely low- Z target atoms.

Chapter 5

A Correction Factor to the Screening Radius for Atomic Interactions Involving Hydrogen and its Application in Direct Recoil Spectrometry

Michael Tassotto and Philip R. Watson

Submitted to Surface Science
Department of Physics
Copyright ©2000, Oregon State University.

5.1. Abstract

The screening function of the atomic interaction potential in low-energy ion scattering and recoiling was investigated for collisions involving hydrogen. Time-of-flight direct recoil spectrometry (TOF–DRS) and the MARLOWE computer code were used to derive a correction factor, with explicit atomic-number dependence, to the screening radius specific to X–H interactions, where X represents any other atom. The improved screening radius was tested in the simulation of TOF spectra. The observed results displayed very good agreement with experimental data. The application of this correction factor in computer simulation studies of ion-surface interactions involving H should improve the exactness of the calculations and lead to more accurate differential interaction cross-sections.

5.2. Introduction

The direct detection of surface hydrogen is not possible by most of the conventional experimental techniques. A powerful solution to this problem was provided by the development of the technique of time-of-flight direct recoil spectrometry (TOF–DRS), first suggested by Chen et al. [30]. One of the important capabilities of DRS is its high sensitivity to surface H ($\sim 10^{-3}$ of a monolayer [102]), allowing direct monitoring of the hydrogen coverage in adsorption experiments and in film growth. Many applications of surface H detection by DRS have been described in a number of reviews [31,32,103].

In TOF–DRS, a pulsed rare gas ion beam of low energy (1–10 keV) is incident on the studied surface at grazing angles. Directly ejected surface atoms (direct recoils, DR), including light adsorbates like H, are analyzed in time-of-flight measurements. While qualitative identification of surface H recoils is straightforward, quantitative analysis requires relating the flux of directly recoiled H, e.g. the peak intensity or signal, S_H , in the measured TOF spectrum, to the surface H concentration, C_H ,

$$S_H \propto C_H \varepsilon_H \sigma_H^r(E_0, E_r, \phi), \quad (5.1)$$

where ε_H and $\sigma_H^r(E_0, E_r, \phi)$ represent the detection efficiency and differential recoil cross-section for H recoils, E_0 is the kinetic energy of the projectile, E_r and ϕ are the kinetic energy and recoil angle of the ejected surface H, respectively. Relation (5.1) omits such factors as the incident flux of the primary ions, a function representing the experimental geometry, and a so-called masking factor that accounts for shadowing and blocking effects in the surface [31]. In order to avoid having to make assumptions about these additional factors, most researchers frequently look at peak intensity ratios,

$$S_H / S_j = (C_H \varepsilon_H \sigma_H^r) / (C_j \varepsilon_j \sigma_j^r), \quad (5.2)$$

and their variations as function of polar and/or azimuthal angles of incidence to infer compositional and structural information about the surface studied. The most sought-after quantity of real information is not the left-hand-side of Eq. (5.2), because that is measured experimentally, but the ratio of atomic composition, C_H/C_j . Those calculated ratios are very sensitive to even slight changes in S , ε , or σ^r . Thus, these quantities have to be accurately known in order to extract useful numbers from TOF spectra.

A functional form for ε was recently determined by the authors [65]. Furthermore, a computer simulation study [66] of recoil depth distributions and multiple scattering contributions to TOF spectra in DRS was recently completed. While this study verified the high surface sensitivity of the DRS technique, it also showed that the extraction of absolute numbers (S) for DR intensities from TOF spectra is not a trivial task due to possible contributions from near-surface layers and peak overlap. Furthermore, TOF spectra simulated for Ar^+ ions impinging upon a hydrocarbon surface grossly overestimated the H(DR) contribution when compared to experimental data. It was pointed out that this discrepancy seemed to be the result of the interaction potential used in the simulations.

In other studies, Schultz et al. [104,105] attempted to calibrate the surface H concentration using TOF-DRS on methoxylated magnesium. An ancillary objective of

their work was to determine if theoretical differential DR cross-sections are reliable for predicting H recoil intensities for systems of known concentration. They found that the calculated cross-section ratio for H(DR)/C(DR) did not successfully reproduce the experimental one and that it was too large by a factor of about four. It was acknowledged that the disagreement between theory and experiment was substantial and outside of experimental error.

This article focuses on the differential interaction cross-section, σ , between a projectile of mass M_0 and energy E_0 colliding with a hydrogen atom. We propose a correction factor to the screening radius used in interatomic potentials to describe the interaction between H and another collision partner at energies typical for DRS (1–10 keV). This correction factor should make possible the calculation of more accurate interaction cross-sections involving H. In the following section, we discuss the origin of the problem leading to overly large H interaction cross-sections obtained from calculations. Sections 5.4 and 5.5 provide details about the experimental and computational approach before the results and their comparison to experimental data are discussed in Section 5.6.

5.3. Theoretical Considerations and Potentials

Screened Coulomb potentials have extensively been used to describe the physics of atomic collisions between charged particles and matter. Their basic structure consists of a Coulomb repulsion term that is modified by a screening function $\chi(r/a)$,

$$V(r) = \left(Z_1 Z_2 e^2 / r \right) \chi(r/a), \quad (5.3)$$

where Z_1 and Z_2 are the atomic numbers of the incident and target particles, respectively, e is the elementary charge, r is the interatomic separation, and a is a characteristic distance called the screening length or radius. The choice of the screening function depends on the conditions of the problem under consideration and on the accuracy required. The books by Torrens [38] and Mashkova and Molchanov [37] contain detailed discussions on interaction potentials. The physics of atomic

collisions make wide use of potentials with screening functions based on the Thomas–Fermi statistical atomic model. Many empirical approximations of the screening function are known. Among the most commonly used ones in binary collision and Monte Carlo computational codes for trajectory calculations are the approximations by Molière [49] and Ziegler, Littmark and Biersack (ZBL) [51]. They express the screening function in terms of a sum of exponentials,

$$\chi(r/a) = \sum_i \alpha_i \exp(-\beta_i r/a), \quad (5.4)$$

with $\alpha_i = (0.35, 0.55, 0.10)$, $\beta_i = (-0.3, -1.2, -6.0)$ for the Molière potential and $\alpha_i = (0.1818, 0.5099, 0.2802, 0.02817)$, $\beta_i = (-3.2, -0.9423, -0.4028, -0.2016)$ for the ZBL potential. The screening radius, a , can take on various forms depending on the range of distances encountered in energetic collisions. In fact, it can be and has been treated as an adjustable parameter. Frequently used forms of the screening radius were given by Firsov [50], a_F (known as the *Firsov screening length*), and Lindhard et al. [62], a_L ,

$$a_F = 0.88534 a_0 \left(Z_1^{1/2} + Z_2^{1/2} \right)^{-2/3}, \quad (5.5)$$

$$a_L = 0.88534 a_0 \left(Z_1^{2/3} + Z_2^{2/3} \right)^{-1/2}, \quad (5.6)$$

where a_0 is the Bohr radius, 0.529 \AA .

The problem that calculated interaction cross-sections for hydrogen recoils do not successfully reproduce experimental data in the low-energy collision regime is best illustrated by an example of a plot of recoil cross-sections. The Molière potential and the Firsov screening length were used to calculate differential recoil cross-sections, $\sigma^r(E_0, E_r, \phi)$, for Ar^+ ions ($E_0 = 2.5 \text{ keV}$) colliding with various target nuclei at a recoil angle $\phi = 45^\circ$. [This particular approximation to the interaction potential was chosen, as alluded to earlier, because of its popularity and wide spread use. It has found numerous applications in areas such as shadow and blocking cone calculations for the determination of adsorption site geometries and trajectory calculation codes

based on the binary collision approximation.] The calculations were performed with the TABULA program, which is part of the MARLOWE computer code (version 14c) [29]. TABULA follows closely the explicit formulas for cross-section calculations given in Ref. [46]. Values for $\sigma^r(E_0, E_r, \phi)$ as a function of target mass are shown in Fig. 5.1 (solid squares).

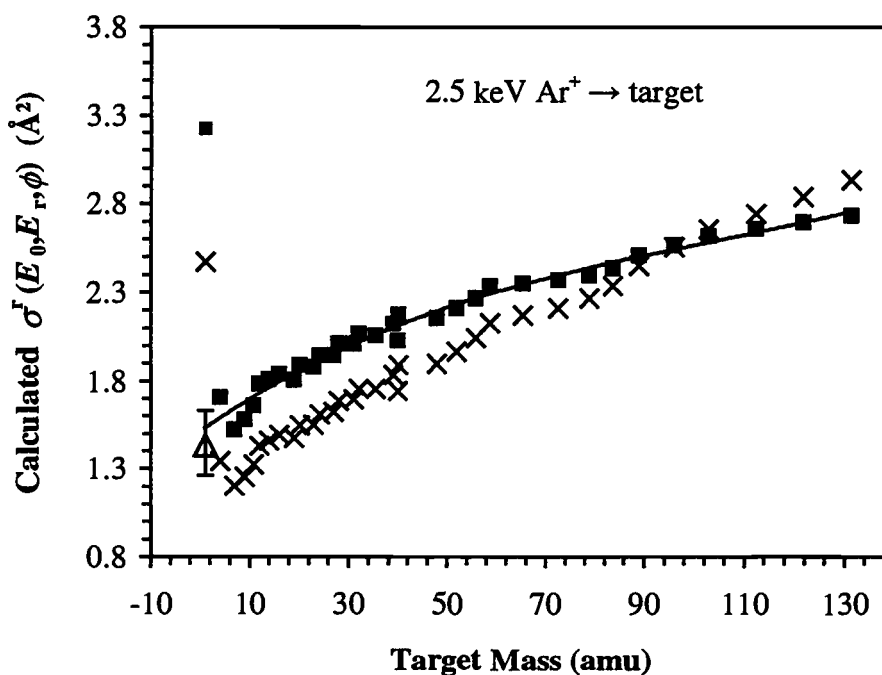


Fig. 5.1 Differential recoil cross-section as function of target mass calculated for collisions with a primary Ar^+ projectile. $E_0 = 2.5$ keV, $\phi = 45^\circ$. The solid squares result from calculations using the Molière potential with the Firsov screening length, a_F , from Eq. (5.5). The trendline is there to guide the eye. The crosses include O'Connor and MacDonald's correction factor to a_F [see Eqs. (5.7) and (5.8)]. The open triangle shows σ^r for H based on the screening radius, a_{X-H} , obtained from Fig. 5.4 (see Section 5.6.2).

Two general observations can readily be made. First, following the solid trendline toward decreasing target mass numbers, σ^r is steadily decreasing. Second, the differential recoil cross-section for H ($\sigma^r = 3.22 \text{ \AA}^2$) deviates strongly from the overall trend, which would place it at $\sim 1.5 \text{ \AA}^2$. A more detailed discussion of this deviation is necessary and will be done in the following paragraphs.

As Rabalais [31] pointed out in his review article on DRS, the cross-section for H interacting with other atoms appears to be “abnormally high”. His discussion, based on a simple Coulomb or inverse-square potential, isolates the mass dependence of σ^r , which turns out to be roughly proportional to $(M_1 + M_2) / M_2$. M_1 and M_2 are the masses of the projectile and the struck target atom, respectively. This mass factor is large for H targets because $M_2 = 1$, resulting in a large σ^r . This would make DRS not just sensitive to surface H, but *particularly* or *favorably* sensitive. However, one has to ask the question whether this abnormally high cross-section for H recoils is physically plausible (especially when calculations are consistently at variance with experiment) or merely a consequence of the algebra involved in these simple potentials.

A very good indication for an answer to this question can be found by looking at the theoretical foundation of the Thomas–Fermi statistical atomic model on which many empirical interatomic potentials, such as the Molière potential, are built. The Thomas–Fermi model is based on the assumption that the electrons around an atomic nucleus can be regarded as a degenerate electron gas at absolute zero temperature [106]. The electronic charge density is uniformly distributed; electrons are “pulverized” or “smeared out”. Consequently, individual properties of the electrons are lost in the statistical model, which is primarily applicable to many-electron systems where a statistical treatment is justified. As for hydrogen, a statistical approach loses its meaning. Empirical interatomic potentials, such as the Molière potential, become increasingly valid and applicable the higher the relative collision energies and atomic numbers of the colliding particles are.

Overbury and Huntley [107] investigated the validity of the Molière and ZBL potentials using low-energy ion scattering spectroscopy. They found that at 2.5 keV

the scattering of Li^+ , Na^+ , and K^+ from Mo(001) is adequately described by the Molière potential with use of a Firsov screening length reduced by factors of Γ ,

$$a = \Gamma a_F, \quad (5.7)$$

where $\Gamma = 0.90, 0.95$, and 1.0 for Li^+ , Na^+ , and K^+ , respectively. Their empirically determined Γ factors were in excellent agreement with calculated values based on a correction factor to the interatomic potential screening function given by O'Connor and MacDonald [101]. The latter group parameterized a large body of gas-phase scattering data to determine an effective screening function and expressed their results by the following formula

$$\Gamma = 0.69 + 0.0051(Z_1 + Z_2). \quad (5.8)$$

Making use of O'Connor and MacDonald's correction factor by including Eqs. (5.7) and (5.8) in the cross-section calculations done for 2.5 keV Ar^+ above, one obtains somewhat different values for σ^r which are represented by crosses in Fig. 5.1. Again, the same observations mentioned earlier hold true. A steady decline of σ^r values with decreasing target mass (although the general slope is slightly steeper) stands in contrast to the sharp rise in the differential recoil cross-section for H. This is not at all unexpected, given the monotonic behavior of Γ . While the Molière potential with the Firsov screening length corrected by O'Connor and MacDonald's Γ factor seem adequate for Li^+ and heavier ions colliding with a Mo target, their straight application to H with atomic number $Z = 1$ does not lead to a satisfactory agreement between theory and experiment as outlined above.

It appears that the H single-electron system represents a unique case that existing theory does not handle well. The present study does not attempt to formulate a new theoretical framework encompassing hydrogen. Instead, a correction factor to the screening radius specific to hydrogen is derived from experiment. A brief outline of the approach taken in this study to improve the convergence of calculated recoil cross-sections involving hydrogen on experimentally derived ones goes as follows. First, an

experimental TOF spectrum for 2.5 keV Ar^+ ions incident upon an H-containing surface of known structure and composition was recorded. This spectrum was to serve as a standard for relative peak intensities. Liquid heptadecane ($\text{C}_{17}\text{H}_{36}$) at a temperature of 23°C was used. The choice of target surface and experimental geometry will be addressed in detail in Section 5.4. Second, actual TOF spectra based on parameters identical to the experiment were calculated using the MARLOWE program. The calculations were repeated while systematically changing the interaction strengths (via a modified screening radius $a_{\text{X-H}}$) between Ar-H, C-H, and H-H. The screening radius yielding the best match between the experimental and calculated H/C peak intensity ratio was then employed in additional calculations. Finally, these additional calculations were compared to a set of experimental TOF spectra recorded under conditions of varying projectile mass, energy, and angle of incidence.

5.4. Experimental Method

Liquid heptadecane ($\text{C}_{17}\text{H}_{36}$, Aldrich) was used in this study for a number of reasons. It is a linear hydrocarbon molecule, which should lend itself to simple interpretation in TOF spectra because only two recoil peaks due to H and C are expected. It is inexpensive, easy to work with, and has a vapor pressure low enough ($\sim 1.5 \times 10^{-5}$ Torr) to be used in a differentially pumped vacuum system for TOF analysis. Heptadecane belongs to a group of n-alkanes that have been reported to form an ordered surface layer in the liquid within a temperature range of $2\text{--}3^\circ\text{C}$ above their bulk freezing points (22.5°C for $\text{C}_{17}\text{H}_{36}$). See, for instance, [11] and references therein. On cooling from above that temperature, a phase change occurs, producing an ordered monolayer in which the molecules' carbon backbones are aligned parallel to the surface normal. Hence, the surface is terminated by chain-end methyl groups and its relative H/C concentration (3/1) is known.

The applicability of other H-containing surfaces to serve as a model and standard for surface H concentration was investigated. Due to the approach being taken in this article, the search for a suitable system was limited to literature data based on the technique of TOF-DRS. While a lot of work has been done in this field, actual TOF

spectra of the surfaces studied (to serve as models) are frequently omitted from articles. An obvious but only choice could have been the aforementioned studies by Schultz et al. [104,105] on methoxylated magnesium. However, expectations of a well-defined surface with known atomic composition were frustrated by factors such as a 40% uncertainty in methoxide coverage and a small population of hydroxide and magnesium hydride present on or in the surface. Furthermore, one now deals with four elements (H, C, O, and Mg) instead of two. This could provide a more stringent test of the applicability of results obtained, however, at the same time, it adds unwanted complexity to the computer simulations. In fact, preliminary TOF calculations done on this system proved too sensitive to the exact surface model employed, e.g. bond lengths, coverage, amounts of MgH included and their location in the surface. Finally, the use of literature data is further complicated by the lack of knowledge of the actual detection efficiency function, ε , of the particle detector used. For the reasons outlined above and the fact that ε is known [65] for our time-of-flight direct recoil spectrometer, heptadecane was found to be a very suitable model surface.

All TOF spectra on liquid heptadecane presented herein were recorded with our TOF-DR spectrometer, a detailed description of which can be found elsewhere [27,64,74]. Ion beam energies of 2.5 and 2.2 keV were used for Ar^+ and Ne^+ , respectively. They fall within the range of energies commonly used in DRS and ensure a linear response of the particle detector (channel electron multiplier) to impinging recoils from the target surface. The recoil angle, ϕ , and the drift length, L , of the time-of-flight leg were, unless otherwise noted, 45° and 112 cm, respectively.

5.5. Simulation Model

The MARLOWE computer code (version 14c) [29] was used to simulate the experimental TOF spectra presented in this study. Hexagonal packing for the ordered monolayer of $\text{C}_{17}\text{H}_{36}$ molecules was assumed with a chain-chain separation of 4.77\AA [100]. The $\text{C}_{17}\text{H}_{36}$ surface was configured to extend laterally without boundaries. Its depth into the bulk was limited to 30\AA . This restriction was imposed in order to

minimize computation time. Calculations with thicker targets displayed no changes in the results, proving that this thickness was sufficient.

The impact points on the surface for 3×10^6 primary projectiles per simulation were uniformly distributed. Although the $C_{17}H_{36}$ molecules align themselves vertically in the surface at the phase transition temperature, as discussed above, their rotational degree of freedom about an axis parallel to the surface normal is assumed to be unrestricted. Therefore, the original MARLOWE code was edited in order to allow for randomization of the azimuthal direction of beam incidence.

The modeled $C_{17}H_{36}$ surface is atomically smooth except for thermal vibrations. The target atoms were allowed to undergo uncorrelated thermal vibrations with a surface temperature identical to experimental conditions. The vibrational amplitudes were based on mean square amplitudes for diatomic molecules [99] and were on the order of 0.1 \AA or smaller.

The simulated detector was situated at a recoil angle $\phi = 45^\circ$ with respect to the initial direction of travel of the primary ion and had an acceptance angle of 3° , which is five times more than the real detector. This reduced calculation times by a factor of 25. The calculated TOF intensity distributions of recoils were adjusted in two ways. First, the raw TOF data were convoluted with a Gaussian (area) function to simulate the finite pulse width (170 ns) of the incident ion beam in the experiment. Second, the thereby obtained intensity distribution was multiplied by $\mathcal{E}(v, Z)$, the detection efficiency function of our particle detector [65].

The authors have previously discussed a very similar set of computations and refer the interested reader to Ref. [66] for additional details on individual simulation parameters.

5.6. Results and Discussion

5.6.1. *The Surface of Liquid Heptadecane*

The first step in using heptadecane as a model surface with known structure and composition is to show evidence of the presence and absence, respectively, of the

ordered monolayer at temperatures just above (23°C) and much higher (41°C) than the liquid's melting point. For this purpose, TOF spectra resulting from bombarding the $\text{C}_{17}\text{H}_{36}$ surface with Ar^+ ions were recorded for a range of incident angles, $\alpha = 4\text{--}32^{\circ}$. An example of a TOF spectrum obtained for 2.5 keV Ar^+ ions impinging on the heptadecane surface ($T = 23 \pm 0.5^{\circ}\text{C}$) at $\alpha = 8^{\circ}$ is shown in Fig. 5.2. Only peaks due to recoiling H and C atoms are observed. Identification of the peaks is achieved by straightforward application of physical conservation laws for energy and linear momentum in binary collisions [31].

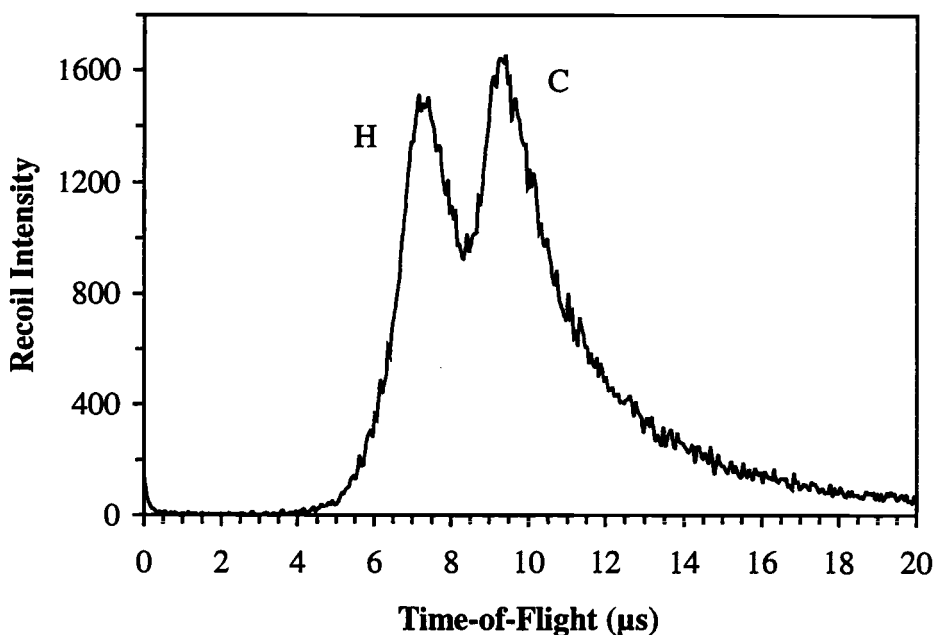


Fig. 5.2 TOF spectrum showing hydrogen and carbon recoil peaks resulting from Ar^+ bombardment of liquid heptadecane. The incident angle $\alpha = 8^{\circ}$ with respect to the surface. The primary ion energy $E_0 = 2.5$ keV, the recoil angle $\phi = 45^{\circ}$, and the drift length is 112 cm.

Relative peak intensity ratios, $S_{\text{H}}/S_{\text{C}}$ (also denoted as H/C), were obtained by integrating narrow time windows (~ 250 ns) centered under the respective TOF peak maxima after a five-point smoothing function had been applied three times to reduce

noise. It is obvious that the tail of the H recoil peak at longer flight times overlaps with the C recoil peak, thereby adding to S_C . However, deconvolution of the peaks for accurate extraction of absolute numbers for S_H and S_C is not trivial [66]. Fortunately, this is not necessary because only the relative peak-intensity variations are important when looking for structural evidence of preferential ordering of $C_{17}H_{36}$ molecules in the top monolayer at $T = 23^\circ\text{C}$ and disorder at higher temperatures.

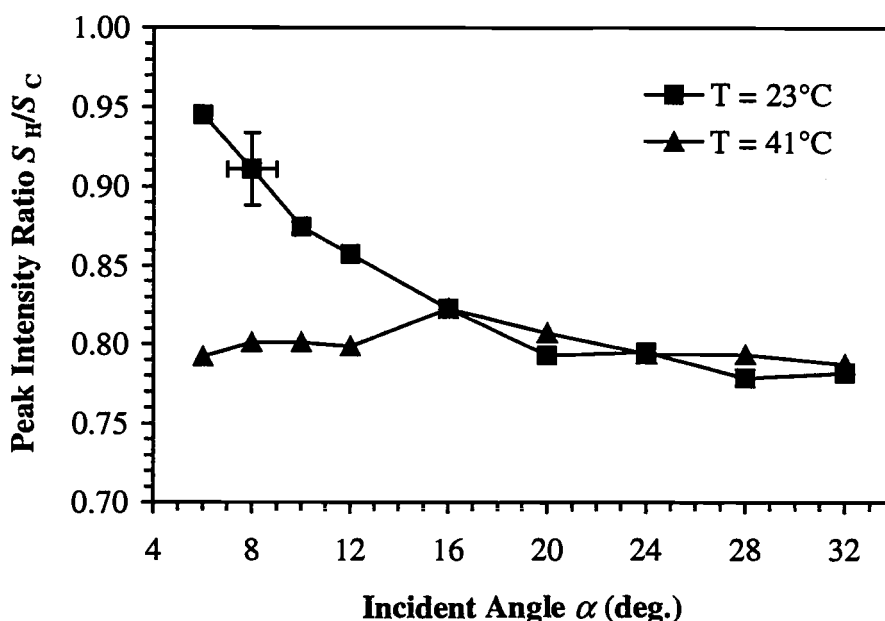


Fig. 5.3 Measured peak intensity ratios, S_H/S_C , versus beam incident angle α . Solid squares and solid triangles are for liquid heptadecane at 23 and 41°C, respectively. Error bars represent a 1° uncertainty in the incident angle α and an absolute 5% uncertainty in the intensity ratio.

Fig. 5.3 shows a compilation of the measured peak intensity ratios, S_H/S_C , as a function of the incident angle α . The cross of error bars represents a $\pm 1^\circ$ uncertainty in α and an absolute 5% uncertainty in the intensity ratio after smoothing. Both tolerances are believed to be upper limits for very conservative error estimates. As can be seen from Fig. 5.3, the relative peak intensity for the range of incident angles $16^\circ \leq \alpha \leq 32^\circ$ remains almost constant at both $T = 23$ and 41°C . While at the latter

temperature the H/C ratio continues to remain constant toward smaller incident angles, this is clearly not the case at 23°C. Instead, the H/C ratio now increases steadily as α decreases and reaches a maximum at $\alpha = 4^\circ$.

At shallow incidence (small α), the ion beam primarily probes the topmost surface layer [66]. In the ordered monolayer (23°C), where the liquid is terminated predominantly by chain-end methyl groups, the relative abundance of H with respect to C is $\sim 3/1$. This ratio is expected to be smaller at 41°C because the molecules are now randomly orientated which exposes entire molecules at the surface and not just their methyl groups. This is confirmed by the observations in Fig. 5.3 at small α where S_H/S_C differs considerably for the two temperatures. As α increases, the ion beam starts to probe beneath the surface where, independent of the molecules' orientation, the relative abundance of H to C is dominated by CH_2 groups. Furthermore, with increasing α it is expected that the initially higher H/C ratio for the ordered monolayer begins to drop. While it is true that the ion beam produces more recoils at greater depths when α is increased [66], the majority ($\sim 50\%$) of the recoil signal originates, nonetheless, in the top 1 Å of the liquid. Hence, the H/C ratio for the ordered monolayer should therefore, at larger α , only approach but not reach the one for the disordered liquid. This is not observed in Fig. 5.3 where the H/C ratio is the same at incident angles $\alpha \geq 16^\circ$ for both temperatures. This seems to indicate that although a preferred vertical alignment of heptadecane molecules did occur in the surface at a temperature of $T = 23^\circ\text{C}$, a complete monolayer of ordered $\text{C}_{17}\text{H}_{36}$ molecules did not form. As will be discussed below, the extent to which this posed a problem for the objective of this study was very limited.

5.6.2. Empirical Estimation of the Screening Radius a_{X-H}

Fig. 5.4 shows an experimental TOF spectrum (solid line) resulting from 2.5 keV Ar^+ bombardment of liquid heptadecane at 23°C at an incident angle $\alpha = 16^\circ$. This TOF spectrum is compared in Figs. 5.4a–f to calculated ones. Intensities were normalized to the experimental C(DR) peak. In the simulated TOF spectra, the

strength of the atomic interaction between a collision partner 'X' and H was systematically changed via the screening radius, a_{X-H} . Here, 'X' encompasses Ar, C, and H. The Molière potential was used for all simulations.

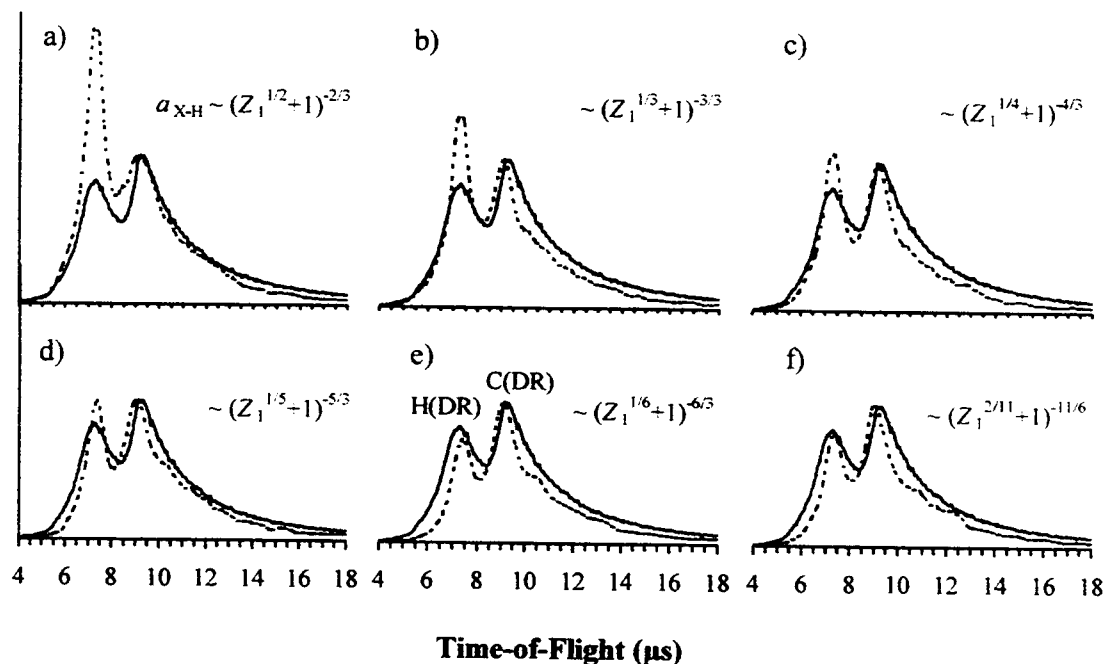


Fig. 5.4 Comparison of calculated TOF spectra (dashed line) with an experimental one (solid line) for 2.5 keV Ar^+ bombardment of liquid heptadecane at 23°C and $\alpha = 16^\circ$. The screening radius, a_{X-H} ('X' = Ar, C, H), was systematically changed as indicated in each plot. The Molière potential was used for all simulations. Intensities are normalized to the experimental C(DR) peak. Fig. 5.4f shows the best fit.

Fig. 5.4a shows a result from an earlier simulation study [66]. Here, $a_{X-H} = a_F$, the Firsov screening length from Eq. (5.5). The simulation grossly overestimates the H(DR) contribution to the spectrum. Following Figs. 5.4b–e, the screening radius is systematically made smaller by choosing different exponents for the atomic-number dependence of a_{X-H} . A continual drop in H(DR) intensity is observed until, in Fig. 5.4e, the simulated H(DR) intensity goes below the experimental one. Fig. 5.4f shows the best match of the relative H/C peak intensities between experiment and

simulation. All calculated spectra exhibit peak widths that are smaller compared to the experiment, which is a result of the surface model used for heptadecane. This will be addressed in Section 5.6.3.1.

A few comments about the screening radius a_{X-H} are necessary. It has to be stressed that the functional form of the atomic-number dependence of the various screening radii in Figs. 5.4b–f is not based on any solid theoretical foundation. However, two considerations went into choosing the respective exponents. The first one is based on an argument given, for instance, by Mashkova and Molchanov [37]. When the nuclear charge of one of the interacting particles is much lower than that of the other one, as is the case for a proton interacting with a heavy atom, the screening radius is assumed to be equal to the screening radius of the isolated heavy atom (with atomic number Z_1), so that $a = 0.88534 a_0 Z_1^{-1/3}$. The other consideration concerns the applicability of an improved screening radius to calculate more accurate differential interaction cross-sections between H and *any* other collision partner using the Molière potential. It is common practice to use correction factors to the screening radius as adjustable parameters in computer calculations to obtain a better fit to experimental data. However, those empirically derived correction factors exclusively apply to the very system under study because they are generally given as a numerical value (for instance, 0.90 for Li^+ scattering from Mo [107]). As discussed earlier in Section 5.3 above, O'Connor and MacDonald [101] derived a functional form for a correction factor with explicit atomic-number dependence. The goal is the same in this study. Instead of arbitrarily choosing a correction factor, with which to scale the screening radius between only one projectile, say Ar, and H, a functional expression was sought that would directly depend on the atomic numbers of H and its collision partner. An obvious choice was to stick to the general form of the screening radius. The expression for a_{X-H} in Fig. 5.4f,

$$a_{X-H} = 0.88534 a_0 \left(Z_1^{2/11} + 1 \right)^{-11/6}, \quad (5.9)$$

certainly displays somewhat unusual exponents. Nonetheless, it yields a very close fit to the experimental TOF spectrum's H/C intensity ratio.

The empirically derived screening radius given in Eq. (5.9) can now be used to recalculate the differential recoil cross-section for an H atom being struck by a 2.5 keV Ar⁺ ion. The result is shown in Fig. 5.1 by the open triangle. The positive and negative error bars associated with it were estimated from σ^r - values based on the screening radii from Figs. 5.4d and e. Notice that the recalculated cross-section now follows the overall trend of $\sigma^r(E_0, E_r, \phi)$ as a function of target mass. A plot identical to Fig. 5.1 was calculated for a primary Ne⁺ projectile. The agreement of the recalculated σ_H^r - value for H with the trendline was even closer here than for Ar⁺ in Fig. 5.1.

5.6.3. Test of a_{X-H} in TOF Simulations

The screening radius in Eq. (5.9) was used in additional TOF simulations in order to test its applicability to a different projectile atomic number, Z_1 , and initial kinetic energy, E_0 . In the following first two subsections, 2.5 keV Ar⁺ and 2.2 keV Ne⁺ ion bombardments of the disordered liquid surface of heptadecane at a temperature of 41°C are discussed. Experimental TOF spectra were recorded at three different angles of incidence, $\alpha = 12, 20,$ and 28° .

$T = 41$ instead of 23°C was chosen because the formation of a complete monolayer of ordered C₁₇H₃₆ molecules in the experiment is not guaranteed, as was discussed in Section 5.6.1. However, what can be assured is the complete randomness with which the molecules are oriented in the liquid, including its surface, at 41°C. This enables us to not only test Eq. (5.9) but also to show whether the simulations are able to reproduce the constancy in relative H/C ratio that was observed in Fig. 5.3 for $T = 41^\circ\text{C}$.

When the MARLOWE code was created, it was intended for computer simulations of atomic collisions in crystalline solids. It does not model true liquids. The disorder of molecules in the MARLOWE calculations was simulated by randomly selecting a

rotation of the three-dimensional crystal structure at the start of each primary trajectory [43], in other words, by making heptadecane polycrystalline. Certainly, this does not represent an accurate model of a liquid's surface and problems might be anticipated. However, as will be discussed below, the most obvious result of this shortcoming was a reduced peak width in the calculated TOF spectra throughout all simulations. MARLOWE does also simulate amorphous crystals. This option was not employed because the structural integrity of the $C_{17}H_{36}$ molecules is thereby lost.

The third subsection discusses the 4.0 keV Ar^+ bombardment of an ordered thin film of an organic polymer, which provides a test of Eq. (5.9) at higher relative collision energies between Ar, C, and H.

5.6.3.1. 2.5 keV Ar^+ Bombardment of Heptadecane

Fig. 5.5 shows the comparison of calculated TOF spectra to experiment for 2.5 keV Ar^+ ion bombardment of the disordered liquid surface of heptadecane at a temperature of $41^\circ C$ for the incident angles $\alpha = 12, 20,$ and 28° . The increments on each graph's ordinate are identical. All calculated TOF spectra were normalized to the highest peak maximum in the $\alpha = 12^\circ$ spectrum to facilitate direct comparison of experimental and simulated relative H/C peak intensities at different angles of incidence. In each spectrum, the experimental data are represented by solid circles, the solid line shows the calculated TOF spectrum, and the dashed lines indicate the individual contributions to the calculated TOF spectrum from H and C recoils and multiply scattered Ar (denoted by H, C, and Ar(MS), respectively). Note that multiply scattered primary Ar projectiles contribute only minimally to the TOF tail at longer flight times.

The small peak labeled P in Fig. 5.5 is called the photon peak and is due to photons entering the detector as a result of inelastic collisions of the incident ions with target atoms. It served as a convenient way to calibrate time zero for the experimental spectra.

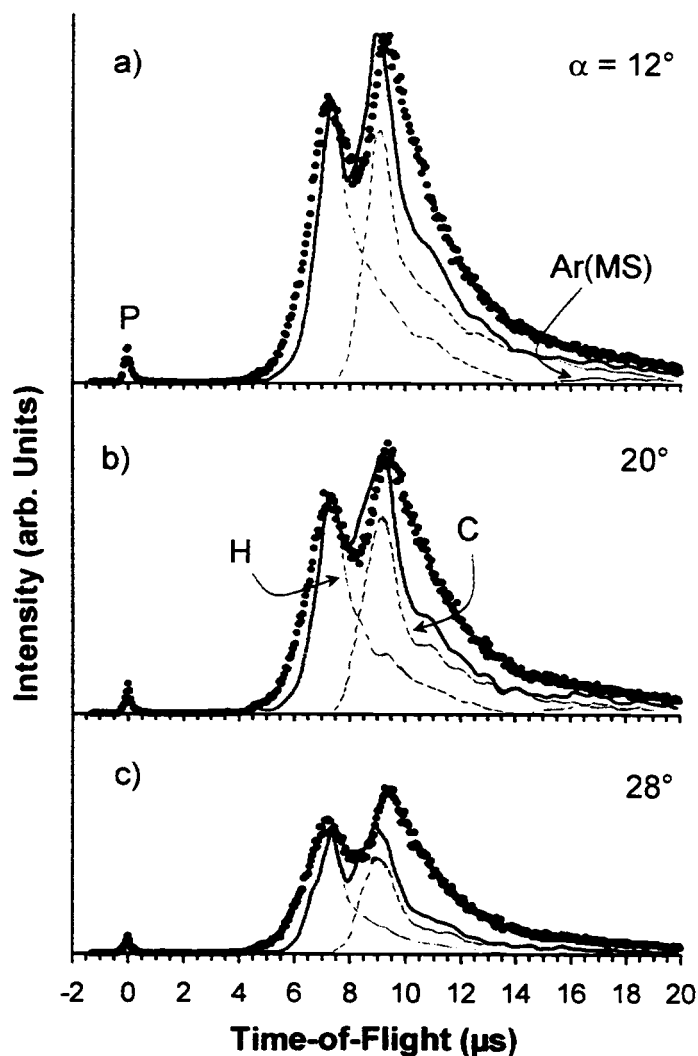


Fig. 5.5 Comparison of calculated TOF spectra (solid lines) to experiment (solid circles) for 2.5 keV Ar^+ ion bombardment of liquid heptadecane at 41°C for incident angles $\alpha = 12, 20,$ and 28° . All spectra are normalized to the highest peak maximum in Fig. 5.5a. The dashed lines indicate the individual contributions to the calculated TOF spectrum from H and C recoils and multiply scattered Ar. 'P' denotes the photon peak at time zero.

The calculated TOF spectra for $\alpha = 12$ and 20° reproduce the relative H/C peak intensity ratios very well. At $\alpha = 28^\circ$, only the H recoil intensity is closely matched, while the C recoil intensity falls short of the experimentally measured one. Furthermore, a reduced peak width and a slightly smaller peak separation between the

H and C direct recoil peaks are observed in all spectra. An explanation for this discrepancy is readily given by the polycrystalline model used to represent liquid heptadecane.

In the real liquid, a distribution of intermolecular distances of separation exists. Additionally, *gauche* defects in the linear hydrocarbon occur that cause deviations from the molecule's ideal *trans* configuration. On the contrary, in the polycrystalline model, the $C_{17}H_{36}$ molecules are merely rotated in a random fashion and a new surface is defined. The relative orientation of the molecules with respect to each other and all intermolecular distances of separation are maintained. This causes problems for some recoils (mostly C) wanting to escape the model surface into the particular direction of the detector ($\phi = 45^\circ$).

The majority of recoils contributing to a peak maximum in a TOF spectrum originates at or close to the surface and suffers only one large-angle deflection [66]. This is not the case for recoils away from the peak maximum in the sloping TOF tail at longer flight times. Here, more than one large-angle deflection frequently occur to slow down displaced target atoms. The random orientation of molecules in the real liquid allows these recoils to more easily escape the surface into all possible directions. Unlike the true liquid, the model target for heptadecane contains ordered rows of carbon zigzag chains that make up the molecules' backbones. This arrangement more effectively blocks recoils and limits the number of possible multiple scattering sequences leading to a recoil's escape into the proper solid angle.

The effects just mentioned are emphasized at larger α because the primary projectile probes deeper into the liquid's surface. The reduced simulated C recoil intensity in Fig. 5.5c supports this observation. The close agreement between the experimental and simulated H/C intensity ratios for $\alpha = 12$ and 20° is quite remarkable, considering that Eq. (5.9) was derived from a comparison of TOF spectra from an atomically smooth, perfectly ordered monolayer of $C_{17}H_{36}$ molecules (simulation) with a surface being only partially ordered (experiment), as discussed for Fig. 5.3. Thus, it is not believed that the formation of less than a full monolayer of vertically aligned $C_{17}H_{36}$ molecules in the 23°C liquid constituted a problem for the

derivation of a_{X-H} . More evidence for our confidence in this statement is given by the following Sections 5.6.3.2 and 5.6.3.3.

5.6.3.2. 2.2 keV Ne⁺ Bombardment of Heptadecane

The screening radius in Eq. (5.9) was derived from TOF spectra obtained from Ar⁺ bombardment of heptadecane. In order to test its applicability to a different atomic number, Z_1 , experimental and calculated TOF spectra similar to the ones discussed in the previous section and shown in Fig. 5.5 were obtained for 2.2 keV Ne⁺ ions. The results are displayed in Fig. 5.6. As in Fig. 5.5, the calculated TOF spectra were normalized to the highest peak maximum in the $\alpha = 12^\circ$ spectrum for direct comparison of relative H/C peak intensities. Again, experimental data are represented by solid circles, the solid line shows the calculated TOF spectrum, and the dashed lines indicate the individual contributions to the calculated TOF spectrum from H and C recoils and multiply scattered Ne (denoted by H, C, and Ne(MS), respectively).

While the initial kinetic energy of the primary Ne⁺ ions (2.2 keV) is very similar to the one used for Ar (2.5 keV) in Fig. 5.5, the lighter mass of the Ne projectile causes fundamental differences in both the simulated and experimental TOF spectra in Fig. 5.6. The H/C peak intensity ratio is now shifted in favor of H for the exact same target surface. The velocity of the H recoils plays the key-role in this change. Consider Eq. (5.2) showing the dependence of the H/C peak intensity ratio on the respective ratios of the differential recoil cross-sections, σ_H^r/σ_C^r , and the detection efficiencies, $\varepsilon_H/\varepsilon_C$. The former is nearly constant when going from 2.5 keV Ar to 2.2 keV Ne ($\sigma_H^r/\sigma_C^r = 0.80$ and 0.76 , respectively), while the latter changes from $\varepsilon_H/\varepsilon_C = 0.53$ to 0.74 .¹ The detection efficiency increases linearly with velocity before it reaches a plateau. The lighter 2.2 keV Ne⁺ ion transfers more kinetic energy in collisions with the H and C atoms than does a 2.5 keV Ar⁺ ion, thus creating faster recoils, which, in turn, cause an overall shift of the TOF spectrum to shorter flight times.

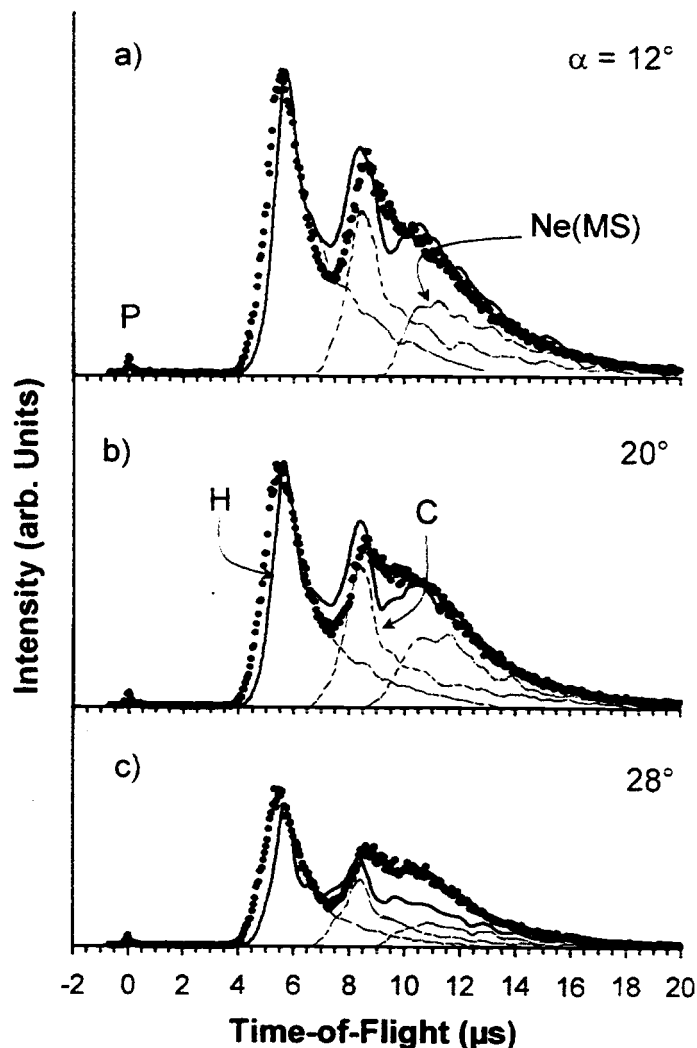


Fig. 5.6 Comparison of calculated TOF spectra (solid lines) to experiment (solid circles) for 2.2 keV Ne^+ ion bombardment of liquid heptadecane at 41°C for incident angles $\alpha = 12, 20,$ and 28° . All spectra are normalized to the highest peak maximum in Fig. 5.6a. The dashed lines indicate the individual contributions to the calculated TOF spectrum from H and C recoils and multiply scattered Ne. 'P' denotes the photon peak at time zero.

The calculated TOF spectra in Fig. 5.6 display a similar agreement with the experimental data as was found in Fig. 5.5. The recoil peaks are slightly too narrow

¹ $\sigma_{\text{H}}^r/\sigma_{\text{C}}^r$ was calculated using the Molière potential and Eq. (5.9) for Ar-H and Ne-H interactions and Eq. (5.5) for Ar-C and Ne-C interactions. $\varepsilon_{\text{H}}/\varepsilon_{\text{C}}$ was calculated based on Ref. [65].

and not as far separated from each other as in the experimental spectra. Notice that the multiple scattering contribution from Ne(MS) is much more intense than the vanishingly small one from Ar(MS) in Fig. 5.5. This is attributed to the larger critical angle, θ_c , for single scattering of Ne from C compared to Ar. When a massive projectile, M_1 , strikes a lighter target, M_2 , the maximum deflection it can experience in a single collision is given by [31]

$$\theta_c = \sin^{-1}(M_2/M_1). \quad (5.10)$$

Eq. (5.10) yields 36.9° and 17.5° for Ne and Ar colliding with C, respectively. Experimental geometries in DRS are chosen so the dominating single scattering peaks caused by the primary ions are excluded from the TOF spectra. The closer the detector angle ϕ (here 45°) is to θ_c , the greater the probability becomes that a multiply scattered primary ion will reach the detector.

The simulated TOF spectrum in Fig. 5.6c for $\alpha = 28^\circ$ does not successfully reproduce the multiple scattering contribution of Ne(MS) to the overall experimental intensity distribution. This is believed to be due to the oversimplified model of liquid heptadecane employed in these calculations. The discussion of this shortcoming follows similar arguments to the ones given in Section 5.6.3.1 on why the C recoil intensity falls short of the experimentally measured one at this angle of incidence.

The results shown in Fig. 5.6 and their preceding discussion validate the application of Eq. (5.9) to describe the atomic interaction not only between Ar and H, but also between Ne and H. Thus, Eq. (5.9) may provide a means for adjusting the screening radius in interatomic potentials of the Molière type when collisions with the lightest of elements, hydrogen, are to be considered.

5.6.3.3. 4.0 keV Ar⁺ Bombardment of an Organic Polymer

A final test of the applicability of the modified screening radius, a_{X-H} , for interactions involving H was performed for higher relative collision energies between Ar, C, and H. Bertrand et al. [98] prepared single crystals of an organic polymer, hexatriacontane (C₃₆H₇₄), deposited as films of $\sim 5 \mu\text{m}$ thickness on silicon wafers. In

these films, the carbon zigzag chains forming the molecules' backbones were oriented parallel to the surface normal with the chain-end methyl groups directed out of the surface. The single crystals have an orthorhombic structure [97]. Bertrand et al. then applied DRS to test the molecules' vertical orientation. They measured the fluxes of H and C atoms recoiling from 4.0 keV Ar⁺ collisions with the oriented films.

An example TOF spectrum of Bertrand et al. is reproduced in Fig. 5.7 along with a formerly simulated TOF spectrum [66] (denoted by $a = a_F$), where the Firsov screening length, a_F , was used in the calculation. While the simulation mirrors the separation of the H(DR) and C(DR) peaks quite well, it no longer comes as a surprise that the H/C peak intensity ratio is not reproduced as desired. However, a very close

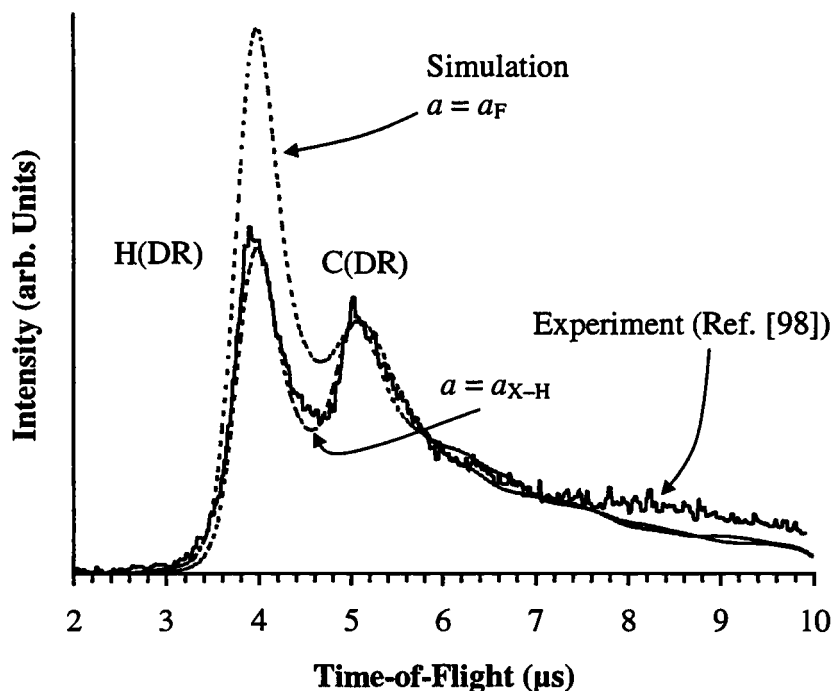


Fig. 5.7 Comparison of calculated TOF spectra (dashed lines) to an experimental one (solid line) for hexatriacontane [98] resulting from 4.0 keV Ar⁺ irradiation at $\alpha = 6^\circ$.

The Molière potential was employed in the calculations. One simulation ($a = a_F$) only used the screening radius according to Eq. (5.5), while the other ($a = a_{X-H}$) made use of both Eqs. (5.5) and (5.9) for Ar-C / C-C and for Ar-H / C-H / H-H interactions, respectively. ($\phi = 35^\circ$, drift length 90 cm)

match (denoted by $a = a_{X-H}$) is obtained by not only applying a_F but also a_{X-H} from Eq. (5.9) to describe atomic interactions.

Two specific observations are worth discussing. One is the improved calculated peak shape in comparison to Figs. 5.5 and 5.6; the other one is a more successful overall match of the simulation to the experiment. The former observation implies that multiple scattering mechanisms leading to H and C recoils of all different energies are realistically modeled by MARLOWE. This can only be true if the real film's surface is accurately represented by the modeled one for hexatriacontane, e.g. they agree to a high measure. The higher initial kinetic energy of the Ar^+ projectiles (4.0 keV) is most likely responsible for the overall better match between simulation and experiment. As mentioned in Section 5.3, empirical interatomic potentials, such as the Molière potential, grow asymptotically in their validity and applicability the higher the relative collision energies of the colliding particles are.

The results shown in Figs. 5.5, 5.6, and 5.7 provide strong evidence that the application of a_{X-H} together with a_F should lead to an improved accuracy in computer simulations of atomic interactions involving H.

5.6.4. The Correction factor Γ_{X-H}

A correction factor similar to that proposed by Overbury and Huntley [107] and O'Connor and MacDonald [101], Γ in Eqs. (5.7) and (5.8), when applied to H can be written down by dividing Eq. (5.9) by Eq. (5.5), yielding

$$\Gamma_{X-H} = \frac{a_{X-H}}{a_F} = \frac{(Z_1^{2/11} + 1)^{-11/6}}{(Z_1^{1/2} + 1)^{-2/3}}. \quad (5.11)$$

Z_1 is the atomic number for hydrogen's collision partner 'X'. A plot of Γ_{X-H} as a function of Z_1 is shown in Fig. 5.8. Notice that Γ_{X-H} reduces the Firsov screening length ($a_{X-H} = \Gamma_{X-H} a_F$) by 50% or more for collision partners 'X' of atomic number $Z_1 \leq 23$. The applicability of Γ_{X-H} was demonstrated successfully in the foregoing sections for two atomic numbers from Fig. 5.8, namely $Z_1 = 10$ and 18 for Ne and Ar,

respectively. It remains to be shown whether equally good agreement between simulation and experiment can be achieved in other low-energy ion scattering and recoiling studies where different combinations of 'X' and H, e.g. values for Z_1 in Eq. (5.11), are found.

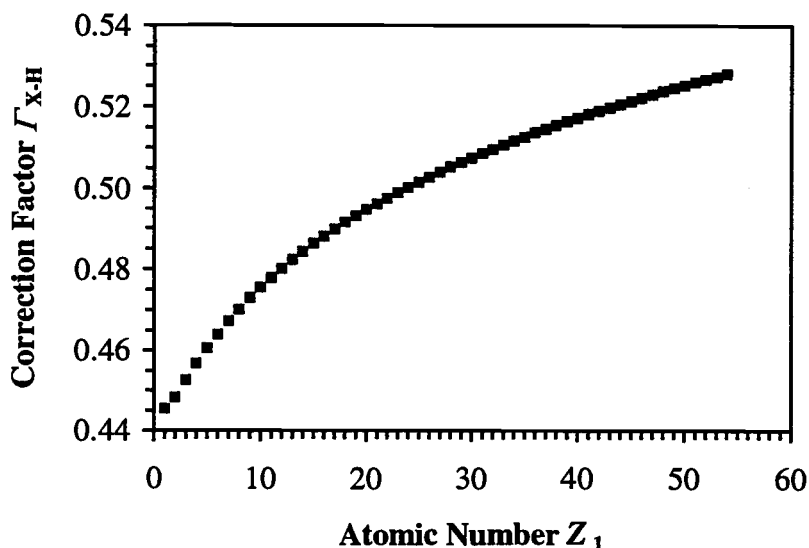


Fig. 5.8 Plot of the correction factor Γ_{X-H} versus the atomic number Z_1 . 'X' in Γ_{X-H} denoted hydrogen's collision partner. See Eq. (5.11).

5.7. Summary

A correction factor to the screening radius specific to X–H interactions, where X represents any other atom, was derived using time-of-flight direct recoil spectrometry and the MARLOWE computer code. The application of this correction factor in computer simulations of ion bombardments of hydrocarbon surfaces improved the exactness of the calculations and led to a much better agreement with experimental data. Hydrogen no longer exhibits an abnormally high differential recoil cross-section when compared to other target masses but follows the general trend. This allows a more accurate determination of absolute numbers of the H surface concentration in adsorption studies as well as compositional and structural analyses using DRS.

Chapter 6. General Conclusions

The work presented in this dissertation describes the adaptation and application of a well-established surface analytical technique, time-of-flight direct recoil spectrometry (TOF-DRS), to the vacuum-liquid interface. Having originally been developed as a tool for surface structural analysis of solid materials, TOF-DRS has hereby become available to provide molecular-level data on the composition and average orientation of molecules in the surface of liquids. To this end, a unique TOF spectrometer was constructed and commissioned by the author and his co-worker, T.G. Gannon. Details of the design as well as proof of key capabilities of the spectrometer were given in Chapter 2. An uncontaminated, continuously refreshed surface of the liquid under investigation can be created, from which a pulsed inert gas ion beam is scattered. Scattered projectiles as well as atoms/ions ejected from the liquid are counted as a function of their flight time to the particle detector. The resulting TOF spectra clearly demonstrated the spectrometer's capability of providing experimental data enabling qualitative identification of the surface composition.

Because the spectrometer was largely constructed from "second-hand" components, some technical (though most likely rather costly) upgrades would provide immense benefits. Those include a more powerful ion source capable of delivering inert gas ions with well defined energies up to 5 keV or higher, which would result in a higher quality of the experimental data obtainable. Even more importantly, the limitation of the detector angle to 45° (singular θ, ϕ -space) ought to be overcome by permitting access to either a discrete or continuous θ, ϕ -space. This added degree of freedom would provide a better choice of experimental geometries and would thereby greatly improve the versatility of the TOF spectrometer.

Issues related to the quantification of experimental data in TOF-DRS were considered in Chapters 3, 4, and 5. Chapter 3 discussed the measurement of the absolute detection efficiency, ε , of a continuous channel electron multiplier as a function of the atomic number, Z , and velocity, v , of low-energy noble gas ions (He^+ , Ar^+ , and Xe^+). The experimental data revealed a Z -dependence of the threshold

velocity below which a multiplier does not respond to impinging particles, an issue that previously had not been resolved in the existing literature. The results obtained in the linear region of response were generalized and transformed into a universal expression yielding the detection efficiency for *any* particle with atomic number Z . The final expression can be written as $\varepsilon(v, Z) = a \left(v - b/Z^c \right) Z^n$, with $a = (2.6 \pm 0.1) \times 10^{-6}$ s/m, $b = (7.8 \pm 0.2) \times 10^4$ m/s, $c = 0.26 \pm 0.01$, and $n = 0.39 \pm 0.02$.

Due to detector-age related effects such as loss of gain, the requirement of either an *in situ* calibration or, at least, an easily performed calibration becomes necessary when absolute numbers for surface concentrations are to be determined. Fortunately, this technically challenging requirement can be waived when dealing with atomic ratios, which is most frequently done in TOF-DRS. The assumption here is that the gradual decline in detector sensitivity or gain happens to equal proportions no matter what the atomic number of the impinging particle is. This is a very reasonable assumption because the internal resistance of the electron multiplier determines the gain, while being independent of Z .

In order to arrive at accurate and useful elemental surface composition information, it is necessary to extract correct count rate data from peaks in experimental TOF spectra. The computer simulations in Chapter 4 were used to investigate the depth distributions of recoils and their multiple scattering contributions to TOF spectra. The simulations provided new insight into, and better understanding of, the changing nature of spectral peak shapes as a function of projectile energy and mass, the angle of incidence, and properties of the bombarded surface itself. The results confirmed the high surface sensitivity of DRS and revealed the dependence of the sampling depth on the primary ion type and energy. The interplay of these experimental parameters can be exploited in order to probe either the very top atomic layer of the sample only or subsurface layers as well. While the former is accomplished by shallow incident angles α , high projectile mass, and low beam energies, the latter requires $\alpha \cong \phi/2$ (specular angle of incidence), low projectile mass, and high beam energies.

A direct correlation between a recoil's location in the TOF-intensity tail and its depth of origin in the target material could not be found from the results of the simulations. Instead, complex multiple-collision mechanisms cause every target layer to be represented in the TOF tail down to the maximum penetration depth of the incident primary ion. Many more systematic trajectory calculations have to be run in order to investigate in detail the multiple-scattering contributions of recoiled target atoms to TOF spectra, which might lead to a reproducible scheme of background subtraction in TOF-DRS.

The comparison of simulated and experimental TOF spectra in Chapter 4 resulted in a clear demonstration of the inadequacy of hydrogen's differential recoil cross-section derived from calculations involving standard potentials and screening lengths. This indication of a breakdown of fundamental assumptions in the interaction potential when applied to H atoms was then further investigated in Chapter 5. Liquid heptadecane ($C_{17}H_{36}$) was used as a model system for known surface composition and structure. Experimental TOF spectra obtained under various conditions were compared and fit to simulated spectra, while the screening radius in the computations was used as a fitting parameter. A correction factor, Γ_{X-H} , to the screening radius specific to X-H interactions, where X represents any other atom, was derived and can be expressed as $\Gamma_{X-H} = (Z_1^{2/11} + 1)^{-11/6} / (Z_1^{1/2} + 1)^{-2/3}$, with Z_1 being the atomic number of atom X. The application of this correction factor in computer simulations of ion scattering and recoiling from organic polymer surfaces drastically improved the exactness of the calculations and led to a much better agreement with experimental data. As a result of the application of Γ_{X-H} , hydrogen no longer exhibits an abnormally high differential recoil cross-section when compared to other target masses but follows their general trend.

Finally, all molecular and ionic liquids studied by TOF-DRS to date contain H as the most abundant element. The correction of hydrogen's interaction potential via adjusting its screening radius was therefore a crucial step toward a more accurate determination of surface concentrations involving H with regard to both relative ratios and absolute numbers. Chapter 5 successfully demonstrated the applicability of Γ_{X-H}

for Ne and Ar primary projectiles in the simulation of TOF-DRS experiments. It remains to be shown whether equally good agreement between simulation and experiment can be achieved when either different primary ions are used or the studied target surface is more complex in regard to its elemental composition.

Bibliography

- [1] J.C. Vickerman, in: *Surface Analysis - The Principal Techniques* (Wiley, Chichester, 1997).
- [2] M.A. Wilson, A. Pohorille, and L.A. Pratt, *J. Chem. Phys.* **88** (1988) 3291.
- [3] M. Matsumoto and Y. Kataoka, *J. Chem. Phys.* **88**(5) (1988) 3233.
- [4] R.M. Townsend and S.A. Rice, *J. Chem. Phys.* **94**(3) (1991) 2207.
- [5] M. Matsumoto and Y. Kataoka, *Phys. Rev. Lett.* **69**(26) (1992) 3782.
- [6] M. Matsumoto and Y. Kataoka, *J. Chem. Phys.* **90**(4) (1989) 2398.
- [7] J. Oberbrodage and H.O.G. Siegbahn, *Int. J. Quantum Chem.* **63**(6) (1997) 1123.
- [8] J. Dietter and H. Morgner, *Chem. Phys.* **241** (1999) 55.
- [9] I. Benjamin and A. Pohorille, *J. Chem. Phys.* **100**(9) (1994) 6500.
- [10] M. Kawamata and T. Yamamoto, *J. Phys. Soc. Japan* **66**(8) (1997) 2350.
- [11] P. Smith, R.M. Lyndell-Bell, J.C. Earnshaw, and W. Smith, *Mol. Phys.* **96**(2) (1999) 249.
- [12] X. Zhuang, P.B. Miranda, D. Kim, and Y.R. Shen, *Phys. Rev. B* **59**(19) (1999) 12632.
- [13] V. Bindu and T. Pradeep, *J. Chem. Phys.* **106**(3) (1997) 1231.
- [14] V. Bindu, K. Smitha, and T. Pradeep, *Mol. Phys.* **93**(1) (1998) 85.
- [15] H. Morgner, *Adv. At., Mol., Opt. Phys.* **42** (2000) 387.
- [16] M.J. Schultz, C. Schnitzer, D. Simonelli, and S. Baldelli, *Int. Rev. Phys. Chem.* **19**(1) (2000) 123.

- [17] G.M. Nathanson, P. Davidovits, D.R. Worsnop, and C.E. Kolb, *J. Phys. Chem.* **100** (1996) 13007.
- [18] J. Stöhr, in: *NEXAFS Spectroscopy* (Springer, Berlin, 1992).
- [19] Y. Yamamoto, R. Mitsumoto, E. Ito, T. Araki, Y. Ouchi, K. Seki, and Y. Takanishi, *J. Electr. Spec. Rel. Phen.* **78** (1996) 367.
- [20] M.A. Gleeson, T.T. Nuver, J. Lourenço, A.M.C. Moutinho, J. Los, and A.W. Kleyn, Ion sputtering as a probe of liquid surfaces, *Roy. Soc. Chem. E-Journal PhysChemComm*, <http://www.rsc.org/ej/qu/1999/A907932G/index.htm>, (1999).
- [21] T. Pradeep and R.G. Cooks, *Amer. Soc. Mass Spectr.* **93** (1993) 1044.
- [22] T. Pradeep and R.G. Cooks, *Mat. Res. Soc. Symp. Proc.* **380** (1995) 93.
- [23] J. Los, M.A. Gleeson, W.R. Koppers, T.L. Weeding, and A.W. Kleyn, *J. Chem. Phys.* **111**(24) (1999) 11080.
- [24] J.W. Rabalais, J.A. Schultz, R. Kumar, and P.T. Murray, *J. Chem. Phys.* **78** (1983) 5250.
- [25] J.W. Rabalais, *Science* **250** (1990) 521.
- [26] J.W. Rabalais, *Surf. Sci.* **299/300** (1994) 219.
- [27] M. Tassotto, T.J. Gannon, and P.R. Watson, *J. Chem. Phys.* **107**(21) (1997) 8899.
- [28] G. Andersson and H. Morgner, *Surf. Sci.* **405** (1998) 138.
- [29] M.T. Robinson and I.M. Torrens, *Phys. Rev. B* **9** (1974) 5008.
- [30] Y.S. Chen, G.L. Miller, D.A.H. Robinson, G.H. Wheatly, and T.M. Buck, *Surf. Sci.* **62** (1977) 133.
- [31] J.W. Rabalais, *CRC Critical Rev. Sol. St. Mat. Sci.* **14** (1988) 319.

- [32] M.S. Hammond, J.A. Schultz, and A.R. Krauss, *J. Vac. Sci. Technol. A* **13**(3) (1995) 1136.
- [33] H. Goldstein, in: *Classical Mechanics*, 2nd ed. (Addison-Wesley, Reading, Mass., 1980), pp. 105-119.
- [34] J.B. Marion, in: *Classical Dynamics of Particles and Systems* (Academic Press, New York, 1970), pp. 243-312.
- [35] H. Bu, M. Shi, K. Boyd, and J.W. Rabalais, *J. Chem. Phys.* **95** (1991) 2882.
- [36] P.G. Bertrand and J.W. Rabalais, "Ion Scattering and Recoiling for Elemental Analysis and Structure Determination", in: *Low Energy Ion-Surface Interactions*, edited by J.W. Rabalais (Wiley, New York, 1994), pp. 55-116.
- [37] E.S. Mashkova and V.A. Molchanov, in: *Medium-Energy Ion Reflections from Solids* (North-Holland Physics Publishing, Amsterdam, 1985), pp. 444.
- [38] I.M. Torrens, in: *Interatomic Potentials* (Academic Press, New York and London, 1972), pp. 247.
- [39] M. Nastasi, J.W. Mayer, and J.K. Hirvonen, in: *Ion-Solid Interactions: Fundamentals and Applications* (University Press, Cambridge, 1996), pp. 62-87.
- [40] R.S. Williams, "Quantitative Intensity Analysis of Low-Energy Scattering and Recoiling from Crystal Surfaces", in: *Low Energy Ion-Surface Interactions*, edited by J.W. Rabalais (Wiley, New York, 1994), pp. 1-54.
- [41] M.T. Robinson, Information on MARLOWE and the user's guide are available at <http://www.ssd.ornl.gov/Programs/MARLOWE/MARLOWE.html>, (2000).
- [42] M.T. Robinson, MARLOWE (ver. 15), released 07/01, RSICC, <http://www-rsicc.ornl.gov/rsic.html>, (2000).
- [43] M.T. Robinson, in: *User's Guide to MARLOWE (Version 14c)* (1997).
- [44] V. Bykov and J.W. Rabalais, *Nucl. Instrum. Methods* **B114** (1996) 371.
- [45] M.T. Robinson, *Radiat. Eff. Def. Sol.* **141** (1997) 1.

- [46] M.T. Robinson, *Radiat. Eff. Def. Sol.* **130-131** (1994) 3.
- [47] C. Lehmann and M.T. Robinson, *Phys. Rev.* **134** (1964) A37.
- [48] M.T. Robinson and O.S. Oen, *Phys. Rev.* **132** (1963) 2385.
- [49] G. Molière, *Z. Naturforsch.* **2a** (1947) 133.
- [50] O.B. Firsov, *Sov. Phys. JETP* **6/33(3)** (1958) 534.
- [51] J.F. Ziegler, J.P. Biersack, and U. Littmark, in: *The Stopping and Range of Ions in Solids* (Pergamon Press, New York, 1985).
- [52] S.T. Nakagawa and Y. Yamamura, *Radiat. Eff.* **105** (1988) 239.
- [53] S.T. Nakagawa, *Radiat. Eff.* **112** (1990) 1.
- [54] S.T. Nakagawa, *Radiat. Eff. Def. Sol.* **116** (1991) 21.
- [55] M. Born and J.E. Mayer, *Z. Phys.* **75** (1932) 1.
- [56] H.H. Andersen and P. Sigmund, *Nucl. Instrum. Methods* **38** (1965) 238.
- [57] P.M. Morse, *Phys. Rev.* **34** (1929) 57.
- [58] M.T. Robinson, *Mat. Fys. Medd. Dan. Vid. Selsk.* **43** (1993) 27.
- [59] M.T. Robinson, *J. Nucl. Mat.* **216** (1994) 1.
- [60] E. Fermi and E. Teller, *Phys. Rev.* **72** (1947) 399.
- [61] J. Lindhard and M. Scharff, *Phys. Rev.* **124(1)** (1961) 128.
- [62] J. Lindhard, V. Nielsen, and M. Scharff, *K. Dan. Vidensk. Selsk. Mat. Fys. Medd.* **36(10)** (1968).
- [63] O.S. Oen and M.T. Robinson, *Nucl. Instrum. Methods* **132** (1976) 647.

- [64] T.J. Gannon, "Time-of-Flight Scattering and Recoil Spectrometry (TOF-SARS) Applied to Molecular Liquid Surfaces: A New Approach to Surface Composition and Orientation," Ph.D. Thesis, Oregon State University, 1999.
- [65] M. Tassotto and P.R. Watson, *Rev. Sci. Instr.* **71**(7) (2000) 2704.
- [66] M. Tassotto and P.R. Watson, *Surf. Sci.* **464**(2-3) (2000) 251.
- [67] T.J. Gannon, M. Tassotto, and P.R. Watson, *Chem. Phys. Lett.* **300** (1999) 163.
- [68] T.J. Gannon, G. Law, P.R. Watson, A.J. Carmichael, and K.R. Seddon, *Langmuir* **15**(24) (1999) 8429.
- [69] M. Tassotto and P.R. Watson, submitted to *Surface Science* (2000).
- [70] A.W. Adamson, in: *Physical Chemistry of Surfaces*, 4th ed. (Wiley, New York, 1982).
- [71] J.B. Hudson, in: *Surface Science: An Introduction* (Wiley, New York, 1992), pp. 136.
- [72] O. Grizzi, M. Shi, H. Bu, and J.W. Rabalais, *Rev. Sci. Instrum.* **61** (1990) 740.
- [73] A.V. Solov'ev and A.B. Tolstoguzov, *Sov. Phys. Tech. Phys.* **32**(5) (1987) 580.
- [74] T.J. Gannon and P.R. Watson, *J. Vac. Sci. Technol. A* **15**(5) (1997) 2580.
- [75] M.E. Saecker, S.T. Govoni, D.V. Kowalski, M.E. King, and G.M. Nathanson, *Science* **252** (1991) 1421.
- [76] K.J. Snowdon and C.H. Barber, *J. Phys. E: Sci. Instrum.* **12** (1979) 923.
- [77] J.W. Rabalais, *J. Vac. Sci. Technol. A* **9**(3) (1991) 1293.
- [78] B.L. Schram, A.J.H. Boerboom, W. Kleine, and J. Kistemaker, *Physica (Utr.)* **32** (1966) 749.
- [79] L.A. Dietz and J.C. Sheffield, *J. Appl. Phys.* **46**(10) (1975) 4361.

- [80] C.N. Burrous, A.J. Lieber, and V.T. Zaviantseff, *Rev. Sci. Instrum.* **38**(10) (1967) 1477.
- [81] D.H. Crandall, J.A. Ray, and C. Cisneros, *Rev. Sci. Instrum.* **46**(5) (1975) 562.
- [82] J. Fricke, A. Müller, and E. Salzborn, *Nucl. Instrum. Methods* **175** (1980) 379.
- [83] J.R. Sharber, J.D. Winningham, and W.R. Sheldon, *IEEE Trans. Nucl. Sci.* **NS-15** (1968) 536.
- [84] B. Tatry, J.M. Bosqued, and H. Rene, *Nucl. Instrum. Methods* **69** (1969) 254.
- [85] G.E. Iglesias and J.O. McGarity, *Rev. Sci. Instrum.* **42**(11) (1971) 1728.
- [86] A. Egidi, R. Marconero, G. Pizzella, and F. Sperli, *Rev. Sci. Instrum.* **40**(1) (1969) 88.
- [87] J.P. Ravon, *Nucl. Instrum. Methods* **211** (1983) 7.
- [88] E.S. Parilis and L.M. Kishinevskii, *Sov. Phys. Sol. St.* **3**(4) (1960) 885.
- [89] J.N. Chen, M Shi., S. Tachi, and J.W. Rabalais, *Nuc. Instrum. Methods* **B16** (1986) 91.
- [90] G. Paschmann, E.G. Shelley, C.R. Chappell, R.D. Sharp, and L.F. Smith, *Rev. Sci. Instrum.* **41**(12) (1970) 1706.
- [91] personal communication with Laura Ray, Director of Engineering, Detector Technology.
- [92] H. Bu, M. Shi, and J.W. Rabalais, *Nucl. Instrum. Methods* **B61** (1991) 337.
- [93] T. Fuse, M. Watanabe, Y. Kido, O. Ishiyama, M. Shinohara, and F. Ohtani, *Surf. Sci.* **357-358** (1996) 119.
- [94] M.M. Li and D.J. O'Connor, *Nucl. Instrum. Methods* **B149** (1999) 460.
- [95] W.S. Yang, J. Sokolov, F. Jona, and P.M. Marcus, *Solid State Commun.* **41** (1982) 191.

- [96] T.E. Derry, L. Smit, and J.F. van der Veen, *Surf. Sci.* **167** (1986) 502.
- [97] P.W. Teare, *Acta Cryst.* **12** (1959) 294.
- [98] P. Bertrand, H. Bu, and J.W. Rabalais, *J. Phys. Chem.* **97** (1993) 13788.
- [99] S.J. Cyvin, in: *Molecular Vibrations and Mean Square Amplitudes* (Elsevier, Amsterdam, 1968).
- [100] B.M. Ocko, X.Z. Wu, E.B. Sirota, S.K. Sinha, O. Gang, and M. Deutsch, *Physical Review E* **55**(3) (1997) 3164.
- [101] D.J. O'Connor and R.J. MacDonald, *Radiat. Eff.* **34** (1977) 247.
- [102] O. Grizzi, J.E. Gayone, G.R. Gómez, R.G. Pregliasco, and E.A. Sánchez, *J. Nucl. Mat.* **248** (1997) 428.
- [103] M.H. Mintz, I. Jacob, and D. Shaltiel, "Adaptation of New Techniques to Study Surface and Bulk Properties of H-Metal Systems", in: *Hydrogen in Intermetallic Compounds II*, edited by L. Schlapbach (Springer, Berlin, 1992), Vol. 67, pp. 285.
- [104] J.A. Schultz and J.W. Rabalais, *Chem. Phys. Lett.* **108**(4) (1984) 328.
- [105] J.A. Schultz, S. Contarini, Y.S. Jo, and J.W. Rabalais, *Surf. Sci.* **154** (1985) 315.
- [106] P. Gombás, "Statistische Behandlung des Atoms", edited by S. Flügge (Springer, Berlin, 1956), Vol. XXXVI, pp. 109.
- [107] S.H. Overbury and D.R. Huntley, *Phys. Rev. B* **32**(10) (1985) 6278.

Appendices

Appendices

Appendix A. FORTRAN Code for User-Supplied MARLOWE Analysis Procedure EXTRAZ

Phase 1 portion:

```

C#          EXTRINZ                                EXNZ0000
G+  SUBROUTINE EXTRIN( ID )                        EXNZ0010
C  Version Z: the Phase 1 portion of EXTRA procedure. EXNZ0020
C  The required data are supplied by the NAMELIST &XTRZ, Input Record 15. EXNZ0030
C  This version only works for single-task MARLOWE simulations. EXNZ0040
C  The values are:                                EXNZ0050
C                                                  EXNZ0060
C          KCHOICE ( = 1) control variable;        EXNZ0070
C          KCHOICE = 1 Time-of-Flight spectrum is generated EXNZ0080
C          KCHOICE = 2 Energy ratio spectrum is generated EXNZ0090
C          KCHOICE = 3 1 and 2                    EXNZ0100
C                                                  EXNZ0110
C          KTIEFE ( = 0) control variable;         EXNZ0120
C          KTIEFE = 0 no scoring of depth of recoils EXNZ0130
C          KTIEFE = 1 correlation of depth of recoils with EXNZ0140
C                   TOF is generated              EXNZ0150
C                                                  EXNZ0160
C          NBIN   ( = 300) Number of time bins in TOF spectrum EXNZ0170
C                                                  EXNZ0180
C          DT     ( = 100) width of time bin in nanoseconds EXNZ0190
C                                                  EXNZ0200
C          ACCANG Detector acceptance angle in degrees. Default is EXNZ0210
C                   calculated from physical dimensions of detector opening EXNZ0220
C                   (DIAM) and LENGTH of flight tube EXNZ0230
C                                                  EXNZ0240
C          LENGTH ( = 112.5) Length of flight tube in centimeters EXNZ0250
C                                                  EXNZ0260
C          DETANG ( = 45.0) Angle of position of detector with respect to EXNZ0270
C                   direction of incident projectile EXNZ0280
C                                                  EXNZ0290
C          ERATIO ( = 0.0) Represents the lower limit in an energy EXNZ0300
C                   spectrum. The upper limit is 1.0 EXNZ0310
C                                                  EXNZ0320
C          TOFOUT ( =spectrum.tof) Name of output file for TOF spectrum EXNZ0330
C                   Maximum of 20 characters allowed. EXNZ0340
C                                                  EXNZ0350
C          ENOUT  ( =spectrum.ene) Name of output file for energy EXNZ0360
C                   spectrum. Maximum of 20 characters allowed. EXNZ0370
C                                                  EXNZ0380
C          DPHOUT ( =hist.dph) Name of output file for depth-TOF EXNZ0390
C                   correlation. Maximum of 20 characters allowed. EXNZ0400
C                                                  EXNZ0410
C                                                  EXNZ0420
COMMON and CODE blocks required: EXNZ0430
C  SCON  PARM  PRJX  CHRZ  EXTZ  EXCZ  #END EXNZ0440
C  CHARACTER*28 ERMS EXNZ0450
C                                                  EXNZ0460
C  Definition of NAMELIST Input Record 15: EXNZ0470
C  NAMELIST/XTRZ/KCHOICE,KTIEFE,NBIN,DT,ACCANG,LENGTH,DETANG,ERATIO, EXNZ0480
C  1      TOFOUT,ENOUT,DPHOUT EXNZ0490
C  DATA ERMS/'*****Error in EXTRINZ: '/ EXNZ0500
C                                                  EXNZ0510
C  Define diameter of detector aperture in centimeters EXNZ0520
C  CONSTANT DIAM = 1.112 EXNZ0530
C                                                  EXNZ0540
C  Report presence of subroutine in LCOM EXNZ0550
C  CALL LINER( 2, 2) EXNZ0560
C  WRITE( LCOM, '(6X,38X,A/6X,38X,A)' ) EXNZ0570
C  1      'EXTRAZ: Time-of-Flight and/or Energy Spectra', EXNZ0580
C  2      'Input data from the NAMELIST record &XTRZ' EXNZ0590
C  IF( SURFCE .NE. 1 .AND. SURFCE .NE. 2 ) THEN EXNZ0600
C                                                  EXNZ0610
C  Error in the program options: EXNZ0620
C  ID = 91 EXNZ0630

```

```

          CALL LINER( 3, 1)
          WRITE( LCOM, '(6X,33X,2A,I3,A)' ) ERMS, 'SURFCE =',
1          SURFCE, ' is not supported'
          ENDIF
C
C      Default values of the input data:
          KCHOICE = 1
          KTIEFE = 0
          NBIN = 300
          DT = 100
          ACCANG = 0.0
          LENGTH = 112.5
          DETANG = 45.0
          ERATIO = 0.0
          TOFOUT = 'spectrum.tof'
          ENOUT = 'spectrum.ene'
          DPHOUT = 'hist.dph'
C
C      Read the data from Input Record 15:
C
CODE block required to define NAMELIST READ syntax:
C      NMLR      #END
1          XTRZ, IOSTAT = IOS, ERR = 20, END = 20 )
C
C      Process the input data:
          IF ( ACCANG .EQ. 0 ) THEN
              ACCANG = DIAM / LENGTH
          ELSE
              ACCANG = ACCANG * DEGRAD
          ENDIF
          UPPER = NBIN * DT / 1000
C
C      Error in reading NAMELIST input data:
          IF ( KTIEFE .EQ.1 .AND. LAIP .NE. 1 ) THEN
              ID = 91
              CALL LINER( 3, 1)
              WRITE( LCOM, '(6X,2A)' ) ERMS,
1              ' Scoring of depth of recoils requires LAIP=1 !'
          ELSE IF ( KTIEFE .EQ.1 .AND. KCHOICE .NE. 1
1              .AND. KCHOICE .NE. 3 ) THEN
              ID = 91
              CALL LINER( 3, 1)
              WRITE( LCOM, '(6X,2A)' ) ERMS,
1              ' Depth scoring error --> KTIEFE=1 requires KCHOICE=1 or 3 !'
          ENDIF
C
          RETURN
C
C      Error in reading NAMELIST input data:
20 ID = 90
          CALL LINER( 3, 1)
          WRITE( LCOM, '(6X,26X,2A,I4,A)' ) ERMS, 'error', IOS,
1          encountered in Input Record 15'
          RETURN
G-      END

```

EXNZ0640
 EXNZ0650
 EXNZ0660
 EXNZ0670
 EXNZ0680
 EXNZ0690
 EXNZ0700
 EXNZ0710
 EXNZ0720
 EXNZ0730
 EXNZ0740
 EXNZ0750
 EXNZ0760
 EXNZ0770
 EXNZ0780
 EXNZ0790
 EXNZ0800
 EXNZ0810
 EXNZ0820
 EXNZ0830
 EXNZ0840
 EXNZ0850
 EXNZ0860
 EXNZ0870
 EXNZ0880
 EXNZ0890
 EXNZ0900
 EXNZ0910
 EXNZ0920
 EXNZ0930
 EXNZ0940
 EXNZ0950
 EXNZ0960
 EXNZ0970
 EXNZ0980
 EXNZ0990
 EXNZ1000
 EXNZ1010
 EXNZ1020
 EXNZ1030
 EXNZ1040
 EXNZ1050
 EXNZ1060
 EXNZ1070
 EXNZ1080
 EXNZ1090
 EXNZ1100
 EXNZ1110
 EXNZ1120
 EXNZ1130
 EXNZ1140
 EXNZ1150
 EXNZ1160
 EXNZ1170
 EXNZ1180

Phase 2 portion:

```

C#          EXTRAZ
G+      SUBROUTINE EXTRA( ID )
C      Version Z: Phase 2. Time-of-Flight/Energy analysis of recoiled
C      target atoms and scattered primaries. The input data are described
C      in EXTRINZ. SURFCE = 1 or 2 is required.
C      This version is for single-task MARLOWE simulations only.
C
C      This procedure requires two special COMMON blocks:
C
C      /EXCZ/TOFOUT,ENOUT
C
C      Specifications: 2 CHARACTER.
C
C      /EXTZ/KCHOICE,KTIEFE,LENGTH,NBIN,DT,ACCANG,DETANG,NCOUNT(3),
C      UPPER,ERATIO,KTOF(NPTS,KIND+1),KENG(NPTS,KIND+1),
C      KTSLOW(KIND+1),CEM(3),KESLOW(KIND+1),CIS(KIND+1),
C      TIEFE(MXDB,MXTB,KIND)
C
C      Specifications: 8 REAL, 9 INTEGER.

```

EXTZ0000
 EXTZ0010
 EXTZ0020
 EXTZ0030
 EXTZ0040
 EXTZ0050
 EXTZ0060
 EXTZ0070
 EXTZ0080
 EXTZ0090
 EXTZ0100
 EXTZ0110
 EXTZ0120
 EXTZ0130
 EXTZ0140
 EXTZ0150
 EXTZ0160
 EXTZ0170
 EXTZ0180

```

C
C
COMMON and CODE blocks required:
C   SCON   PARM   PRJX   SERF   CASK   ATMS   PASS   CHRX
C   FHLR   VACS   SRFX
C   EXTZ   EXCZ   #END
C
C   Local variable specifications:
C       INTEGER TOFBIN, ENBIN
C       REAL ZEITPUNKT
C
C   Select the requested section of the procedure:
C       IF( ID .EQ. 2 ) THEN
C
C       Define direction cosines for the detector
C           CEM(1) = COS (PHI * DEGRAD) * SIN (( THA + DETANG) * DEGRAD)
C           CEM(2) = SIN (PHI * DEGRAD) * SIN (( THA + DETANG) * DEGRAD)
C           CEM(3) = COS (( THA + DETANG) * DEGRAD)
C
C       Initialization at the start of a set of cascades:
C           NCOUNT(1) = 0
C           NCOUNT(2) = 0
C           DO 2 J=1 , KIND+1
C               DO 1 I=1 , NPTS
C                   KTOF(I,J) = 0
1           CONTINUE
C               KTSLOW(J) = 0
C               KESLOW(J) = 0
2           CONTINUE
C               DO 5 N=1 , KIND
C                   DO 4 M=1 , MXTB
C                       DO 3 L=1 , MXDB
C                           TIEFE(L,M,N) = 0
3           CONTINUE
4           CONTINUE
5           CONTINUE
C
C       ELSE IF( ID .EQ. 3 ) THEN
C
C       Entry for the analysis of a single cascade:
C
C           IF ( AZIM .EQ. 1 .AND. NRUN .GT. 1 ) THEN
C
C           Define new direction cosines for detector:
C               CEM(1) = SIN ((THA+DETANG) * DEGRAD) * AZIMU(1)
C               CEM(2) = SIN ((THA+DETANG) * DEGRAD) * AZIMU(2)
C               CEM(3) = COS ((THA+DETANG) * DEGRAD)
C           ENDIF
C
C           DO 30 N = 1, NCASC
C
C           Scan the cascade for particles escaping through front surface:
C               IF( LARK(5,N) .GE. 20 .OR. LARK(5,N) .LT. 10 ) GO TO 30
C               NCOUNT(1) = NCOUNT(1) + 1
C
C           See if particle hits the detector:
C               KNT = 0
C               DO 10 M = 1, 3
C                   IF ( (RFCX(6+M,N) .GE. ( CEM(M) - (ACCANG / 2) )) .AND.
C                       (RFCX(6+M,N) .LE. ( CEM(M) + (ACCANG / 2) )))
C                       KNT = KNT + 1
1           CONTINUE
2           IF ( KNT .NE. 3 ) GO TO 30
10
C
C           Process particle hitting the detector:
C               NCOUNT(2) = NCOUNT(2) + 1
C
C           Find the atom type:
C               KND = LARK(1,N)
C
C           Select output --> time-of-flight spectrum:
C               IF ( (KCHOICE .EQ. 1) .OR. (KCHOICE .EQ. 3) ) THEN
C
C               Calculate time-of-flight:
C                   T = SQRT( W(KND) / (2*RFCX(10,N))) * LENGTH * CORR
C
C           Particle is beyond end of TOF spectrum:
C               IF ( T .GT. UPPER) THEN
C                   KTSLOW(KND) = KTSLOW(KND) + 1

```

```

EXTZ0190
EXTZ0200
EXTZ0210
EXTZ0220
EXTZ0230
EXTZ0240
EXTZ0250
EXTZ0260
EXTZ0270
EXTZ0280
EXTZ0290
EXTZ0300
EXTZ0310
EXTZ0320
EXTZ0330
EXTZ0340
EXTZ0350
EXTZ0360
EXTZ0370
EXTZ0380
EXTZ0390
EXTZ0400
EXTZ0410
EXTZ0420
EXTZ0430
EXTZ0440
EXTZ0450
EXTZ0460
EXTZ0470
EXTZ0480
EXTZ0490
EXTZ0500
EXTZ0510
EXTZ0520
EXTZ0530
EXTZ0540
EXTZ0550
EXTZ0560
EXTZ0570
EXTZ0580
EXTZ0590
EXTZ0600
EXTZ0610
EXTZ0620
EXTZ0630
EXTZ0640
EXTZ0650
EXTZ0660
EXTZ0670
EXTZ0680
EXTZ0690
EXTZ0700
EXTZ0710
EXTZ0720
EXTZ0730
EXTZ0740
EXTZ0750
EXTZ0760
EXTZ0770
EXTZ0780
EXTZ0790
EXTZ0800
EXTZ0810
EXTZ0820
EXTZ0830
EXTZ0840
EXTZ0850
EXTZ0860
EXTZ0870
EXTZ0880
EXTZ0890
EXTZ0900
EXTZ0910
EXTZ0920
EXTZ0930
EXTZ0940
EXTZ0950
EXTZ0960
EXTZ0970

```

```

          KTSLOW(NTYPE+1) = KTSLOW(NTYPE+1) + 1
        ELSE
C
C      Calculate bin# for particle:
          TOFBIN = INT( T / DT * 1000 ) + 1
C
C      Score tof of particle in table under appropriate type:
          KTOF(TOFBIN,KND) = KTOF(TOFBIN,KND) + 1
          KTOF(TOFBIN,NTYPE+1) = KTOF(TOFBIN,NTYPE+1) + 1
C
          IF ( KTIEFE .EQ. 1 ) THEN
C
C      Find the original depth of a recoil:
          IF ( N .LE. LINT ) THEN
              QA = RIS(3,N)
          ELSE
              IF ( N .LE. MINT ) GO TO 20
              I = N - MINT + LVAC
              QA = RV(3,I)
          ENDIF
C
C      Use front surface as origin:
          QA = QA - FRINGE(2,1,1)
C
C      Convert units to Angstroms:
          QA = QA * BASE
C
C      Score depth of origin:
          NTB = INT ( T / NDZT * 1000 ) + 1
          NDB = INT ( QA / NDTF * 100 ) + 1
          IF ( NDB .GT. MXDB ) NDB = MXDB
          TIEFE(NDB,NTB,KND) = TIEFE(NDB,NTB,KND) + 1
20      ENDIF
          CONTINUE
C
          ENDIF
C
C      Select output: --> energy ratio spectrum:
          ELSE IF ( (KCHOICE .EQ. 2) .OR. (KCHOICE .EQ. 3) ) THEN
C
C      Calculate energy ratio:
          U = RFCX(10,N) / EKIP
C
C      Particle's energy ratio falls below ERATIO:
          IF ( U .LE. ERATIO ) THEN
              KESLOW(KND) = KESLOW(KND) + 1
              KESLOW(NTYPE+1) = KESLOW(NTYPE+1) + 1
          ELSE
C
C      Calculate bin# for particle:
          ENBIN = INT ( (U-ERATIO) * 1000 )
C
C      Score energy ratio of particle in table:
          KENG(ENBIN,KND) = KENG(ENBIN,KND) + 1
          KENG(ENBIN,NTYPE+1) = KENG(ENBIN,NTYPE+1) + 1
          ENDIF
30      CONTINUE
C
C      Read the time controlling the intermediate storage of data:
          ZEITPUNKT =
CODE block required to control the timer:
C      TIMR      #END
C
          IF( ZEITPUNKT .GT. CLOCK(4) .OR. NRUN .EQ. MAXRUN ) THEN
C
C      It is time for an intermediate OR final saving of data:
          IF ( (KCHOICE .EQ. 1) .OR. (KCHOICE .EQ. 3) ) THEN
C
C      Open output file:
          OPEN (50,FILE = TOFOUT, STATUS = 'UNKNOWN')
C
C      Write time-of-flight data to output:
          DO 35 I=1 , NTYPE+1
              CIS(I) = 0
35      CONTINUE
          WRITE ( 50, 150 ) (JOBID(J),J=1,4)
          WRITE ( 50, 100 )
          WRITE ( 50, '(8X,A19,1X,8(4X,A3))' )
          EXTZ0980
          EXTZ0990
          EXTZ1000
          EXTZ1010
          EXTZ1020
          EXTZ1030
          EXTZ1040
          EXTZ1050
          EXTZ1060
          EXTZ1070
          EXTZ1080
          EXTZ1090
          EXTZ1100
          EXTZ1110
          EXTZ1120
          EXTZ1130
          EXTZ1140
          EXTZ1150
          EXTZ1160
          EXTZ1170
          EXTZ1180
          EXTZ1190
          EXTZ1200
          EXTZ1210
          EXTZ1220
          EXTZ1230
          EXTZ1240
          EXTZ1250
          EXTZ1260
          EXTZ1270
          EXTZ1280
          EXTZ1290
          EXTZ1300
          EXTZ1310
          EXTZ1320
          EXTZ1330
          EXTZ1340
          EXTZ1350
          EXTZ1360
          EXTZ1370
          EXTZ1380
          EXTZ1390
          EXTZ1400
          EXTZ1410
          EXTZ1420
          EXTZ1430
          EXTZ1440
          EXTZ1450
          EXTZ1460
          EXTZ1470
          EXTZ1480
          EXTZ1490
          EXTZ1500
          EXTZ1510
          EXTZ1520
          EXTZ1530
          EXTZ1540
          EXTZ1550
          EXTZ1560
          EXTZ1570
          EXTZ1580
          EXTZ1590
          EXTZ1600
          EXTZ1610
          EXTZ1620
          EXTZ1630
          EXTZ1640
          EXTZ1650
          EXTZ1660
          EXTZ1670
          EXTZ1680
          EXTZ1690
          EXTZ1700
          EXTZ1710
          EXTZ1720
          EXTZ1730
          EXTZ1740
          EXTZ1750
          EXTZ1760

```

```

1      'channel      TOF', (TYPE(J),J=1,NTYPE), 'SUM'      EXTZ1770
      IF ( NCOUNT(2) .EQ. 0 ) THEN                        EXTZ1780
C
C      Spectrum is empty:                                  EXTZ1790
      WRITE ( 50, 110 )                                     EXTZ1800
      ELSE                                                  EXTZ1810
C
C      Print time-of-flight table:                         EXTZ1820
      DO 50 NB = 1, NBIN                                    EXTZ1830
        T = NB * DT / 1000                                 EXTZ1840
        WRITE ( 50, '(9X,I6,4X,F8.2,1X,8(3X,I4))' )      EXTZ1850
        NB, T, (KTOF(NB,J),J=1,NTYPE+1)                  EXTZ1860
1
C
C      Add total # of counts in spectrum:                  EXTZ1870
      DO 40 K = 1, (NTYPE+1)                                EXTZ1880
        CIS(K) = CIS(K) + KTOF(NB,K)                      EXTZ1890
40      CONTINUE                                           EXTZ1900
50      CONTINUE                                           EXTZ1910
      WRITE ( 50, '(//6X,A19,3X,8(1X,I6))' )             EXTZ1920
      'Counts in spectrum:', (CIS(J),J=1,NTYPE+1)        EXTZ1930
      WRITE ( 50, '(6X,A21,1X,8(1X,I6))' )               EXTZ1940
      '# of atoms dropped:', (KTSLOW(J),J=1,NTYPE+1)     EXTZ1950
      ENDIF                                               EXTZ1960
      WRITE ( 50, '(6X,A31,13X,I10)' )                   EXTZ1970
1      'Total # of atoms into detector:', NCOUNT(2)     EXTZ1980
      WRITE ( 50, '(6X,A32,12X,I10)' )                   EXTZ1990
1      'Total # of atoms leaving target:', NCOUNT(1)    EXTZ2000
C
C      Report current state of RANX:                       EXTZ2010
      WRITE ( 50, 120 ) (RANX(I), I = 1, NRNX)          EXTZ2020
C
C      Report total time of calculation in hours and #of cascade:
      Q = (CLOCK(3) - CLOCK(2)) / 3600.0                EXTZ2030
      WRITE( 50, '(6X,A,I7,A,F10.2,1X,A)' )              EXTZ2040
1      'Total running time for ',NRUN,' cascades: ',Q,'hours'
C
C      Close output file:                                  EXTZ2050
      CLOSE ( 50)                                         EXTZ2060
C
C      IF ( KTIEFE .EQ. 1 ) THEN                           EXTZ2070
C
C      Open output file:                                   EXTZ2080
      OPEN (70,FILE = DPHOUT, STATUS = 'UNKNOWN')        EXTZ2090
C
C      write depth-TOF correlation table(s) to output,    EXTZ2100
      one for each type of target atom:                  EXTZ2110
      WRITE ( 70, 150 ) (JOBID(J),J=1,4)                 EXTZ2120
      WRITE ( 70, '(6X,A)' )                              EXTZ2130
1      '***** Recoil Depth-TOF Correlation Tables *****'
      DO 70 KA=2, NTYPE                                    EXTZ2140
        WRITE ( 70, 140 ) TYPE(KA)                        EXTZ2150
        WRITE ( 70, 160 ) (J,J=1,MXTB)                   EXTZ2160
        WRITE ( 70, 170 ) (J*NDZT*0.001,J=1,MXTB)        EXTZ2170
        DO 60 KB=1, MXDB                                    EXTZ2180
          WRITE ( 70, 180) KB, (KB*NDTF*0.01),            EXTZ2190
          (TIEFE(KB,J,KA),J=1,MXTB)                      EXTZ2200
1
60      CONTINUE                                           EXTZ2210
70      CONTINUE                                           EXTZ2220
C
C      Close output file:                                  EXTZ2230
      CLOSE ( 70)                                         EXTZ2240
C
C      ENDIF                                               EXTZ2250
C
C      ELSE IF ( (KCHOICE .EQ. 2) .OR. (KCHOICE .EQ. 3) ) THEN
C
C      Open output file:                                   EXTZ2260
      OPEN (60,FILE = ENOUT, STATUS = 'UNKNOWN')        EXTZ2270
C
C      write energy data to output:                       EXTZ2280
      DO 75 I=1 , NTYPE+1                                  EXTZ2290
        CIS(I) = 0                                         EXTZ2300
75      CONTINUE                                           EXTZ2310
      WRITE ( 60, 150 ) (JOBID(J),J=1,4)                 EXTZ2320
      WRITE ( 60, 130 )                                    EXTZ2330
      WRITE ( 60, '(8X,A19,1X,8(4X,A3))' )               EXTZ2340
1      'channel      E/E0', (TYPE(J),J=1,NTYPE), 'SUM'  EXTZ2350
      IF ( NCOUNT(2) .EQ. 0 ) THEN                      EXTZ2360
C
C      Spectrum is empty:                                  EXTZ2370
      EXTZ2380
      EXTZ2390
      EXTZ2400
      EXTZ2410
      EXTZ2420
      EXTZ2430
      EXTZ2440
      EXTZ2450
      EXTZ2460
      EXTZ2470
      EXTZ2480
      EXTZ2490
      EXTZ2500
      EXTZ2510
      EXTZ2520
      EXTZ2530
      EXTZ2540
      EXTZ2550

```

```

C          WRITE ( 60, 110 )
C          ELSE
C          Print energy table:
C          NL = INT ( (1-ERATIO) * 1000 )
C          DO 90 NB = 1, NL
C              U = ERATIO + NB * 0.001
C              WRITE ( 60, '(9X,I6,4X,F7.3,1X,8(3X,I4))' )
C                  NB, U, (KENG(NB,J),J=1,NTYPE+1)
C              DO 80 K = 1, (NTYPE+1)
C                  CIS(K) = CIS(K) + KENG(NB,K)
C              CONTINUE
C          CONTINUE
C          WRITE ( 60, '(//6X,A19,3X,8(1X,I6))' )
C              'Counts in spectrum:', (CIS(J),J=1,NTYPE+1)
C          WRITE ( 60, '(6X,A21,1X,8(1X,I6))' )
C              '# of atoms dropped:', (KESLOW(J),J=1,NTYPE+1)
C          ENDIF
C          WRITE ( 60, '(6X,A31,13X,I10)' )
C              'Total # of atoms into detector:', NCOUNT(2)
C          WRITE ( 60, '(6X,A32,12X,I10)' )
C              'Total # of atoms leaving target:', NCOUNT(1)
C
C          Report current state of RANX:
C          WRITE ( 60, 120 ) (RANX(I), I = 1, NRNX)
C
C          Report total time of calculation in hours and #of cascade:
C          Q = (CLOCK(3) - CLOCK(2)) / 3600.0
C          WRITE( 60, '(6X,A,I7,A,F10.2,1X,A)' )
C              'Total running time for ',NRUN,' cascades: ',Q,'hours'
C          Close output file:
C          CLOSE ( 60)
C
C          ENDIF
C          ENDIF
C          ENDIF
C          RETURN
C
C      Output Formats:
C      100 FORMAT(6X,10X,'Calculated Time-of-Flight Spectra'//6X,24X,'....Type
C          le of Atom....')
C      110 FORMAT(//6X,' ***** Spectrum is empty *****'//)
C      120 FORMAT(6X,'Current state of RANX =',
CODE block required to supply the RANX output format:
C      RNSD #END
C      130 FORMAT(6X,10X,'Calculated Energy Spectra'//6X,24X,'....Type of Ato
C          m....')
C      140 FORMAT(//6X,'Correlation Table for ',A2,' atoms: '/')
C      150 FORMAT(6X,2A, /6X,2A/)
C      160 FORMAT(6X,'Bin#',3X,'TOF',4X,300(I5,1X))
C      170 FORMAT(6X,'Depth',2X,'A/usec',1X,253(F5.1,1X))
C      180 FORMAT(6X,I5,2X,F6.1,1X,300(I5,1X))
C
C-      END
EXTZ2560
EXTZ2570
EXTZ2580
EXTZ2590
EXTZ2600
EXTZ2610
EXTZ2620
EXTZ2630
EXTZ2640
EXTZ2650
EXTZ2660
EXTZ2670
EXTZ2680
EXTZ2690
EXTZ2700
EXTZ2710
EXTZ2720
EXTZ2730
EXTZ2740
EXTZ2750
EXTZ2760
EXTZ2770
EXTZ2780
EXTZ2790
EXTZ2800
EXTZ2810
EXTZ2820
EXTZ2830
EXTZ2840
EXTZ2850
EXTZ2860
EXTZ2870
EXTZ2880
EXTZ2890
EXTZ2900
EXTZ2910
EXTZ2920
EXTZ2930
EXTZ2940
EXTZ2950
EXTZ2960
EXTZ2970
EXTZ2980
EXTZ2990
EXTZ3000
EXTZ3010
EXTZ3020
EXTZ3030
EXTZ3040
EXTZ3050
EXTZ3060
EXTZ3070
EXTZ3080
EXTZ3090
EXTZ3100

```

Phase 3 portion:

```

C#          EXTRAXZ
G+ SUBROUTINE EXTRAX( ID)
C Version Z: the Phase 3 portions of EXTRA procedure.
C This is just a phase 3 'dummy' procedure.
C          RETURN
G-      END
EXXZ0000
EXXZ0010
EXXZ0020
EXXZ0030
EXXZ0040
EXXZ0050

```

Appendix B. FORTRAN Code for User-Supplied MARLOWE Analysis Procedure SINGLEZ

Phase 1 portion:

```

C#                SINGLINZ                SNNZ0000
SUBROUTINE SINGLIN( ID)                SNNZ0010
C Version Z: The Phase 1 portion of SINGLEZ. The data required are
C taken from the NAMELIST record &SNGZ. The possible value is:
C                SNNZ0020
C                SNNZ0030
C                SNNZ0040
C                PROPOUT ( =Properties.out) Name of output file for detailed
C                cascade data. Maximum of 20 characters allowed.
C                SNNZ0050
C                SNNZ0060
C                SNNZ0070
COMMON and CODE blocks required:
C                SNNZ0080
C  SCON  PARM  SGCZ  #END                SNNZ0090
C    CHARACTER*24 ERMS                SNNZ0100
C                SNNZ0110
C Definition of Input Record 14:
C  NAMELIST/SNGZ/PROPOUT                SNNZ0120
C  DATA ERMS/'*****Error in SINGLINZ: '/
C                SNNZ0130
C                SNNZ0140
C                SNNZ0150
W  IF( ID .LE. 1 ) THEN                SNNZ0160
C                SNNZ0170
C Report presence of subroutine in LCOM:
C  CALL LINER( 2, 2)                SNNZ0180
C  WRITE( LCOM, '(6X,20X,A/6X,47X,A)' )
C  1 'SINGLEZ: properties of single collisions and flight distances',
C  2 'Input data from the NAMELIST record &SNGZ'
C                SNNZ0190
C                SNNZ0200
C                SNNZ0210
C                SNNZ0220
C                SNNZ0230
C Default values of the input data:
C  PROPOUT(1) = 'Properties1.out'
C  PROPOUT(2) = 'Properties2.out'
C  PROPOUT(3) = 'Properties3.out'
C  PROPOUT(4) = 'Properties4.out'
C  PROPOUT(5) = 'Properties5.out'
C                SNNZ0240
C                SNNZ0250
C                SNNZ0260
C                SNNZ0270
C                SNNZ0280
C                SNNZ0290
C                SNNZ0300
C Read the data from Input Record 14:
C                SNNZ0310
C                SNNZ0320
CODE block required to define NAMELIST READ syntax:
C  NMLR  #END                SNNZ0330
C  1                SNGZ, IOSTAT = IOS, ERR = 20, END = 20 )
C                SNNZ0340
C                SNNZ0350
C                SNNZ0360
W  ENDIF                SNNZ0370
C  RETURN                SNNZ0380
C                SNNZ0390
C Error reading NAMELIST input data:
C  20 ID = 80
C  CALL LINER( 3, 1)
C  WRITE( LCOM, '(6X,28X,2A,I4,A)' ) ERMS, 'error', IOS,
C  1 'encountered in Input Record 14'
C  RETURN
C  END                SNNZ0400
C                SNNZ0410
C                SNNZ0420
C                SNNZ0430
C                SNNZ0440
C                SNNZ0450
C                SNNZ0460

```

Phase 2 portion:

```

C#                SINGLEZ                SGLZ0000
SUBROUTINE SINGLE( ID, N)                SGLZ0010
C Version Z: The Phase 2 portion of SINGLEZ. Retrieves detailed data
C for each detected recoil atom over the course of a full cascade:
C its type, time-of-flight, original depth, init. kinetic energy,
C recoil angle wrt direction of flight of collision partner,
C projection of recoil angle onto z-axis, number of collisions the
C recoil suffered on its way to the target surface, length of flight
C path; type of projectile causing the collision, its kinetic energy,
C number of collisions before this encounter, and projection of
C direction of projectile before the encounter onto z-axis.
C                SGLZ0020
C                SGLZ0030
C                SGLZ0040
C                SGLZ0050
C                SGLZ0060
C                SGLZ0070
C                SGLZ0080
C                SGLZ0090
C                SGLZ0100
C                SGLZ0110
C The procedure requires two special COMMON and CODE blocks:
C                SGLZ0120
C                SGLZ0130
C  /SGCZ/PROPOUT(5)                SGLZ0140
C                SGLZ0150
C  Specifications: 1 CHARACTER.
C                SGLZ0160
C                SGLZ0170

```

```

C      /SGLZ/PROP(10, LONG)
C
C      Specifications: 1 REAL.
C
C      The procedure only works in conjunction with the EXTRA/Z analysis
C      and requires its special COMMON block EXTZ!
C
COMMON and CODE blocks required:
C      SCON   PARM   PRJX   FIND   SERF   SRFC   CHRX   VACS
C      ATMS   CASK   EXTZ   SGLZ   SGCZ   #END
C
C      Define local variables:
C      CHARACTER*20 DATEI
C      CHARACTER*24 ERMS
C      DATA ERMS/'*****Error in SINGLEZ: '/
C
C      Select the required section:
C      IF ( ID .EQ. 2 ) THEN
C
C      Initialization at the start of a set of cascades:
C      IF ( .NOT. INFORM(8) .OR.
C      1      ( KCHOICE .NE. 1 .AND. KCHOICE .NE. 3 )) THEN
C
C      Required EXTRA/Z is missing:
C      CALL LINER( 3, 1)
C      WRITE( LCOM, '(6X,2A)' ) ERMS, 'SINGLE/Z only works in conju
C      lunction with EXTRA/Z, &XTRZ KCHOICE = 1 or 3 required'
C      ENDIF
C
C      Prepare output file(s):
C      OPEN ( 80, FILE = PROPOUT(1), STATUS = 'UNKNOWN')
C      DO 4 M=1, LONG
C      DO 3 L=1, 10
C      PROP(L,M) = 0.0
C      3      CONTINUE
C      4      CONTINUE
C      NCOUNT(3) = 0
C
C      Print header of data table to output file:
C      WRITE ( 80, 30 ) (JOBID(J),J=1,4)
C      WRITE ( 80, '(2A/)' ) '***** Detailed Information',
C      1      ' on recoiled target atoms *****'
C      WRITE ( 80, '(2A)' ) 'ID-R, TOF(us), Depth(A), KE-R, PHI, PHI(Z)',
C      1      '#Coll.-R, Path (A), ID-P, KE-P, #Coll.-P, THETA(Z)',
C      CLOSE (80)
C
C      ELSE IF ( ID .EQ. 3 ) THEN
C
C      Initialization at the start of a single cascade:
C      DO 6 M=1, LONG
C      DO 5 L=1, 10
C      PROP(L,M) = 0.0
C      5      CONTINUE
C      6      CONTINUE
C
C      ELSE IF ( ID .EQ. 4 ) THEN
C
C      Entry after collision involving newly displaced target atoms:
C
C      Record the projectile data:
C      PROP(7, NCASC) = LA(1)
C      PROP(8, NCASC) = EK(1)
C      PROP(10, NCASC) = ( ACOS(RCOS(3,1)) / DEGRAD ) - 90
C      PROP(9, NCASC) = PROP(5, MPT(1))
C
C      Record the displaced target atom data:
C      Record the original depth:
C      QA = REF(3, N)
C      Use front surface as origin:
C      QA = QA - FRINGE(2, 1, 1)
C      Convert units to Angstroms:
C      QA = QA * BASE
C      Score depth of origin:
C      PROP(1, NCASC) = QA
C      Record the initial kinetic energy:
C      PROP(2, NCASC) = EK(N)
C      Record change in (z-axis-)direction cosine and total recoil
C      angle of displaced target atom wrt incident projectile:
C      QA = RCOS(1, 1)

```

SGLZ0180
SGLZ0190
SGLZ0200
SGLZ0210
SGLZ0220
SGLZ0230
SGLZ0240
SGLZ0250
SGLZ0260
SGLZ0270
SGLZ0280
SGLZ0290
SGLZ0300
SGLZ0310
SGLZ0320
SGLZ0330
SGLZ0340
SGLZ0350
SGLZ0360
SGLZ0370
SGLZ0380
SGLZ0390
SGLZ0400
SGLZ0410
SGLZ0420
SGLZ0430
SGLZ0440
SGLZ0450
SGLZ0460
SGLZ0470
SGLZ0480
SGLZ0490
SGLZ0500
SGLZ0510
SGLZ0520
SGLZ0530
SGLZ0540
SGLZ0550
SGLZ0560
SGLZ0570
SGLZ0580
SGLZ0590
SGLZ0600
SGLZ0610
SGLZ0620
SGLZ0630
SGLZ0640
SGLZ0650
SGLZ0660
SGLZ0670
SGLZ0680
SGLZ0690
SGLZ0700
SGLZ0710
SGLZ0720
SGLZ0730
SGLZ0740
SGLZ0750
SGLZ0760
SGLZ0770
SGLZ0780
SGLZ0790
SGLZ0800
SGLZ0810
SGLZ0820
SGLZ0830
SGLZ0840
SGLZ0850
SGLZ0860
SGLZ0870
SGLZ0880
SGLZ0890
SGLZ0900
SGLZ0910
SGLZ0920
SGLZ0930
SGLZ0940
SGLZ0950
SGLZ0960

```

QB = RCOS(2,1)
QC = RCOS(3,1)
QD = RCOS(1,N)
QE = RCOS(2,N)
QF = RCOS(3,N)
PROP(4,NCASC) = (ACOS(QF)-ACOS(QC)) / DEGRAD
QG = QA*QD + QB*QE + QC*QF
QA = QA**2 + QB**2 + QC**2
QD = QD**2 + QE**2 + QF**2
QA = SQRT(QA)
QD = SQRT(QD)
PROP(3,NCASC) = ACOS(QG/(QA*QD)) / DEGRAD
C
ELSE IF ( ID .EQ. 7 ) THEN
C
C Record pathlength traversed by projectile at the completion of a
C trajectory segment not terminating in a collision:
PROP(6,MPT(1)) = PROP(6,MPT(1)) + SVS(8,1)
C
ELSE IF ( ID .EQ. 8 ) THEN
C
C Record pathlength traversed by projectile after a collision
C involving an atom and increase counter for #of collisions for
C projectile:
PROP(5,MPT(1)) = PROP(5,MPT(1)) + 1
PROP(6,MPT(1)) = PROP(6,MPT(1)) + SVS(8,1)
C
ELSE IF ( ID .EQ. 10 ) THEN
C
C Entry for the analysis of a single cascade:
C
IF ( AZIM .EQ. 1 .AND. NRUN .GT. 1 ) THEN
C
C Define new direction cosines for detector:
CEM(1) = SIN ((THA+DETANG) * DEGRAD) * AZIMU(1)
CEM(2) = SIN ((THA+DETANG) * DEGRAD) * AZIMU(2)
CEM(3) = COS ((THA+DETANG) * DEGRAD)
ENDIF
C
C Process each atom from this cascade:
DO 20 MA = 1, NCASC
C
C Scan the cascade for recoiled atoms escaping through front
C surface:
IF( LARK(5,MA) .NE. 10 ) GO TO 20
C
C See if atom hits the detector:
KNT = 0
DO 10 MB = 1, 3
IF ( (RFCX(6+MB,MA) .GE. ( CEM(MB) - (ACCANG / 2) ))
1 .AND. (RFCX(6+MB,MA) .LE. ( CEM(MB) + (ACCANG / 2) )))
2 KNT = KNT + 1
10 CONTINUE
IF ( KNT .NE. 3 ) GO TO 20
C
C Find the atom type:
KND = LARK(1,MA)
C
C Calculate time-of-flight:
T = SQRT( W(KND) / (2*RFCX(10,MA))) * LENGTH * CORR
IF ( T .GT. UPPER ) GO TO 20
C
C Advance the recoiled atom counter:
NCOUNT(3) = NCOUNT(3) + 1
C
C Record properties for this atom (3000 entries per file):
IF ( NCOUNT(3) .LE. 3000 ) DATEI = PROPOUT(1)
IF ( NCOUNT(3) .GT. 3000 .AND. NCOUNT(3) .LE. 6000 )
1 DATEI = PROPOUT(2)
1 IF ( NCOUNT(3) .GT. 6000 .AND. NCOUNT(3) .LE. 9000 )
1 DATEI = PROPOUT(3)
1 IF ( NCOUNT(3) .GT. 9000 .AND. NCOUNT(3) .LE. 12000 )
1 DATEI = PROPOUT(4)
IF ( NCOUNT(3) .GT. 12000 ) DATEI = PROPOUT(5)
OPEN ( 80, POSITION = 'APPEND', FILE = DATEI )
WRITE ( 80, 40) TYPE(KND), T, (PROP(I,MA),I=1,4),
1 INT(PROP(5,MA)), PROP(6,MA), TYPE(PROP(7,MA)),
2 PROP(8,MA), INT(PROP(9,MA)), PROP(10,MA)
CLOSE (80)
SGLZ0970
SGLZ0980
SGLZ0990
SGLZ1000
SGLZ1010
SGLZ1020
SGLZ1030
SGLZ1040
SGLZ1050
SGLZ1060
SGLZ1070
SGLZ1080
SGLZ1090
SGLZ1100
SGLZ1110
SGLZ1120
SGLZ1130
SGLZ1140
SGLZ1150
SGLZ1160
SGLZ1170
SGLZ1180
SGLZ1190
SGLZ1200
SGLZ1210
SGLZ1220
SGLZ1230
SGLZ1240
SGLZ1250
SGLZ1260
SGLZ1270
SGLZ1280
SGLZ1290
SGLZ1300
SGLZ1310
SGLZ1320
SGLZ1330
SGLZ1340
SGLZ1350
SGLZ1360
SGLZ1370
SGLZ1380
SGLZ1390
SGLZ1400
SGLZ1410
SGLZ1420
SGLZ1430
SGLZ1440
SGLZ1450
SGLZ1460
SGLZ1470
SGLZ1480
SGLZ1490
SGLZ1500
SGLZ1510
SGLZ1520
SGLZ1530
SGLZ1540
SGLZ1550
SGLZ1560
SGLZ1570
SGLZ1580
SGLZ1590
SGLZ1600
SGLZ1610
SGLZ1620
SGLZ1630
SGLZ1640
SGLZ1650
SGLZ1660
SGLZ1670
SGLZ1680
SGLZ1690
SGLZ1700
SGLZ1710
SGLZ1720
SGLZ1730
SGLZ1740
SGLZ1750

```

```

20 CONTINUE
IF ( NRUN .EQ. MAXRUN ) THEN
C
C After the last cascades:
IF ( NCOUNT(3) .EQ. 0 ) THEN
OPEN ( 80, POSITION = 'APPEND', FILE = PROPOUT(1) )
WRITE ( 80, 50 )
CLOSE (80)
ENDIF
ENDIF
ENDIF
RETURN
C
C Output Formats:
30 FORMAT(2A/,2A/)
40 FORMAT(A, ',', 2(F6.2, ',', '), F8.2, ',', ', 2(F6.2, ',', '), I3, ',', ', F6.2, ',', ', A, ',
1', F8.2, ',', ', I3, ',', ', F6.2, ',', ', ')
50 FORMAT(//', '***** NO data recorded - NCOUNT(3) = 0 *****'/)
C
END

```

SGLZ1760
SGLZ1770
SGLZ1780
SGLZ1790
SGLZ1800
SGLZ1810
SGLZ1820
SGLZ1830
SGLZ1840
SGLZ1850
SGLZ1860
SGLZ1870
SGLZ1880
SGLZ1890
SGLZ1900
SGLZ1910
SGLZ1920
SGLZ1930
SGLZ1940
SGLZ1950

Phase 3 portion:

```

C# SNGLEXZ SNXZ0000
G+ SUBROUTINE SNGLEX( ID) SNXZ0010
C version Z: the Phase 3 portion of SINGLEX. SNXZ0020
C This is just a phase 3 'dummy' procedure. SNXZ0030
RETURN SNXZ0040
G- END SNXZ0050

```

Appendix C. FORTRAN Code for User-Supplied MARLOWE CODE and COMMON Blocks

```

C ***** MT 2/99 master.cmt CCMT0000
C ..... CCMT0010
C . MARLOWE CCMT0020
C . Descriptions of personal (private) CODE and COMMON Blocks . CCMT0030
C ..... CCMT0040
C ..... CCMT0050
C ..... CCMT0060
C . EXTRA/Z . CCMT0070
C ..... CCMT0080
C ..... CCMT0090
NAME: EXCZ CCMT0100
CHARACTER*20 TOFOUT, ENOUT, DPHOUT CCMT0110
COMMON/EXCZ/TOFOUT, ENOUT, DPHOUT CCMT0120
SAVE SAVE /EXCZ/ CCMT0130
C CCMT0140
C CCMT0150
NAME: EXTZ CCMT0160
C CCMT0170
C ***** CCMT0180
C The two parameters MXDB (max# Depth Bin) and MXTB (max# Time Bin) are CCMT0190
C calculated from: CCMT0200
C MXDB = MXTF / NDTF * 100 MXTF: max depth in Angstrom considered CCMT0210
C in correlation table if KTIEFE=1 CCMT0220
C NDTF: depth resolution in picometers CCMT0230
C MXTB = MXZT / NDZT * 1000 MXZT: max TOF in usec considered in CCMT0240
C correlation table if KTIEFE=1 CCMT0250
C NDZT: time resolution in nanoseconds CCMT0260
C CORR = SQRT(1.60219E-19/1.66057E-27)/1E4 CCMT0270
C CORR: unit correction/conversion factor CCMT0280
C for calculating the time-of-flight in CCMT0290
C [µs] with length in [cm], mass in [amu] CCMT0300
C and energy in [ev] CCMT0310
C ***** CCMT0320
C CCMT0330
PARAMETER ( NPTS = 2000, MXTF = 30, NDTF = 20, MXZT = 30, CCMT0340
1 NDZT = 200, MXDB = 150, MXTB = 150, CCMT0350
2 CORR = 0.9822644 ) CCMT0360
REAL LENGTH CCMT0370

```

```

      INTEGER CIS,TIEFE
      COMMON/EXTZ/KCHOICE,KTIEFE,NBIN,DT,ACCANG,LENGTH,DETANG,NCOUNT(3),
1         UPPER,ERATIO,KTOF(NPTS,KIND+1),KENG(NPTS,KIND+1),
2         KTSLOW(KIND+1),CEM(3),KESLOW(KIND+1),CIS(KIND+1),
3         TIEFE(MXDB,MXTB,KIND)
SAVE  SAVE /EXTZ/
C
C      .....
C      .      SINGLE/Z      .
C      .....
C
NAME:  SGCZ
      CHARACTER*20 PROPOUT
      COMMON/SGCZ/PROPOUT(5)
SAVE  SAVE /SGCZ/
C
NAME:  SGLZ
      COMMON/SGLZ/PROP(10,LONG)
SAVE  SAVE /SGLZ/
C
C
C.....End of File.....

```

```

CCMT0380
CCMT0390
CCMT0400
CCMT0410
CCMT0420
CCMT0430
CCMT0440
CCMT0450
CCMT0460
CCMT0470
CCMT0480
CCDT1490
CCDT1500
CCDT1510
CCDT1520
CCMT0530
CCMT0540
CCMT0550
CCMT0560
CCMT0570
CCMT0580
CCMT0590

```

Appendix D. Additions to MARLOWE Source Code

File: marlow.ms

The following lines of code were inserted after line MRLW2190 to allow for azimuthally averaged direction of incidence of the primary projectile during simulation.

```

C ***** MT 1/99
C
      IF ( AZIM .EQ. 1 .AND. NRUN .GT. 1 ) THEN
C
C      Choose the initial azimuthal angle ...
35      QA = RANF()
          QC = QA**2
          QB = RANF()
          QD = QB**2
          QE = QC + QD
          IF ( QE .GT. 1 ) GO TO 35
          IF ( ZETA .NE. 0.0 .AND. ZETA .NE. 360.0 ) THEN
C
C      ... uniformly in sector defined by ZETA about azimuth PHI:
          QF = ZETA / 180 * ACOS( QA / SQRT(QE) )
          IF ( RANF() .GT. 0.5 ) QF = -QF
          QC = COS( PHI *DEGRAD + QF )
          QD = SIN( PHI *DEGRAD + QF )
          ELSE IF ( ZETA .EQ. 0.0 .OR. ZETA .EQ. 360.0 ) THEN
C
C      ... uniformly in a whole circle:
          QC = (QC - QD) / QE
          QD = 2 * QA * QB / QE
          IF ( RANF() .GT. 0.5 ) QD = -QD
          ENDIF
          AZIMU(1) = QC
          AZIMU(2) = QD
C
C      Define new incident direction of projectile:
          BEAM(1) = SIN (THA*DEGRAD) * QC
          BEAM(2) = SIN (THA*DEGRAD) * QD
          BEAM(3) = COS (THA*DEGRAD)
          PCOS(1) = BEAM(1)
          PCOS(2) = BEAM(2)
          PCOS(3) = BEAM(3)
C
          ENDIF
C

```

C *****

File: projex.ms

The following underlined code and completely new lines of code were inserted into projex.ms. The lines with identification numbers on the far right belong to the original MARLOWE code and serve as orientation.

```

C  Definition of Input Record 16:
      NAMELIST/PROJ/LAIP,LRIP,RAIP,REFIP,EKIP,THA,PHI,MAXRUN,NEW,
      1          LEAP,PRIM,DVRG,BEAM,MILLER,RANX,TRMP,AZIM,ZETA
C
C
C          ENDIF
C
C  Set default for NO randomization of azimuth, PHI, for
C  external irradiation:
      AZIM = 0
      ZETA = 0.0
C
C
C
CODE block required to define NAMELIST READ syntax:
C  NMLR  #END
      1          PROJ, IOSTAT = IOS, ERR = 40, END = 40 )
C
C  Check input data for azimuthal randomization:
      IF ( AZIM .EQ. 1 .AND. (LEAP .LT. 20 .OR. LEAP .GT. 23 .OR.
      1          MAXRUN .LE. 1 .OR. THA .EQ. 0.0) ) THEN
C      Input data error:
          MODE = 15
          CALL LINER( 3, 1)
          WRITE( LCOM, '(6X,2A)' ) '*****Error in &PROJ: ',
      1          'AZIM=1 requires MAXRUN>1, 20<=LEAP<=23, THA>0.0'
          RETURN
      ELSE IF ( AZIM .EQ. 0 .AND. ZETA .NE. 0.0 ) THEN
C      Input data error:
          MODE = 15
          CALL LINER( 3, 1)
          WRITE( LCOM, '(6X,2A,F6.1)' ) '*****Error in &PROJ: ',
      1          'AZIM = 1 is required for ZETA = ',ZETA
          RETURN
      ENDIF

```

File: common.mmf

The following underlined code was inserted into common.mmf for the definition of common variables.

```

NAME:  PRJX
      INTEGER PRIM,AZIM
      LOGICAL MILLER
      COMMON/PRJX/EKIP,THA,PHI,DVRG,RAIP(3),REFIP(3),BEAM(3),PCOS(3),
      1          MAXRUN,LEAP,LRIP,LAIP,NEW,NPRIM,PRIM,MILLER,AZIM,
      2          AZIMU(2),ZETA
SAVE  SAVE /PRJX/

```